nagra.

TECHNICAL REPORT 23-05

ClaySor 2023:

Update of 2SPNE SC/CE Sorption Model for Illite and Montmorillonite in GEMS Implementation

May 2024

Nagra | National Cooperative for the Disposal of Radioactive Waste
Hardstrasse 73 | 5430 Wettingen | Switzerland
T. +41 56 437 11 11 | info@nagra.ch | nagra.ch

nagra.

TECHNICAL REPORT 23-05

ClaySor 2023:

Update of 2SPNE SC/CE Sorption Model for Illite and Montmorillonite in GEMS Implementation

May 2024

O. Marinich, M. Marques Fernandes,
G.D. Miron & D.A. Kulik

Nuclear Energy and Safety Research Department,
Laboratory for Waste Management, Paul Scherrer Institute,
5232 Villigen PSI, Switzerland

Nagra | **National Cooperative for the Disposal of Radioactive Waste**
Hardstrasse 73 | 5430 Wettingen | Switzerland
T. +41 56 437 11 11 | info@nagra.ch | nagra.ch

ISSN 1015-2636

Abstract

The ClaySor model is an implementation of the two-site protolysis non-electrostatic surface complexation and cation exchange (2SPNE SC/CE) sorption model in the GEM-Selektor software and databases. In this work, the ClaySor model was made consistent with the PSI Chemical Thermodynamic Database 2020 (TDB 2020), resulting in the updated Sorption Thermodynamic Database (STDB 2023) for illite and montmorillonite. The STDB 2023 comprises surface complexation constants and selectivity coefficients for Cs(I), Cd(II), Co(II), Fe(II), Mn(II), Ni(II), Pb(II), Ra(II), Zn(II), Am(III), Cm(III) (illite only), Eu(III), Pu(III, IV), Np(IV, V), Sn(IV), Th(IV), Nb(V), Pa(V), and U(IV, VI).

Extensive experimental data on pH edges and adsorption isotherms, collected over a few decades at the Laboratory for Waste Management (LES) at the Paul Scherrer Institute and supplemented with recently obtained datasets, were compiled and evaluated. At the same time, the ClaySor model was fitted to all datasets of certain metal/clay mineral pairs using the GEMSFITS parameter optimisation tool to determine adjustable model parameters such as surface complexation constants and cation exchange selectivity coefficients. The performance of the updated model is demonstrated on sample pH edges and adsorption isotherms. The uncertainties of adjustable parameters were estimated by means of the 95% confidence interval determined via the Monte Carlo method as implemented in the GEMSFITS package. The re-evaluated equilibrium surface complexation constants and cation exchange selectivity coefficients (STDB 2023) are now fully consistent with the TDB 2020 and are provided in the appendix, along with the related metal hydrolysis constants. In addition, an overview of batch sorption experiments of the investigated elements on illite and montmorillonite used for the ClaySor model parameter optimisation is given in the appendix.

For some cations of interest, namely Cd(II) and Fe(II) for illite, as well as the surface complexation constants of Pu(III, IV), Np(IV), and U(IV) for illite and montmorillonite, the surface complexation constants were determined based on the linear correlations between the stability constants of aqueous and surface complexes (linear free energy relationships, LFERs). The estimated equilibrium constants of Cd(II) and Fe(II) were used to predict pH edges and adsorption isotherms, which showed a good agreement with the experimental data of chemical analogues, implying the reliability of the constants found in LFERs.

The ClaySor 2023 model and STDB 2023 for 2:1 clay minerals can be used to compute the solid-liquid distribution ratios (R_d) of many cationic elements in complex systems of geological and engineered barriers in the deep geological repository, namely the illite-containing argillaceous rocks and the bentonite buffer materials, interacting with porewaters of various compositions.

Zusammenfassung

Das ClaySor-Modell implementiert das «2-site protolysis non-electrostatic surface complexation and cation exchange» (2SPNE-SC/CE) in die GEM-Selektor-Software und in die Datenbanken. Dieser Bericht beschreibt, wie das ClaySor-Modell mit der PSI/Nagra chemisch-thermodynamischen Datenbank (TDB) 2020 in Einklang gebracht wurde. Das Ergebnis ist die aktualisierte Sorption thermodynamische Datenbank (STDB 2023) für Illit und Montmorillonit. Die STDB 2023 enthält Oberflächen-Komplexierungskonstanten und Selektivitätskoeffizienten für Cs(I), Cd(II), Co(II), Fe(II), Mn(II), Ni(II), Pb(II), Ra(II), Zn(II), Am(III), Cm(III) (nur Illite), Eu(III), Pu(III, IV), Np(IV, V), Sn(IV), Th(IV), Nb(V), Pa(V), and U(IV, VI).

Umfangreiche experimentelle Daten zu pH-Kanten und Adsorptionsisothermen, die über mehrere Jahrzehnte am Labor für Endlagersicherheit (LES) des Paul Scherrer Instituts gesammelt und mit neu gewonnenen Datensätzen ergänzt wurden, wurden zusammengestellt und ausgewertet. Gleichzeitig wurde das ClaySor-Modell mit Hilfe des Parameteroptimierungstools GEMSFITS an alle Datensätze bestimmter Metall-/Tonmineralpaare angepasst, um flexible Modellparameter wie Oberflächen-Komplexierungskonstanten und Kationenaustausch-Selektivitätskoeffizienten zu bestimmen. Die Wirksamkeit des aktualisierten Modells wird am Beispiel von pH-Kanten und Sorptionsisothermen demonstriert. Die Unsicherheiten der konfigurierbaren Parameter wurden mittels des 95 %-Konfidenzintervalls geschätzt, das wiederum mit der Monte-Carlo-Methode ermittelt und im GEMSFITS-Paket implementiert wurde. Die neu bewerteten Gleichgewichts-Oberflächen-Komplexierungskonstanten und Kationenaustausch-Selektivitätskoeffizienten (STDB 2023) stimmen nun vollständig mit der TDB 2020 überein und sind zusammen mit den entsprechenden Metallhydrolysekonstanten im Anhang aufgeführt. Darüber hinaus enthält der Anhang einen Überblick über Batch-Sorptionsexperimente für die untersuchten Elemente an Illit und Montmorillonit, die für die Parameteroptimierung des ClaySor-Modells verwendet wurden.

Für einige Kationen von Interesse, (Cd(II) und Fe(II) für Illit sowie jene von Pu(III, IV), Np(IV) und U(IV) für Illit und Montmorillonit), wurden die Oberflächen-Komplexierungskonstanten aus den linearen Korrelationen zwischen den Stabilitätskonstanten von wässrigen Komplexen und Oberflächenkomplexen («linear free energy relationships», LFER) bestimmt. Die geschätzten Gleichgewichtskonstanten von Cd(II) und Fe(II) wurden zur Vorhersage von pH-Kanten und Adsorptionsisothermen verwendet. Diese zeigten eine gute Übereinstimmung mit den experimentellen Daten der chemischen Analoga, was auf die Zuverlässigkeit der aus LFER ermittelten Konstanten hindeutet.

Mit dem Modell ClaySor 2023 und der STDB 2023 für 2:1-Tonminerale lassen sich die Feststoff-Flüssigkeit-Verteilungskoeffizienten (R_d) vieler kationischer Elemente in komplexen Systemen geologischer und technischer Barrieren des geologischen Tiefenlagers berechnen, nämlich am illithaltigen Tongestein und an den Bentonit-Puffermaterialien, die mit Porenwässern unterschiedlicher Zusammensetzung interagieren.

Table of Contents

List of Tables

List of Figures

1 Introduction

The multi-barrier system of a deep geological repository for radioactive waste involves a natural geological barrier formed by the repository host rock and a system of engineered barriers. Together, they ensure the long-term stability of the repository and the retention of radioactive and chemotoxic substances, and provide isolation, containment and retention of radioactive substances. In Switzerland, the Jurassic Opalinus Clay unit confined between clay-rich formations has been selected as the host rock and forms a natural geological barrier for the repository. The clay minerals in the sedimentary rocks mainly consist of illite and kaolinite, and to a lesser extent of smectite and chlorite (Mazurek et al. 2023). The 2:1 clay minerals, illite and montmorillonite, are considered to be the main sorbents in the Opalinus Clay due to their significant retention properties with regard to radionuclides and toxic substances. Montmorillonite is the primary mineral of the bentonite buffer material to be used in the engineered barrier system of the high-level waste repository. The process of radioactive and chemotoxic contaminant uptake by clay minerals in argillaceous rocks in the far-field and high clay-content materials in the near-field is crucial in determining their migration rate through such systems. A wide variety of different factors, such as the contaminant properties, the concentration, porewater and rock chemistry, sorbent content and properties, and the presence and concentration of competing metals, demonstrates the necessity for developing sorption models that can predict sorption in complex systems over wide ranges of conditions.

The development of the two-site protolysis non-electrostatic surface complexation cation exchange (2SPNE SC/CE) model (Baeyens & Bradbury 1997, Bradbury & Baeyens 1997, Bradbury & Baeyens 2009a), as well as sorption thermodynamic databases (STDB) for illite (Bradbury & Baeyens 2017) and montmorillonite (Baeyens & Bradbury 2017), became a fundamental scientific contribution to the framework for the safety analysis of a deep geological repository in Switzerland. The large array of experimental datasets, combined with the quantitative description of the experimental data performed using the MINSORB code (Bradbury & Baeyens 1995) (a specialised version of the MINEQL chemical speciation code (Westall et al. 1976)), formed the basis for compiling the aforementioned STDBs. The experimental datasets were represented by edges and isotherms that express pH-dependent and concentration-dependent adsorption, respectively. The sorption data were measured in simplified laboratory systems: $NaClO_4$ or NaCl background electrolyte solutions, purified and homo-ionic clay minerals, a CO_2 free atmosphere and a single radionuclide. The STDB comprises the equilibrium surface complexation constants and cation exchange selectivity coefficients of metals derived by fitting the experimental data. For metals for which no experimental data were available, the approach based on the relationship between stability constants of aqueous and surface complexes, so-called linear free energy relationships (LFER), was applied to derive surface complexation constants.

Surface complexation constants in both STDBs (Bradbury & Baeyens 2017 and Baeyens & Bradbury 2017) were retrieved (mostly by visual fitting) using the fragmented aqueous speciation thermodynamic data from different sources (Baes & Mesmer 1976, Hummel et al., 2002). The uncertainty of retrieved constants was not evaluated.

The PSI Chemical Thermodynamic Database 2020 (TDB 2020, Hummel & Thoenen 2023), an extension/update from its predecessor the PSI/Nagra Chemical Thermodynamic Database 12/07 (PSI/Nagra TDB 12/07, Thoenen et al. 2014), contains revised and justified thermodynamic data. It is the source of thermodynamic data for the models used for performance and safety assessments of the planned repositories for low- and intermediate-level as well as high-level radioactive waste in Switzerland.

To reduce uncertainties in geochemical calculations (e.g., porewater compositions, solubility limits, sorption database, diffusion database), a consistent workflow using a common chemical system (Kulik et al. 2023) was defined in the GEMS geochemical modelling software (Kulik et al. 2013), based on the TDB 2020 (Hummel & Thoenen 2023) as the reference source of all necessary thermodynamic data.

In 2017, at the end-of-life of the MINSORB code, the 2SPNE SC/CE sorption model for montmorillonite and illite was re-implemented in the GEM-Selektor package as the ClaySor model, and shown to produce the same results as those previously obtained with the MINSORB code (Kulik et al. 2018). Since then, the ClaySor model has been used with GEMS codes to model adsorption equilibria (pH edges, isotherms) during model training or the occasional fitting of thermodynamic surface complexation constants using the GEMSFITS code (Miron et al. 2015).

After the release of the updated chemical thermodynamic database, TDB 2020 (Hummel & Thoenen 2023), the ClaySor models had to be updated by adding or removing surface complexes to reflect changes in the aqueous speciation, and by (re)fitting the ClaySor-model adjustable parameters against the experimental data. Updating the models involved utilising the same experimental data used for the Bradbury & Baeyens (2017) and Baeyens & Bradbury (2017) databases, supplemented with more recent in-house datasets, as well as a few datasets from the external sources in order to fill data gaps. In this work, for the first time, the uncertainty intervals of equilibrium cation exchange selectivity coefficients and surface complexation constants were determined at the 95% confidence level using the Monte Carlo sampling method implemented in the GEMSFITS code (Miron et al. 2015). GEMSFITS is coupled with the GEMS geochemical solver needed to compute equilibria for the sorption experiments within the global or local least-square fitting routine. The sorption models for some metals were revised when compared to those presented in the earlier STDBs (Bradbury & Baeyens 1997, Baeyens & Bradbury 2017) due to three main factors:

1. Changes in the aqueous speciation patterns of metals in the updated thermodynamic database TDB 2020 (Hummel & Thoenen 2023) in comparison to the previously used thermodynamic databases - PSI/Nagra TDB 12/07 (Thoenen et al. 2014) and Nagra/PSI TDB 01/01 (Hummel et al. 2002).
2. The near-neutral pH range relevant to porewaters of argillaceous rocks, commonly found in geochemical systems associated with a radioactive waste repository, was used to guide the assessment of the experimental points. Due to these constraints, the derived selectivity coefficients and surface complexation constants are best applied in the corresponding pH range of 4 – 10. In some cases, the data fell outside this pH interval and were not used in the fitting. Consequently, no corresponding surface complexes were considered for low- or high-pH regions.
3. The uncertainty intervals of adjustable parameters and their correlations were used to remove those model parameters that showed low sensitivity during the fit. For some pH and sorbate concentration ranges, where limited experimental data were available, including more than one surface complex in the model resulted in high parameter correlation and high model uncertainty. To overcome this, the model was simplified by excluding the least sensitive parameters.

The effect of the three specified factors on the proposed sorption model is detailed for each relevant element in Chapter 4.

The aim of this report is to provide relevant details on the comprehensive update to the ClaySor model, consisting of the optimised values of equilibrium surface complexation constants and cation exchange selectivity coefficients made consistent with the TDB 2020, and with the uncertainties at the 95% confidence level. The updated ClaySor 2023 model and STDB 2023 can be used to compute solid liquid distribution ratios (R_d) of the most relevant radionuclides in the radioactive waste with oxidation states +I to +VI, on illite and montmorillonite in complex clay/porewater systems of host rocks and buffer materials to be used as engineered barriers in a deep geological repository.

2 Models and methods

ClaySor 2023 embodies the two-site protolysis non-electrostatic surface complexation and cation exchange (2SPNE SC/CE) sorption model as consistently implemented in the GEM-Selektor modelling software with the built-in thermodynamic database (currently TDB 2020). A brief description of the model, as well as its special case, the Generalised Caesium Sorption (GCS) model, with references to the detailed description, is given below.

The 2SPNE SC/CE non-electrostatic sorption model (Bradbury & Baeyens 1997, 2009a) was widely and successfully used for more than two decades to describe, in terms of mass action relations, the adsorption of dissolved metal species on the 2:1 clay minerals montmorillonite and illite (Fig. 2-1). This occurs through a combination of electrostatic binding at planar sites (cation exchange) and a pH-dependent inner-sphere surface complexation at the amphoteric surface hydroxyl functional groups.

"Non-electrostatic" means that the electrostatic (Coulomb) term $[\exp\left(\frac{zF\Psi}{RT}\right)]$, (where z is the surface species charge, F (= 96,485 C mol^{-1}) is the Faraday constant, Ψ (in V) is the relative electrostatic potential on the mineral-water interface, R (= 8.3145 J K^{-1} mol^{-1}) is the universal gas constant, and T is temperature in K), was omitted from the activity and mass action equations of surface complexation reactions in order for the calculations to reproduce the measured R_d values within investigated ranges of experimental conditions. This implys that the chemical contribution to the adsorption free energy predominates over the electrostatic contribution (Bradbury & Baeyens 1997).

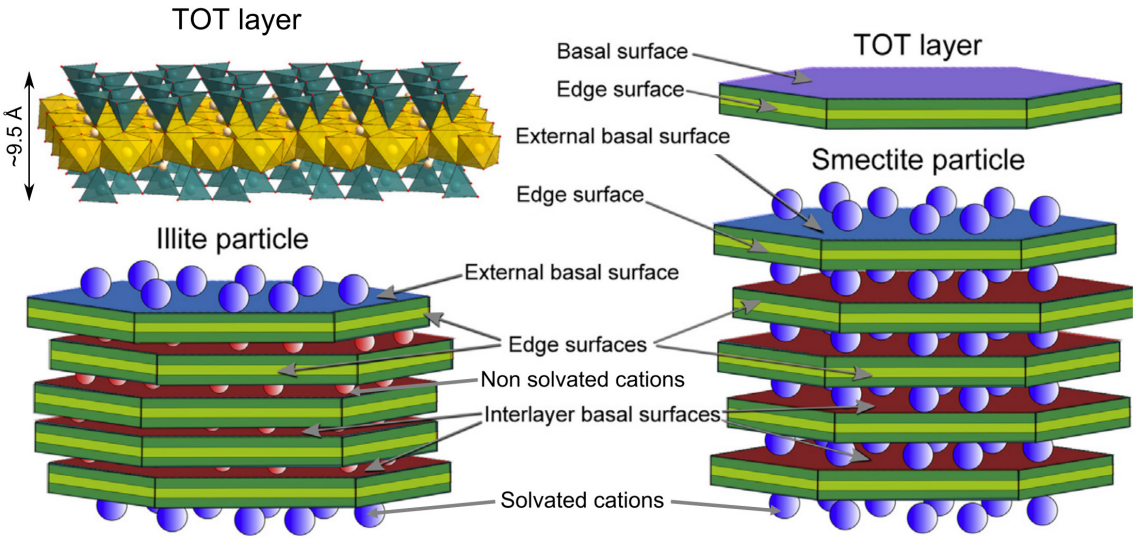

Fig. 2-1: Basic crystal structures of 2:1 clay minerals (illite and smectite) with two characteristic tetrahedral sheets for each octahedral sheet (TOT) and illustrating the positions of the edge and surfaces

Modified from Tournassat et al. (2015).

2.1 Cation exchange

The permanent excess negative charge in 2:1 clay minerals, caused by isomorphic substitutions of Al^{3+} by divalent cations in octahedral (O) layer sites and/or of Si^{4+} by Al^{3+} in tetrahedral (T) layer sites in the lattice, is compensated by the electrostatic binding of cations (Na^+, K^+, Cs^+, Ca^{2+}, Mg^{2+}, etc.) from the aqueous solution to the planar sites that are assumed to maintain charge neutrality. These cations can undergo reversible exchange with other aqueous cations, thus providing the dominant adsorption mechanism for alkaline and alkaline-earth elements on illite and montmorillonite. For the divalent and trivalent elements such as Ni(II), Am(III) and Eu(III), cation exchange may become a dominant adsorption mechanism at low ionic strength and low pH (< 4) and can contribute to sorption at higher sorbate concentrations and pH when strong edge sites become saturated.

Each clay mineral is characterised by its cation exchange capacity (CEC); defined as the total moles of charge of sorbed exchange cations per unit mass of clay, e.g., equivalents·kg^{-1}. This parameter is derived from the planar site saturation experiments (Baeyens & Bradbury 2004) and is fixed in the model. The generic cation exchange reaction can be written as:

$$z_B A^{z_A}\text{-}clay + z_A B^{z_B} \leftrightarrow z_A B^{z_B}\text{-}clay + z_B A^{z_A} \tag{2-1}$$

where B is a cation with valence z_B in the aqueous phase that is in exchange with cation A, with valence z_A, bound to the clay mineral surface.

This reaction corresponds to a mass action equation, expressed as the selectivity coefficient ${}^{B}_{A}K_C$:

$${}^{B}_{A}K_C = \frac{(E_B)^{z_A}}{(E_A)^{z_B}} \cdot \frac{\{A\}^{z_B}}{\{B\}^{z_A}} \tag{2-2}$$

where {} denotes the activity of ions (A or B) in aqueous solution, E_A and E_B are the equivalent fractional occupancies (in the Gaines & Thomas convention (Gaines & Thomas 1953)), defined as the charge equivalents of A (or B) sorbed per unit mass of solids divided by the CEC. Replacing equivalent fractional occupancies with the mole fraction occupancies X_A and X_B leads to another mass action expression in the Vanselow convention (Vanselow 1932), with the equilibrium constant ${}^{B}_{A}K_V$ (if ion exchange is treated as a phase-solution with simple ideal mixing):

$${}^{B}_{A}K_V = \frac{(X_B)^{z_A}}{(X_A)^{z_B}} \cdot \frac{\{A\}^{z_B}}{\{B\}^{z_A}} \tag{2.3}$$

In GEMS, the selectivity coefficient values are expressed in the Vanselow convention, while in PHREEQC and most publications, the Gaines & Thomas convention is applied. Thus, in this report, the selectivity coefficients are given in both conventions to remain consistent with previous works and allow calculations to be performed in GEMS.

It can be shown that for any homovalent ion exchange reaction with $z_A = z_B$, ${}^{B}_{A}K_V = {}^{B}_{A}K_C$ because $X_A = E_A$ and $X_B = E_B$. However, this is not true for heterovalent ion-exchange reactions. As shown in Curti (2023), for $z_A = 1$ and $z_B = 2$, the reported Gaines-Thomas exchange coefficient ${}^{B}_{A}K_C$ can be converted into the Vanselow equilibrium constant ${}^{B}_{A}K_V$ using the equations:

$${}^{B}_{A}K_V = {}^{B}_{A}K_G \frac{1}{2(1+X_B)} \tag{2.4}$$

$${}^{B}_{A}K_V = {}^{B}_{A}K_G \frac{2-E_B}{4} \tag{2.5}$$

When $z_A = 1$ and $z_B = 3$, the conversions (derived as shown in Curti (2023)) will be

$${}^{B}_{A}K_V = {}^{B}_{A}K_G \frac{1}{3(1+2X_B)^2} \tag{2.6}$$

$${}^{B}_{A}K_V = {}^{B}_{A}K_G \frac{(3-2E_B)^2}{9} \tag{2.7}$$

As seen from Equations (2.4) to (2.7), both conversions depend on the composition of ion-exchange phases, expressed either in the mole fraction of B (di- or trivalent cation) or in the equivalent fraction of B. Usually, cation A is monovalent (Na^+) and greatly exceeds other cations in porewater and on illite or montmorillonite. At minor or trace fractions of di- or trivalent cation B, $X_B \rightarrow 0$, $E_B \rightarrow 0$, so approximately

$${}^{B}_{A}K_V \approx \frac{1}{z_B} {}^{B}_{A}K_G \tag{2.8}$$

This is the case for cations such as Ba^{2+}, Sr^{2+}, Ra^{2+}, Fe^{2+}, Mn^{2+}, Am^{3+}, Cm^{3+}, etc. However, in experiments, major cations Ca^{2+} and Mg^{2+} can be present in significant fractions on ion exchange, therefore, Equations (2.4) to (2.7) must be used with the awareness of these equivalent fractions, as these are essential for accurate conversions of the reported Gaines-Thomas selectivity coefficients into Vanselov equilibrium constants required for GEMS calculations.

The selectivity coefficient values are derived from adsorption experiments, mainly carried out under low pH and low ionic strength. In the current work, the experiments carried out on homo-ionic Na-illite and Na-montmorillonite in background solutions with Na^+ as a main cation were used for modelling. Thus, all ion-exchange reactions and selectivity coefficients assume Na^+ as the reference cation.

2.2 Surface complexation

The amphoteric surface hydroxyl groups that exist on clay platelet edges (Sposito 1984, Davis & Kent 1990) can be illustrated as being attached to different site types (≡S^SOH is a strong site and ≡S^{W1}OH and ≡S^{W2}OH are weak sites) with their associated apparent protonation and deprotonation constants, K_{app}^{+} and K_{app}^{-}, respectively.

The protolysis reactions and the corresponding equilibrium constants are given as:

$$\equiv SOH + H^+ \leftrightarrow \equiv SOH_2^+ \qquad K_{app}^{+} = \frac{[\equiv SOH_2^+]}{[\equiv SOH]\cdot\{H^+\}} \tag{2.9}$$

$$\equiv SOH \leftrightarrow \equiv SO^- + H^+ \qquad K_{app}^{-} = \frac{[\equiv SO^-]\cdot\{H^+\}}{[\equiv SOH]} \tag{2.10}$$

where [] denotes molar concentrations and {} denotes activities.

The surface complexation of metal cations on clays at trace concentrations are assumed to occur mainly on the strong sites that have a higher affinity but low amounts per unit mass of clay minerals (site capacity). This was determined by fitting the concentration-dependent sorption data of given nuclides. The weak sites affect adsorption at higher concentrations due to their high site capacities, which were determined based on clay mineral acid-base titration data. Modelling of the titration data indicated that the two weak site types ≡S^{W1}OH and ≡S^{W2}OH are involved in protolysis reactions. These sites are assumed to have equal site capacities but exhibit different protolysis constants. Due to the low capacity of strong sites, their protolysis constants cannot be estimated from acid-base titrations, so they are assumed to be equal to the respective values for weak sites ≡S^{W1}OH (Bradbury & Baeyens, 1997). In the following, the clay-specific parameters of the 2SPNE SC/CE sorption model (site capacities and protolysis constants) are considered as fixed non-adjustable parameters, as given in Tab. 2-1.

Tab. 2-1: Summary of 2SPNE SC/CE model parameters (site types, site capacities and protolysis constants) for illite (Bradbury & Baeyens 2009a) and montmorillonite (Baeyens & Bradbury 1997)

	Illite		**Montmorillonite**	
Site type	Capacity (mol kg^{-1})			
≡S^SOH	$2.0 \cdot 10^{-3}$			
≡S^{W1}OH	$4.0 \cdot 10^{-2}$			
≡S^{W2}OH	$4.0 \cdot 10^{-2}$			
Protolysis reactions	$\log_{10}K_{app}$			
	≡$S^{S/W1}$OH	≡S^{W2}OH	≡$S^{S/W1}$OH	≡S^{W2}OH
≡SOH + H^+ ⇔ ≡SOH_2^+	4.0	8.5	4.5	6.0
≡SOH ⇔ ≡SO^- + H^+	-6.2	-10.5	-7.9	-10.5

The basic assumption associated with the 2SPNE SC/CE sorption model is that only cations and neutral and positively charged hydroxy species sorb on the edge surface sites; all other aqueous species are considered non-sorbing (Bradbury & Baeyens 2017). Although ternary carbonate surface complexes of trivalent metals confirmed by EXAFS investigations (Marques Fernandes et al. 2008, 2012, 2015) have been used to model their sorption on clay minerals under specific conditions, they seem to be irrelevant at the pH range (6.8 to 7.4) of porewaters related to prospective sites for the deep geological repository (Kulik & Miron 2024), and thus are not included in the present sorption thermodynamic database.

The surface complexation reaction of an aqueous cation Me^z on the hydroxyl group of clay edge can be written as:

$$\equiv SOH + Me^z + yH_2O \leftrightarrow \equiv SOMe(OH)_y^{z-(y+1)} + (y+1)H^+ \tag{2.11}$$

where Me^z denotes metal with valence z, and y is an integer.

The equilibrium surface complexation constant for Equation (2.11) is given as:

$$K_y = \frac{[\equiv SOMe(OH)_y^{z-(y+1)}]}{[\equiv SOH]} \cdot \frac{f_{\equiv SOMe(OH)_y^{z-(y+1)}}}{f_{\equiv SOH}} \cdot \frac{\{H^+\}^{(y+1)}}{\{Me^z\}} \tag{2.12}$$

where f denotes surface activity coefficients whose ratio is assumed to be unity.

As the reaction as given in Equation (2.11) is of the hydrolysis type, the surface complexation constants of the interacting cation are related to its stability and its aqueous hydrolysis complexation constants. Therefore, the present sorption thermodynamic database can only be applied to the sorption modelling when it is consistent with the chemical thermodynamic database used to model the experiments.

2.3 Generalised caesium sorption (GCS) model on illite

The generalised caesium sorption (GCS) model (Bradbury & Baeyens 2000) applied in this work (in GEMS ClaySor implementation) is based on the three-site cation exchange model of Cs sorption on illite (Brouwer et al. 1983). This was developed to predict Cs sorption on argillaceous rocks in different water chemistries and illite contents. The cation exchange of Cs on illite is assumed to occur on three sites. The high-affinity/low-capacity "frayed edge sites" (FES) are responsible for the uptake of Cs at low concentrations. The other two site types were identified at the surface of the illite crystallites by means of nuclear magnetic resonance spectroscopy (Kim et al. 1996) and are referred to as type II sites (T2S) and to the low-affinity/ high-capacity planar sites (PS). The GCS model parameters, including capacities for three sites (fixed model parameters), as well as selectivity coefficients for Cs^+ (re-estimated in this work) and the main competing cations K^+, Ca^{2+}, NH_4^+, Mg^{2+}, and Sr^{2+} with respect to Na^+ (taken from literature), are given in App. A, Tab. A-1.

In the GEM-Selektor modelling software, the GCS model is implemented by introducing two additional independent components (IC) for FES and T2S, with the respective reference Na-exchange dependent components (DC) and other chemical species defined via cation exchange reactions similar to those for the main planar sites (PS). The site capacities (per kg of illite) were set in a separate predefined composition object, "NaIlliteCs", in line with Bradbury & Baeyens (2000). The species defined by cation exchange reactions on those sites are enclosed in two separate phases. One phase, "IlliteX", includes Cs cation exchange species on planar sites, as well as similar species of other elements with refitted or previously set equilibrium constants following

the Vanselow convention. Another phase, "IlliteCsNa", comprises cation exchange species of Cs and other monovalent and divalent cations such as K^+, NH_4^+, Ca^{2+}, Mg^{2+}, Sr^{2+} on FES and T2S (App. A, Tab. A-1). This phase is only used in calculations of Cs pH edges and adsorption isotherms on illite.

2.4 ClaySor: 2SPNE SC/CE model implementation in GEM-Selektor

This section provides the basic concepts and definitions that are relevant for this study. The detailed description of the implementation procedure for the 2SPNE SC/CE model into the GEM-Selektor code and databases, known as the ClaySor model, can be found in Kulik et al. (2018).

The conceptual difference between the earlier 2SPNE SC/CE model and its current GEMS implementation is that in the former, adsorbed species were treated analogously to aqueous complexes (with the sorption site as a ligand) as part of the aqueous electrolyte phase. In contrast, in the GEMS ClaySor model, ion-exchange species for a clay mineral (e.g., illite) are treated as endmembers of a separate ion-exchange phase, in turn treated as a solid solution with simple ideal mixing. Edge adsorption species are components of a separate surface complexation phase and are also treated as a simple ideal solid solution. Within each sorption phase, the mole amounts of surface complexes on strong as well as weak-1 and weak-2 sites are additionally constrained by the respective mass balances set by total mole amounts of independent components for each site type in the input bulk composition of the chemical system.

In the GEM-Selektor modelling software, chemical systems are usually considered in the elemental stoichiometry basis, in which the system bulk composition is given as mole amounts of independent components (IC), usually chemical elements and electrical charges. For ClaySor models, the sorption sites are represented as additional ICs ("fictive elements"). The following ICs are set for illite and montmorillonite:

- `Clai`, `Clfei`, `Cltti` – permanent charge sites of valence -1 on illite involved in cation exchange reactions: planar sites (PS), frayed edge sites (FES), type II sites (T2S), respectively;
- `Clay` – permanent charge planar site of valence -1 on montmorillonite;
- `Essi`, `Esvi`, `Eswi` – amphoteric edge sites on illite: strong sites $\equiv S^S$, weak sites $\equiv S^{W1}$ and $\equiv S^{W2}$, respectively, all of valence +1;
- `Ess`, `Esv`, `Esw` – edge sites on montmorillonite: strong sites $\equiv S^S$, weak sites $\equiv S^{W1}$ and $\equiv S^{W2}$, respectively, all of valence +1.

Permanent charge sites are also assigned with the molar mass (in g mol^{-1}), roughly estimated as the mass (in g) of the respective (dry) clay with 1.0 eq permanent charge: 1,126.346 g mol^{-1} for `Clay` (PS on montmorillonite) and 4,421.1 g mol^{-1} for `Clai` (PS on illite; molar mass for `Clfei` and `Cltti` is assumed to be identical). This is necessary because, in ClaySor, the clay sorbent (illite or montmorillonite) is represented only in amounts of "fictive elements" proportional to site capacities and the mass of (dry) clay, but not in the real elemental stoichiometry. The molar mass of edge sites is arbitrarily set to 1 g mol^{-1}. These molar masses propagate into sorption species and are useful in setting compositions of clay systems in terms of solid/water mass ratios.

The chemical system definition in GEMS is composed of phases (aqueous electrolyte, gas mixture, pure condensed phases, liquid or solid solutions, sorption phases, etc.). A phase or phase-solution includes one or more dependent components (DC), respectively (chemical species, components, endmembers). Activities and concentrations of DCs are defined separately for each phase, according to universally accepted conventions and concentration scales (e.g., molality for aqueous species, mole fraction for endmembers of other solutions). Each DC is defined by a chemical formula expressed in moles of IC per one mole of DC concerned. The stability of each

DC is set by its standard molar Gibbs energy G^o_{298} (of formation from ICs taken at the appropriate standard and reference states) at reference temperature T_r = 298.15 K (25 °C) and pressure P_r = 1 bar and, if necessary, corrected to the temperature T and pressure P of interest. The following reference DCs are set for illite and montmorillonite in the GEMS database for the ClaySor model:

- `ClaiNa@`, `ClfeiNa@`, `ClttiNa@` – cation exchange species representing the Na^+ ion on the permanent charge site of illite: planar sites (PS), frayed edge sites (FES), type II sites (T2S), respectively;
- `ClayNa@` – cation exchange species representing the Na^+ ion on permanent charge planar sites of montmorillonite;
- `=iSsOH@`, `=iSvOH@`, `=iSwOH@` – representing amphoteric OH groups on edge sites of illite: strong sites $\equiv S^SOH$, weak sites $\equiv S^{W1}OH$ and $\equiv S^{W2}OH$, respectively. In the following, the sign "=" will be used in the edge sites notation along with the traditionally used "≡", as the former corresponds to the representation of edge sites in the GEMS and GEMSFITS software;
- `=SsOH@`, `=SvOH@`, `=SwOH@` – representing amphoteric OH groups on edge sites of montmorillonite: strong sites $\equiv S^SOH$, weak sites $\equiv S^{W1}OH$ and $\equiv S^{W2}OH$, respectively.

The stoichiometries and the provisional standard-state thermodynamic properties of the reference DC species, set to be roughly consistent with those of related aqueous species, are listed in Tab. 2-2 and Tab. 2-3 and stored as DComp records in GEMS databases. Standard properties of all other exchange cations and edge surface complexes are defined via the 2SPNE SC/CE reactions according to Equations (2.1), (2.9), (2.10), (2.11) and stored in ReacDC records in the GEMS databases (see App. A).

The aforementioned species, names and acronyms are used in the following sections to describe cation exchange and surface complexation reactions and to graphically demonstrate the partitioning of (ad)sorbed forms of elements on clay sorption sites on plotted pH edges and isotherms.

Tab. 2-2: Provisional standard-state properties of ClaySor reference DC chemical species for Na-montmorillonite at 1 bar, 25 °C

Species name	Formula	Molar mass, g mol^{-1}	G^o_{298} kJ mol^{-1}	V^o_{298} cm^3 mol^{-1}
`ClayNa@`	ClayNa	1,172.99	-251.92	428.47
`=SsOH@`	EssOH@	18.0153	-237.18	18.07
`=SvOH@`	EsvOH@	18.0153	-237.18	18.07
`=SwOH@`	EswOH@	18.0153	-237.18	18.07

In species names and formulae, "@" stands for zero charge. G^o_{298} of `ClayNa@` is set to be identical to that of the Na^+ aqueous ion (in the TDB 2020 for GEMS) plus 9.96 kJ mol^{-1} (conversion from the unimolal to the unimolar "pure-substance" standard state); V^o_{298} corresponds to the dry density of Na-montmorillonite (2.73 g cm^{-3}). The properties of `=SsOH@`,`=SvOH@`,`=SwOH@` species are set to be identical to that of liquid H_2O.

Tab. 2-3: Provisional standard-state properties of ClaySor reference DC chemical species for Na-illite at 1 bar, 25 ºC

Species name	Formula	Molar mass, g mol^{-1}	G^{o}_{298} kJ mol^{-1}	V^{o}_{298} cm^3 mol^{-1}
ClaiNa@	ClaiNa	4,443.99	-251.92	1,626.6
ClfeiNa@	ClfeiNa	4,443.99	-251.92	1,626.6
CltiNa@	CltiNa	4,443.99	-251.92	1,626.6
=iSsOH@	EssiOH@	18.0153	-237.18	18.07
=iSvOH@	EsviOH@	18.0153	-237.18	18.07
=iSwOH@	EswiOH@	18.0153	-237.18	18.07

In species names and formulae, "@" stands for zero charge. G^{o}_{298} of ClaiNa@, ClfeiNa@, CltiNa@ is identical to that of the Na^+ aqueous ion plus 9.96 kJ mol^{-1} (conversion from the unimolal to the unimolar "pure-substance" standard state); V^{o}_{298} corresponds to the dry density of illite (2.73 g cm^{-3}). All properties of =iSsOH@,=iSvOH@,=iSwOH@ species are set to be identical to that of liquid H_2O.

In the TDB 2020, the specific ion-interaction theory (SIT) is chosen for estimating activity coefficients of aqueous species (Hummel & Thoenen 2023). The available interaction coefficients data allow modelling of laboratory systems for NaCl and $NaClO_4$ background media in the range of 0.01 M to 1 M for all the datasets (Tab. D-1, Tab. E-1). Considering the range in IS for the majority of the data used for the model evaluation, the applicability of the selectivity coefficients is suitable between ~ 0.01 and ~ 0.3 M and for protolysis and surface complexation constants between ~ 0.01 and ~ 0.5.

In this work, separate datasets with KCl, KNO_3, or $NaNO_3$ as a background electrolyte were included into the fitting (see App. C) without considering interaction coefficients between sorbate and electrolyte ions. Preliminary tests conducted with interaction coefficients found in the literature showed a negligible difference in R_d (< 0.024 $\log_{10}$K) compared to values obtained without interaction coefficients at the relatively low concentration of electrolytes (< 0.3 M). Since this difference in R_d was incomparably smaller than the scatter of experimental data, the afore-mentioned datasets were also taken into account in the fitting.

3 Model parameter optimisation and estimation of uncertainties

The optimal values for the apparent standard molar Gibbs free energy of surface complexes and cation exchange species ($G°_{298}$) in the ClaySor 2023 model are derived using the versatile GEMSFITS parameter optimisation tool (Miron et al. 2015). GEMSFITS is capable of concurrently refining multiple parameters, including thermodynamic constants, against a variety of experimental datasets. It employs the GEMS3K code (Kulik et al. 2013, Wagner et al. 2012) internally to compute the equilibrium speciation for each experimental data point.

The $G°_{298}$ values of surface complexes and cation exchange species were obtained by fitting several pH-dependent (pH edge) and concentration-dependent sorption data (isotherms) simultaneously. The adjusted values of $G°_{298}$ can then be used in GEMS or transformed into equilibrium constants for surface complexation and cation exchange reactions. GEMSFITS incorporates various statistical methods for assessing parameter correlation, overall parameter sensitivity to experimental data, and a Monte Carlo approach to determine parameter uncertainties.

Experimental datasets were transformed into the GEMSFITS experimental data format using predefined Excel spreadsheets that list the input and output for each experiment data point. The input includes details such as the volume of aqueous solution, background electrolyte concentration, pH, quantity of clay, cation exchange capacity, and edge site capacities. The output is denoted by the experimentally determined solid–liquid distribution coefficients R_d:

$$R_d = \frac{C_{in.} - C_{eq.}}{C_{eq.}} \cdot \frac{V}{m} \tag{3-1}$$

where $C_{in.}$ is the initial aqueous concentration of the metal ion (mol·L^{-1}), $C_{eq.}$ is the equilibrium aqueous metal concentration (mol·L^{-1}), V is the volume of liquid phase (L) and m is the mass of solid phase (kg). To avoid overfitting of high-sorption relative to low-sorption values, R_d values were converted into the logarithmic scale ($\log_{10}R_d$) for the optimisation procedures.

The chemical system setup, as well as the preliminary "goodness of fit" evaluation, were carried out using the GEMS software. As the first approximation, the previous models were applied to describe the experimental data. At this stage, it is possible that some observations from datasets were excluded from the considerations based on the GEMS calculation results due to, for instance, high probability of metal precipitation under certain conditions. The chemical system and the experimental datasets were exported to GEMSFITS for the subsequent simultaneous fitting.

The $G°_{298}$ values of surface complexes and cation exchange species were the input adjustable parameters. The measured $\log_{10}R_d$ values were compared with the calculated $\log_{10}R_d$ values. The objective function was a normalised sum of the squares of the residuals:

$$S = \sum_{i=0}^{n} \frac{(\log_{10}Rd_{measured} - \log_{10}Rd_{calcuated})^2}{\log_{10}Rd_{measured}^{\ 2}} \tag{3-2}$$

where n is the number of data points. During the optimisation procedure, the nested GEMSFITS function was used to constrain pH in the system via titration with acid or base until the experimental pH value was reached (Miron et al. 2015).

All datasets for each element were applied simultaneously to derive optimum values for $G°_{298}$ of surface complexes and cation exchange species in the ClaySor 2023 model, along with their respective uncertainties at the 95% confidence level as follows:

1. The $G°_{298}$ values are simultaneously fitted using the BOBYQA nonlinear optimisation algorithm (Powell 2009) from the NLOpt library (Johnson 2007) used in the GEMSFITS code package. This algorithm performs derivative-free bound-constrained minimisation using an iteratively constructed quadratic approximation of the least squares objective function in accordance with Equation (3-2). The initial guess for $G°_{298}$ values was derived from $\log_{10}K$ values of sorption reactions taken from the previous studies. When new sorption species were introduced that had not been previously used in the model, their initial $G°_{298}$ values were approximated using the linear free energy relationship (LFER) approach. Usually, the $G°_{298}$ boundaries of ±10 kJ mol^{-1} were wide enough to locate the minimum of the objective function. In some cases, one of the $G°_{298}$ parameters was fixed to the previously estimated value (i.e., Zn selectivity coefficient on illite and montmorillonite) due to unreliable data in the respective part of the sorption edge or isotherm without affecting the quality of the fit, but better constraining it.

2. During the optimisation procedure, the composite scaled sensitivities (CSS) (Miron et al. 2015, Hill & Tiedeman 2007) of the $G°_{298}$ values were evaluated. These metrics are available from the results of GEMSFITS and represent the sum of all observation sensitivities for a given parameter and describe how well a parameter is constrained by the experimental data. Any parameters with a low sensitivity could be removed from the model. Step 1 was then repeated with the simplified model and only with those parameters that are necessary to describe the observations. If the objective function minimum for the new model was significantly higher compared to the old one, the parameter was then returned to the model. The details of CSS determination are described in Miron et al. (2015).

   Once the optimised values of the parameters ($G°$) were determined, Monte Carlo simulations were performed to derive the uncertainty of the parameters represented by the 95% confidence interval. The Monte Carlo sampling method can be used for evaluating the error propagation and for estimating the parameter uncertainty when these two steps cannot be carried out using analytical propagation formulae in a straightforward way. This method (details in Miron et al. 2015) allows the assessment of the uncertainty at the 95% confidence level of each adjusted parameter as twice the standard deviation of parameter values obtained by repeating the fit for many (usually 1,000) synthetic experimental datasets.

3. These synthetic datasets were generated by modifying the measured values with quantities randomly sampled from a log-normal distribution with mean zero and data residual Δ from the data scatter or the experimental error (Δ_{exp}). They were calculated as follows:

$$\Delta = |log_{10}R_{d\,meas} - log_{10}R_{d\,calc}| \tag{3-3}$$

   where $R_{d\,meas}$ and $R_{d\,calc}$ refer to the measured and calculated best-fit R_d values, respectively.

$$\Delta_{exp} = |log_{10}\sigma_{exp}| \tag{3-4}$$

where σ_{exp} refers to the experimental error of R_d, which was at expert level evaluated as 30% of the R_d value for $R_d < 1 \times 10^5$ and 50% of the R_d value for $R_d \geq 1 \times 10^5$. On a logarithmic scale, these values form asymmetric error intervals: (+0.11 – 0.15) and (+0.18 – 0.3), respectively. Since the resulting R_d uncertainty values require only symmetric values in the logarithmic scale, the larger value was used for calculations as the more conservative option. Thus, σ_{exp} values of 0.15 for $R_d < 1 \times 10^5$ and 0.3 for $R_d \geq 1 \times 10^5$ were applied to generate synthetic datasets.

To avoid underestimating the parameter confidence interval for metals for which only scarce data were available, i.e. Th, Sn, Pa, Ra, and Am, synthetic datasets were created based on experimental error.

4. Fitting against the synthetic datasets yielded 1,000 new sets of best-fit $G°_{298}$ values. For the obtained G^0_{298} values, their uncertainty at the 95% confidence level is approximated by:

$$Un_{G^\circ_{298}} = 1.96 \times \sigma \tag{3-5}$$

where σ is the standard deviation, and 1.96 is the z-score corresponding to the 95% confidence level:

$$-1.96 \times \sigma < \overline{G^\circ_{298}} < 1.96 \times \sigma \tag{3-6}$$

where $\overline{G^\circ_{298}}$ is the mean of 1,000 best-fit $G°_{298}$ values, and 95% of estimated parameter values lie within 1.96 standard deviations of the mean.

In some ranges of pH or sorbate concentrations, the contributions of different surface complexes may overlap to different degrees, leading to correlated parameters and wider confidence intervals. To reduce the uncertainty and on a case-by-case basis, one of the correlated parameters could be excluded from the model if no significant effect on the fit was observed.

The fitted $G°_{298}$ values of surface complexes and cation exchange species were converted into equilibrium constants of surface complexation and cation exchange reactions via the standard Gibbs free energy of reaction $\Delta_r G^\circ_{298}$, according to Equations (3-7) and (3-8).

$$\Delta_r G^\circ_{298} = \Sigma G°_{298(\text{products})} - \Sigma G°_{298(\text{reactants})} \tag{3-7}$$

where $\Sigma G°_{298(\text{reactants})}$ is the sum of standard molar Gibbs free energies of formation of reactants in surface complexation or the cation exchange reaction in $J \cdot mol^{-1}$. Conversion to $\log_{10}K°$ is then:

$$\log_{10}K° = \frac{\Delta_r G^\circ_{298}}{-R \cdot T° \cdot \ln(10)} \tag{3-8}$$

where R is the gas constant in $J \cdot mol^{-1} \cdot K^{-1}$, and T^o is the reference temperature, 298.15 K.

Uncertainties at the 95% confidence level of surface complexation and cation exchange reaction constants $Un_{K_{SC/CE}}$ were calculated as:

$$\log_{10} Un_{K_{SC/CE}} = \left| \frac{Un_{G^{\circ}_{298}}}{-RTln(10)} \right| \quad (3\text{-}9)$$

where $Un_{G^{\circ}_{298}}$ is the uncertainty at the 95% confidence level of best-fit $G°_{298}$ values.

The optimised parameters for sorption species and reactions with uncertainties evaluated as described above are provided in App. A.

Based on the estimated uncertainties of the optimised parameters, the overall uncertainty of the sorption model was propagated to the 95% confidence interval of the resulting R_d values, shown as the blue band on the pH edge and isotherm plots in Chapter 4. This band was evaluated for each plot with help of the in-house UpsaGEMS Python code (PSI LES 2022 annual progress report) combining the GEMS3K code with the "Uncertainpy" toolbox (Tennøe et al., 2018). For the calculated pH edges or isotherms, "Uncertainpy" (Tennøe et al., 2018) samples many values for different parameter combinations. From within their uncertainty, and through GEMS calculations running through all combinations, a spread of calculated pH edges or isotherms is generated and then used to define the 95% confidence interval band that contains 95% of all model predictions.

The derived uncertainty of parameters at the 95% confidence level reflects how well the model is determined by the measured points. And the displayed model 95% confidence interval band provides the likelihood that it contains the model-predicted R_d values if the model would be refitted with additional measurements obtained using the exact same setup. Because the model uses a thermodynamic description that only approximates the real systems, a situation where the model will not be able to describe 95% of all data points can be expected, even with large parameter uncertainties. Therefore, 95% of the points should not be expected to lie within the band, which would, however, be expected if a prediction interval were used. The difference between the prediction interval and the confidence interval can be clarified as follows: the 95% prediction interval refers to the percentage of cases where the future experimental point will lie within the prediction interval band, whereas the 95% confidence interval refers to the percentage of cases where the future model prediction lies within the confidence band. The prediction interval could be produced in cases when using purely empirical models and when the model can accurately approximate all the mechanisms that describe the data points (e.g., logK = f(T) model type). Since, in this work, the uncertainty bands are not represented by the prediction interval, some observations may be outside the functional form of the model. This results from the approximate nature of the model that may not fully account for all processes in a complex system.

4 Results: ClaySor 2023 model performance for illite and montmorillonite

This chapter aims to demonstrate how well the ClaySor 2023 model fits the experimental data of the selected pH edges and adsorption isotherms.

The fitted pH edges and isotherms selected from datasets that were used for this purpose are shown as scatter along with the modelled curves and their 95% confidence intervals. The experimental data points are given as green circles with error bars (±0.15 for $R_d < 1 \times 10^5$ or ± 0.3 for $R_d \geq 1 \times 10^5$), the modelled curves as continuous blue lines, and the 95% confidence intervals as light-blue bands. The confidence intervals of the modelled curves were calculated with the UpsaGEMS code that, in turn, uses the xGEMS code (PSI LES 2022 annual progress report[1]) with Python API for chemical equilibrium calculations and the "Uncertainpy" (Tennøe et al. 2018) Python code to propagate parameter uncertainties with regard to the ClaySor model into the calculated R_d values. The code determines the 95% confidence interval of the model predictions by evaluating the model for a large number of input parameter values that were randomly sampled from within their determined uncertainty interval.

In this report, sorption pH edges are presented as the decimal logarithm of solid-liquid distribution coefficients (R_d; Equation (3-1)) plotted against pH, and adsorption isotherms are presented as the decimal logarithm of R_d vs. the equilibrium aqueous metal concentration C_{eq}..

Surface complexation reactions, G^o_{298} values, and equilibrium constants for metal cations on strong sites and type 1 weak sites of Na-illite and Na-montmorillonite are given in App. A, Tab. A-2 and Tab. A-3, respectively. Surface complexation reactions, G^o_{298} values, and constant values for metal cations on type 2 weak sites for Ra(II) are shown in App. A, Tab. A-1. Cation exchange reactions, G^o_{298} values, and the corresponding selectivity coefficient values (both Vanselow $\log_{10}K_V$ and Gaines-Thomas $\log_{10}K_c$ conventions) for Na-illite and Na-montmorillonite are represented in App. A, Tab. A-5 and Tab. A-6, respectively.

The metal hydrolysis constants from the TDB 2020 that were used for the modelling are listed in App. B. The summaries of batch sorption experiments used for ClaySor model parametrisation, including experimental conditions and references, are given in Tab. D-1 and Tab. E-1.

The revised ClaySor 2023 model parameters are best applied in the pH range of 4 – 10. This interval is representative for pH values expected in the porewaters of the buffer materials (except cement) and the confining geological units of the deep geological repository. In some cases, the measured data that fell outside this interval were not fitted, as it was not possible to clearly confirm sorption on clay. Outside the pH 4 – 10 range, the sorption data may be subject to distortion due to partial clay dissolution with the formation of silicon and aluminum hydroxides at low and high pH, respectively.

In some cases, equilibrium constants of surface complexation reactions that are mainly dominant under high pH were not selected for the final model. These surface complexation constants can be strongly correlated with those relevant for pH values < 10, which can then lead to an increased uncertainty in the calculated R_d values. Since the porewaters normally encountered in the geochemical systems within the near-field of a deep geological repository are characterised mainly by near-neutral pH, a decision was made to limit the number of parameters in the model (i.e., the number of surface complexation reactions) in favour of reducing the uncertainty of the R_d values. Sorption models for some elements have been simplified compared to the previous

[1] Progress Report of the Laboratory for Waste Management (2022). Nuclear Energy and Safety Department, Paul Scherrer Institute". Free download from https://www.psi.ch/en/les/annual-reports

models to be able to describe the measured sorption data with a lower number of parameters, and to reduce the confidence intervals of remaining constants. In such cases, the justification is given below.

4.1 Modelling sorption edges and isotherms on illite

4.1.1 Caesium

The Cs(I) sorption data used for modelling sorption on illite were taken from Brouwer et al. (1983), Comans et al. (1991), Staunton & Roubaud (1997), and Poinssot et al. (1999). The summary of published experimental datasets used for sorption modelling is given in App. E, Tab. E-1.

The three-site GCS cation exchange model (Chapter 2) was applied to describe Cs sorption pH edges and isotherms.

The value of the selectivity coefficient for frayed edge sites (`Clfei`) ${}^{Cs}_{Na}K_c$ was estimated with a high degree of confidence due to a large number of observations in the trace concentration region (Fig. 4-1). In contrast, far fewer experiments were carried out at higher Cs(I) concentrations, where both type II sites (`Cltti`) and planar sites (`Clai`) play a role. This led to a high correlation of more than 0.6 between the selectivity coefficient for type II sites ${}^{Cs}_{Na}K_c\{\text{II}\}$ and planar sites ${}^{Cs}_{Na}K_c$, resulting in high uncertainties in their values and a wide R_d confidence interval in the corresponding Cs sorption isotherm part (Fig. 4-2b).

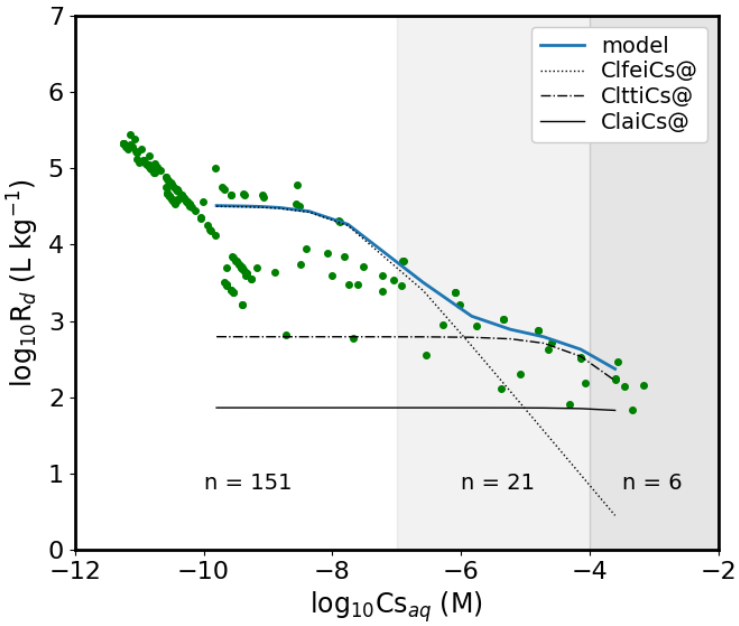

Fig. 4-1: Cs(I) sorption experiments on illite (dots) taken into consideration for the model parametrisation

The modelled sorption isotherm in 0.1 M $NaClO_4$ at pH 7 is shown to illustrate the correspondence of observations to different parts of the isotherm.

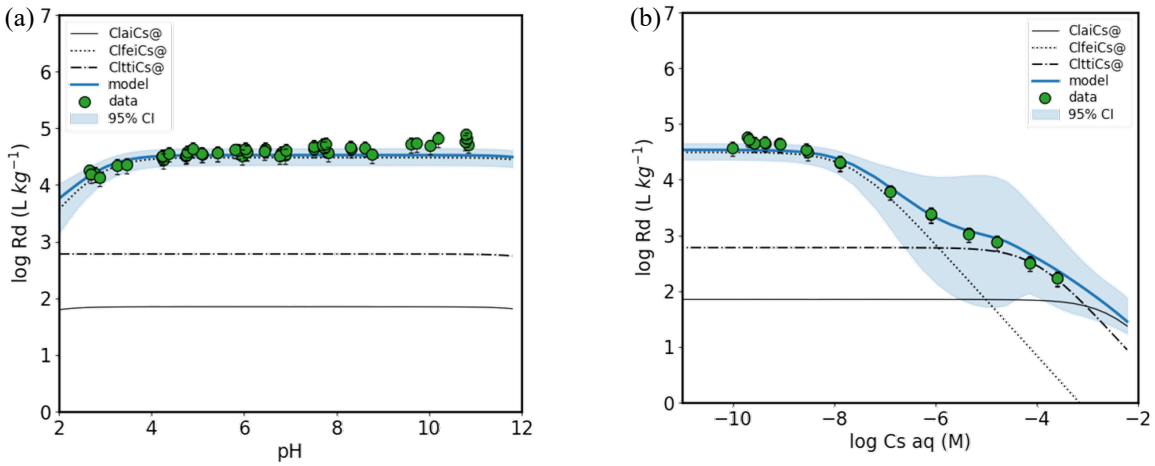

Fig. 4-2: Cs(I) sorption on Na-illite in 0.1 M $NaClO_4$

(a) pH edge and (b) sorption isotherm at pH 7, experimental data (Poinssot et al. 1999)

4.1.2 Cobalt

Co(II) sorption data used for modelling sorption on illite were taken from Marques Fernandes et al. (2015) and Montoya et al. (2018). The latter study compiles a large set of experimental data on Na-IdP (illite du Puy) comprising pH edges at different ionic strengths and isotherms at different pH carried out by various research institutes. Additionally, one unpublished in-house dataset of an isotherm at pH 7.2 was included into the fitting (Fig. 4-3b). The conditions of this experiment are outlined in App. C and App. D, Tab. D-1. The summary of published experimental datasets used in this work are given in App. E, Tab. E-1.

The aqueous thermodynamic data used for the Co(II) modelling on illite were taken from the ThermoChimie database, version 11a (Giffaut et al. 2014).

In this report, the model of Co(II) sorption on illite was simplified in comparison to the previous model (Marques Fernandes et al. 2015, Montoya et al. 2018) by eliminating the negatively charged surface complex $\equiv$iSsOCo$(OH)_2^-$ (Fig. 4-3). This caused a reduction of the predicted sorption after reaching a solution pH value of about 10. In two out of three original edge datasets used for the fitting (incl. data from Montoya et al. 2018), $\log_{10}R_d$ also decreases under pH values above 10, while only one dataset has a plateau. Thus, the updated model without the surface complex $\equiv$iSsOCo$(OH)_2^-$ is consistent with most of the experimental results.

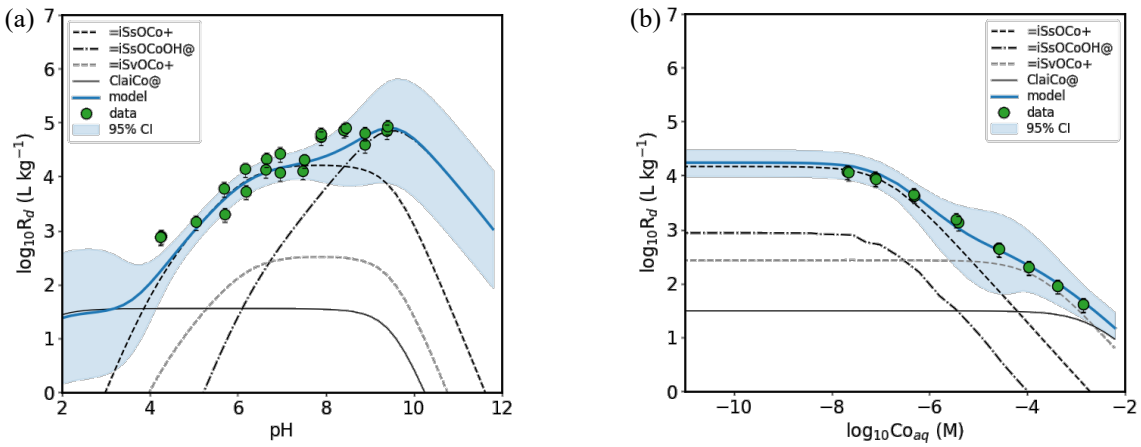

Fig. 4-3: Co(II) sorption on Na-illite in 0.1 M $NaClO_4$

(a) pH edge, experimental data (Montoya et al., 2018) and (b) sorption isotherm at pH 7.2, in-house experimental data, this work (the experimental conditions of sorption measurements are described in App. C and App. D, Tab. D-1)

4.1.3 Manganese

Mn(II) sorption data used for modelling sorption on illite were obtained as part of this work (Fig. 4-4 and App. C, Section C.2). The experimental conditions of sorption measurements and a summary of batch sorption experiments used for the modelling are given in App. C and App. D, Tab. D-1, respectively.

The proposed sorption model of Mn(II) on illite includes a cation exchange reaction on planar sites; one surface complexation reaction on strong and one on weak edge sites (Fig. 4-4). During the experiments, a blackening of illite was observed above pH 8, which could indicate the oxidation of Mn to MnO_2 by structural Fe(III) in illite. Therefore, these points were not included in the fitting, and no further surface complexation reactions were suggested.

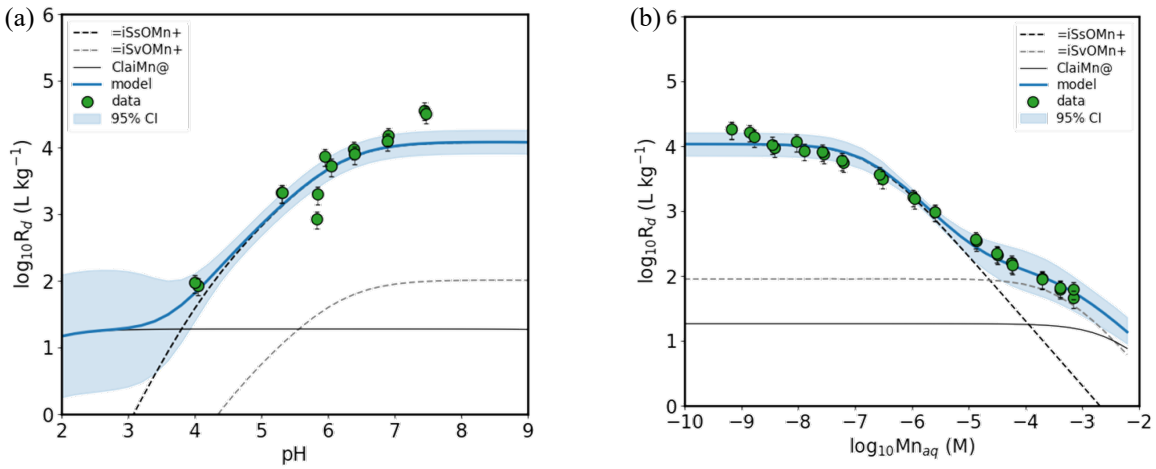

Fig. 4-4: Mn(II) sorption on Na-illite in 0.1 M NaCl

(a) pH edge and (b) sorption isotherm at pH 7.2, in-house experimental data, this work (the experimental conditions of sorption measurements are described in App. C)

4.1.4 Nickel

Ni(II) sorption data used for modelling sorption on illite were taken from Poinssot et al. (1999), Bradbury & Baeyens (2005a) and Marques Fernandes & Baeyens (2020). Additionally, unpublished in-house datasets for pH edges and isotherms were included into the fitting (Fig. 4-5b and App. C, Section C.1.3). The experimental conditions of sorption measurements are outlined in App. C and App. D, Tab. D-1. The summary of published experimental datasets used for the modelling are given in App. E, Tab. E-1.

Only two reactions were accepted for the Ni(II) surface complexation on strong edge sites (Fig. 4-5), while the previously proposed model included three reactions (Bradbury & Baeyens 2009a). This simplification is reasonable when considering the experimental points at pH values below 10 in order to reduce the interference of Ni(II) sorption on aluminium hydroxides, which may be formed as a result of illite dissolution under alkaline conditions. The proposed model fits experimental points with relatively low uncertainty values. The case of Ni(II) sorption on illite is a good example of how a high amount of experimental data points (in total, 351 points of pH edges and isotherms were used in the fitting) with low scatter can reduce the 95% confidence intervals of model parameters and of calculated R_d values.

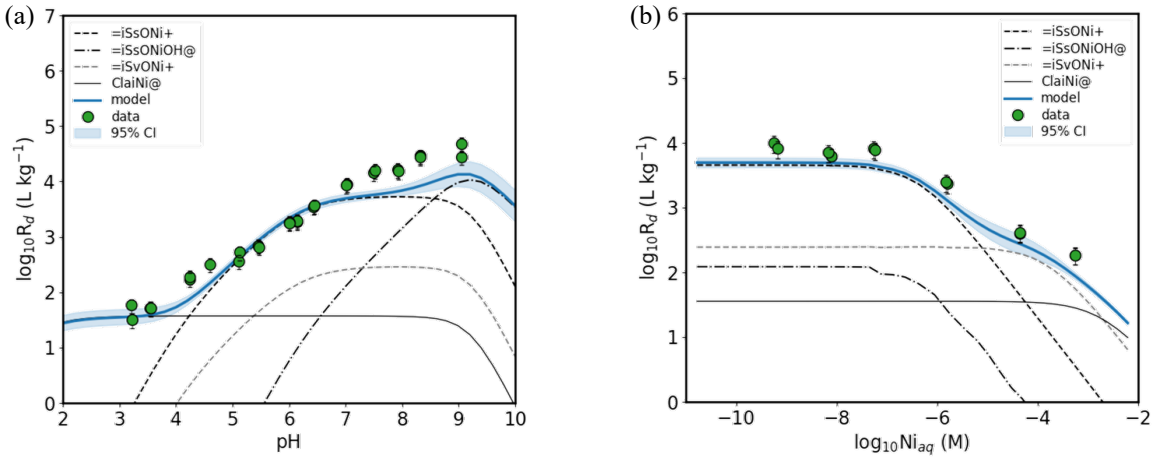

Fig. 4-5: Ni(II) sorption on Na-illite in 0.1 M $NaClO_4$

(a) pH edge, experimental data (Poinssot et al. 1999) and (b) sorption isotherm at pH 7, in-house experimental data, this work (the experimental conditions of sorption measurements are described in App. C)

4.1.5 Lead

Pb(II) sorption data used for modelling sorption on illite were taken from Marques Fernandes & Baeyens (2019). Additionally, an unpublished in-house dataset of the pH edge was included into the fitting (App. C, Section C.4). The experimental conditions of the sorption measurements are outlined in App. C and App. D, Tab. D-1. The summary of the published experimental datasets used for the modelling are given in App. E, Tab. E-1.

The sorption model of Pb(II) on illite involves one cation exchange and two surface complexation reactions (Fig. 4-6) and, in contrast to suggestions related to a previous model (Marques Fernandes & Baeyens 2019), does not imply Pb(II) sorption on the so-called "high affinity" sites. The reasons for not including "high affinity" sites in the ClaySor model is that the nature of these sites has not been established yet, and the low-pH region is less relevant for the conditions in a deep geological repository. Modelling of Pb(II) sorption in the acidic region by means of cation exchange only resulted in a higher K_c value (Tab. A-1) when compared to the model in Marques Fernandes & Baeyens (2019). The surface complexation constants for strong and weak sites have higher values as a consequence of the updated values of Pb(II) hydrolysis constants in the TDB 2020. In addition, one dataset obtained under atmospheric air conditions was excluded from fitting due to the suspected existence of Pb(II) carbonate complexes.

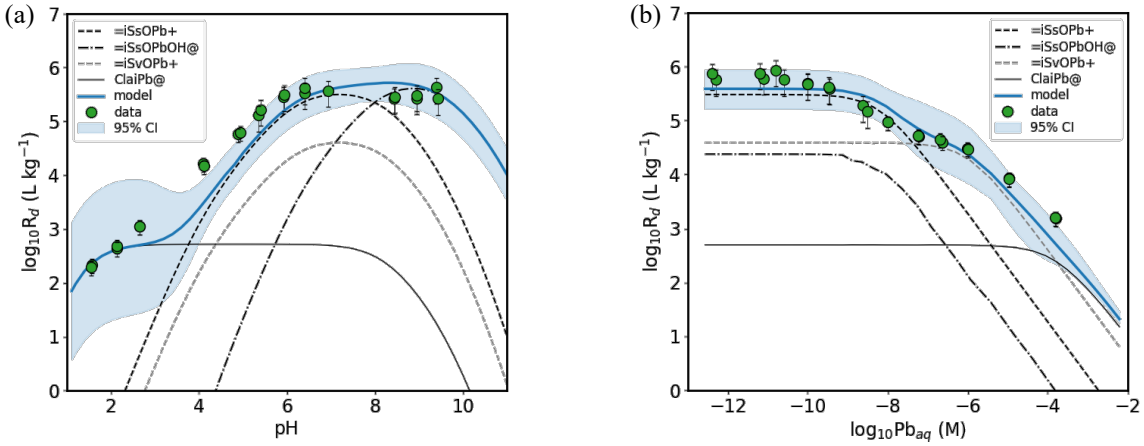

Fig. 4-6: Pb(II) sorption on Na-illite in 0.1 M NaCl

(a) pH edge and (b) sorption isotherm at pH 6.9, experimental data (Fernandes & Baeyens 2019)

4.1.6 Radium

Ra(II) sorption data used for modelling sorption on illite were taken from Marques Fernandes et al. (2023).

In the previous STDB, no Ra(II) sorption model on illite was developed (Bradbury & Baeyens 2017). Based on the fact that both illite and montmorillonite have the same 2:1 layer structure, the same model as proposed for montmorillonite (Klinkenberg et al. 2021) was also applied to illite. As Ra(II) has a very weak hydrolysis behaviour, adsorption is mainly controlled by the Ra^{2+}-Na^{+} cation exchange reaction on planar sites and, to a much lesser extent, by surface complexation on the weak sites $\equiv S^{W2}OH$, which become deprotonated at higher pH values than weak sites $\equiv S^{W1}OH$.

An initial trial of simultaneous fitting to the available datasets obtained from three different ionic strengths demonstrates a good model agreement with low ionic strength experiments (0.02 M and 0.14 M) and somewhat underpredicts the data in higher ionic strength solution (0.3 M) (Fig. 4-7).

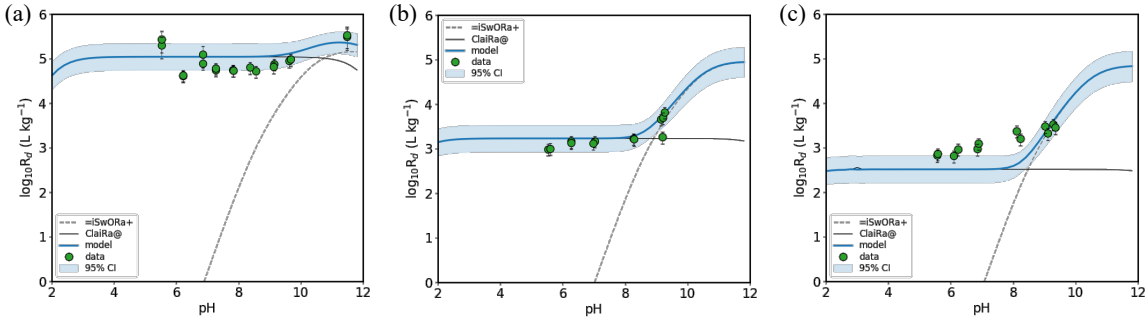

Fig. 4-7: Modelling Ra(II) sorption edge on Na-illite in solutions of different ionic strengths

(a) 0.02 M NaCl (b) 0.14 M NaCl (c) 0.3 M NaCl, experimental data (Marques Fernandes et al. 2023)

Due to poor agreement between the data for different ionic strengths, only the dataset with the highest ionic strength (0.3 M) was used for model parameterisation (Fig. 4-8). The dataset was chosen in view of the similarity to the ionic strength of porewaters expected in the siting regions for a deep geological repository, with values ranging from 0.19 to 0.5 M (Marques Fernandes et al. 2024). It should be noted, however, that in this case, the proposed model overestimates the low ionic strength data.

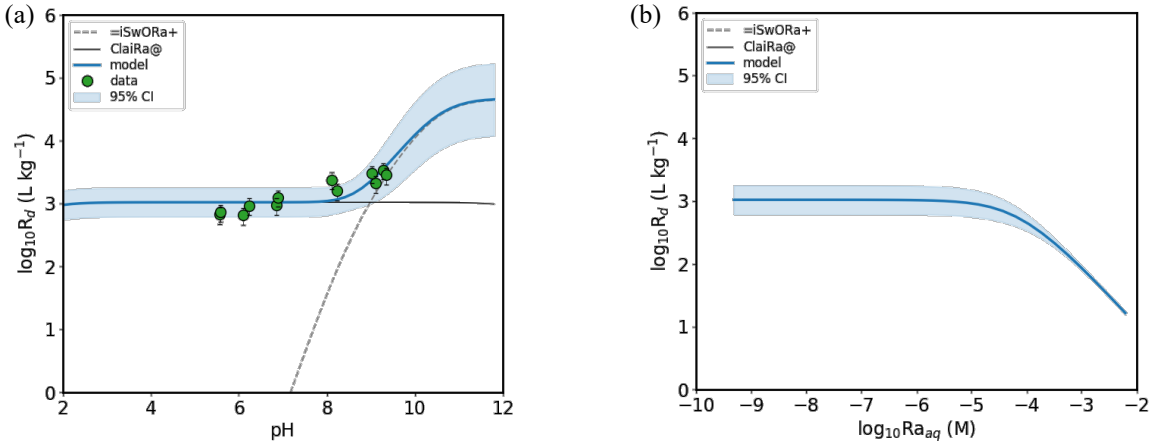

Fig. 4-8: Ra(II) sorption on Na-illite in 0.3 M NaCl

(a) pH edge, experimental data (Marques Fernandes et al. 2023) and (b) predicted sorption isotherm at pH 7 (Ra sorption isotherm data on illite are not available)

4.1.7 Zinc

Zn(II) sorption data used for modelling sorption on illite were taken from Montoya et al. (2018). The summary of published experimental datasets used for the modelling is given in App. E, Tab. E-1.

Initially, the model proposed in Montoya et al. (2018) was used to represent the Zn(II) sorption data on illite. The model included cation exchange components, as well as three surface complexation reactions on strong sites and two on weak sites. However, the simultaneous fitting to all data and uncertainty quantification yielded a wide confidence interval of more than one $\log_{10}K$ unit for the surface complex on strong sites $=iSsOZnOH^0$ that affected sorption calculations under pH conditions relevant for in-situ porewaters. In this regard, the model was simplified by eliminating the surface complex on strong sites $=iSsOZn(OH)_2^-$ and the surface complex on weak sites $=iSvOZnOH^0$. This simplification made the model consistent with the sorption models of divalent elements with similar hydrolysis behaviour, i.e., Co(II) and Ni(II).

Datasets of adsorption isotherms at pH 9 were excluded from the fit, as well as separate points of the isotherms at pH 5 that did not match the corresponding values on the pH edge.

During the fit, the value of ${}^{Zn}_{Na}K_c$ was accepted as fixed by Montoya et al. (2018), since there are no sufficient data available at low pH to re-estimate it. The high sorption values at trace concentrations and low pH (Fig. 4-9) may be caused by specific sorption on high-affinity sites as for Pb(II), the exact mechanism of which is still unclear. These uncertainties, however, do not affect the model predictions at pH values relevant for the deep geological repository.

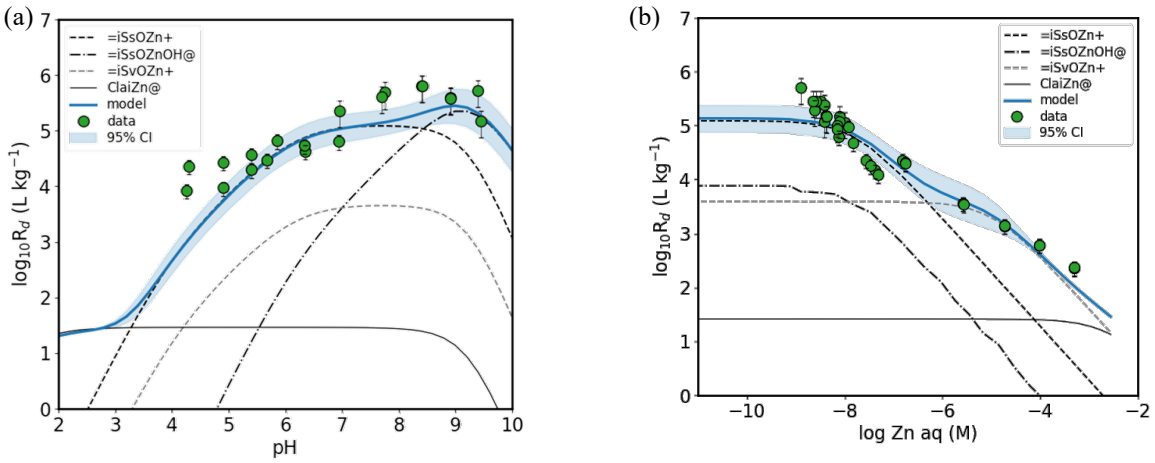

Fig. 4-9: Zn(II) sorption on Na-illite in 0.1 M $NaClO_4$

(a) pH edge and (b) sorption isotherm at pH 7.2, experimental data (Montoya et al. 2018)

4.1.8 Americium

Am(III) sorption data used for modelling sorption on illite were taken from Bradbury & Baeyens (2009b). The summary of published experimental datasets used for the modelling is given in App. E, Tab. E-1.

The same model for Am(III) sorption on illite as previously suggested by Bradbury & Baeyens (2017) was accepted in this work. Due to a high correlation between the values of surface complexation constants that describe sorption in the pH interval range of 7-9, the constant of the =iSsOAmOH+ surface complex has a wide confidence interval. This resulted in a very wide confidence interval of the calculated R_d values at near-neutral pH (Fig. 4-10a). Simplification of the model by eliminating this complex leads to a substantial reduction in the model uncertainty (Fig. 4-10b).

Spectroscopic studies of Cm(III)/Eu(III) sorption suggest three surface complexes on illite and montmorillonite on the one hand (Rabung et al. 2005), as well as practically the same hydrolysis behaviour of Cm(III) and Am(III) on the other. This indicates the necessity to include =iSsOAmOH+ into the Am(III) sorption model. Therefore, two alternative sets of surface complexation constants are given in this work (Tab. A-1).

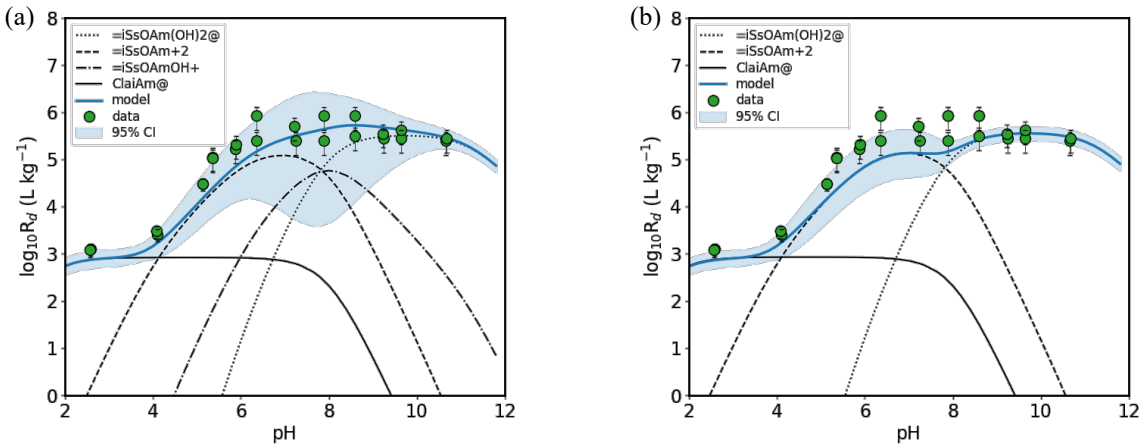

Fig. 4-10: pH edge of Am(III) on Na-illite in 0.1 M $NaClO_4$

(a) modelled with three surface complexes and (b) modelled with two surface complexes, experimental data (Bradbury & Baeyens 2009b)

4.1.9 Curium

Cm(III) sorption data used for modelling sorption on illite were taken from Rabung et al. (2005).

Only two surface complexation reactions for Cm(III) sorption on illite are proposed in this work in contrast to the previous model using three reactions (Bradbury & Baeyens 2017). This simplification is due to the fact that the available experimental data (Fig. 4-11, Rabung et al. 2005) are limited to a narrow pH range, which prevents the estimation of constants for surface complexation reactions that may occur at lower or higher pH values.

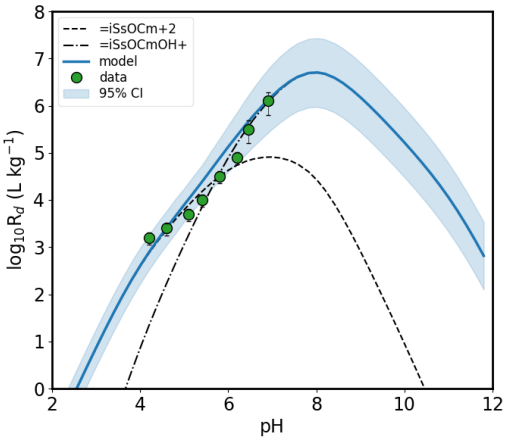

Fig. 4-11: Sorption edge of Cm(III) on Na-illite in 0.1 M $NaClO_4$

Experimental data (Rabung et al. 2005)

4.1.10 Europium

Eu(III) sorption data used for modelling sorption on illite were taken from Poinssot et al. (1999), Bradbury & Baeyens (2005a), Bradbury & Baeyens (2009a) and Marques Fernandes & Baeyens (2020). Additionally, unpublished in-house datasets of pH edges were included in the fitting (Fig. 4-12a and App. C, Section C.6). The experimental conditions and the results of the batch sorption experiments used for the modelling are given in App. C and App. D, Tab. D-1. The summary of published experimental datasets used in this work are given in App. E, Tab. E-1.

The proposed model of Eu(III) sorption on illite was simplified compared to the earlier one (Bradbury & Baeyens 2017) by eliminating two surface complexation reactions – one on strong sites and one on weak sites (Fig. 4-12). The reason for this simplification is to avoid the large uncertainty caused by multiple surface complexes supposed to occur over a narrow pH range and thus correlating with each other. Since two complexes, $\equiv iSsOEu(OH)_2^0$ and $\equiv iSvOEuOH^+$, had confidence intervals significantly larger than others during fitting trials, around 1 $\log_{10}K$ versus less than 0.3 $\log_{10}K$, they were eliminated from the model. Sufficient complexes remained to fit the available measured data. An attempt to eliminate the surface complex $\equiv iSsOEu(OH)_3^-$ instead of $\equiv iSsOEu(OH)_2^0$ led to an incomplete description of the measured data at pH values around 9, which was still within the pH interval relevant to the conditions of a deep geological repository.

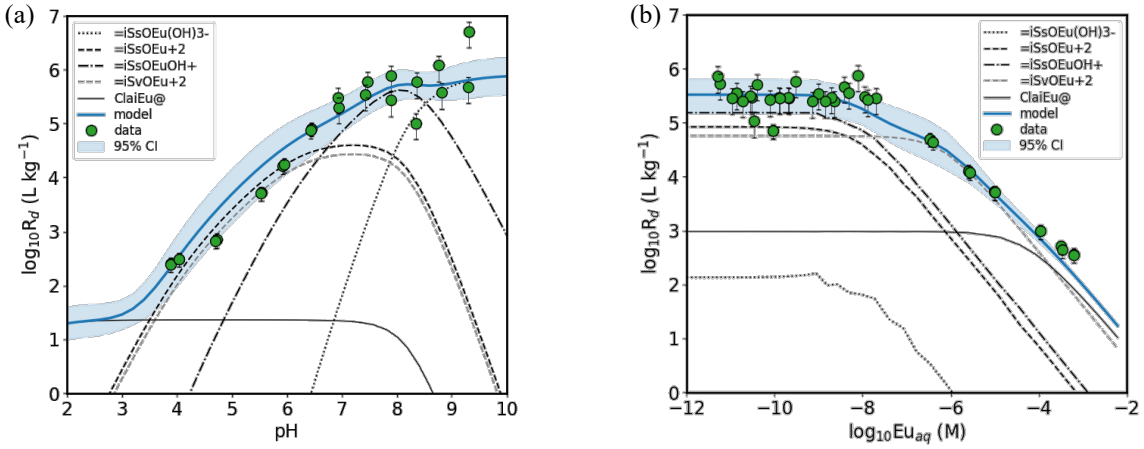

Fig. 4-12: Eu(III) sorption on Na-illite

(a) pH edge in 0.3 M $NaClO_4$, in-house experimental data, this work (the experimental conditions of sorption measurements are described in App. C and App. D, Tab. D-1), and (b) sorption isotherm at pH 7 in 0.1 M $NaClO_4$, experimental data (Poinssot et al. 1999)

4.1.11 Tin

Sn(IV) sorption data used for modelling sorption on illite were taken from Bradbury & Baeyens (2009a).

By applying the different set of hydrolysis reactions and constant values according to the TDB 2020, the Sn(IV) sorption model containing three surface complexes was sufficient to fit the data instead of the previously proposed model in Bradbury & Baeyens (2017) with four surface complexes. The surface complex $=iSsOSn(OH)_2^+$ was no longer needed in the current model to describe the measured data (Fig. 4-13).

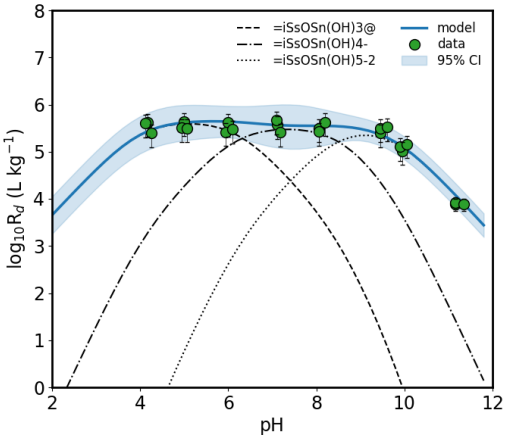

Fig. 4-13: pH edge of Sn(IV) on Na-illite in 0.1 M $NaClO_4$

Experimental data (Bradbury and Baeyens, 2009a)

4.1.12 Thorium

Th(IV) sorption data used for modelling sorption on illite were taken from Bradbury & Baeyens (2009b).

Similarly to the previously applied Th(IV) hydrolysis reactions set by Neck & Kim (2001), the $Th(OH)_3^+$ aqueous complex was removed from the set of aqueous species in the TDB 2020, and the sorption model had to be adjusted accordingly.

The surface complex $=iSsOTh(OH)_2^+$ was removed in accordance with the approach used for the linear free energy relationships between surface complexes and corresponding hydrolysed aqueous species (Bradbury & Baeyens 2005b). The proposed model with four surface complexes fits experimental data but shows relatively high uncertainty for three out of four surface complexation constants (Fig. 4-14). This is due to the insufficient number of measurements to distinguish the contribution of individual surface complexes from the overall sorption, resulting in a high correlation between the parameters.

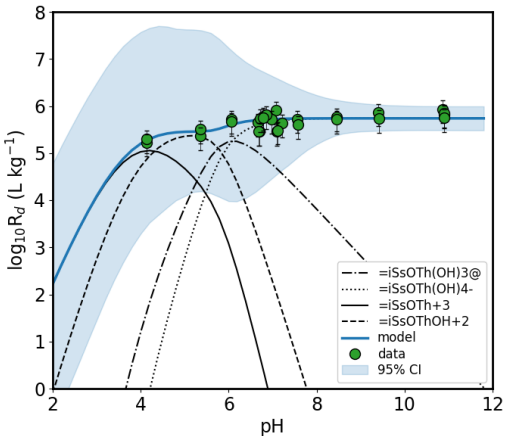

Fig. 4-14: Th(IV) sorption on Na-illite in 0.1 M $NaClO_4$

Experimental data (Bradbury & Baeyens 2009b)

4.1.13 Niobium

Nb(V) sorption data used for modelling sorption on illite were taken from Ervanne et al. (2014).

Nb(V) sorption on illite was modelled based on a single dataset of measurements carried out at trace concentrations presented in Fig. 4-15 (Ervanne et al. 2014). Although the authors suggested surface complexation reactions for both strong and weak sites, we adhere to the concept of the 2SPNE SC/CE model, in which sorption occurs predominantly on strong sites at trace concentrations.

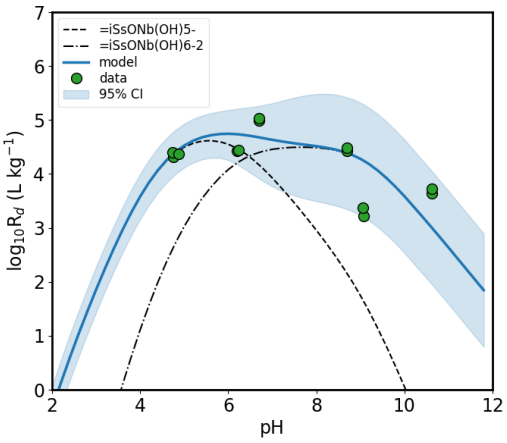

Fig. 4-15: Nb(V) sorption edge on Na-illite in 0.1 M $NaClO_4$

Experimental data (Ervanne et al. 2014)

4.1.14 Neptunium

Np(V) sorption data used for modelling sorption on illite were taken from Gorgeon (1994). Additionally, unpublished in-house datasets of a pH edge and an isotherm were included into the fitting (Fig. 4-16 and App. C, Section C.7). The experimental conditions and the results of the batch sorption experiments used for the modelling are given in App. C and App. D, Tab. D-1. The summary of published experimental datasets used in this work are given in App. E, Tab. E-1.

The current Np(V) sorption model on illite includes cation exchange and two surface complexation reactions as in Bradbury & Baeyens (2017), since the Np(V) hydrolysis speciation in the TDB 2020 remains the same as that used in the previous model (Fig. 4-16). However, the surface complexation constants were adjusted against the additional pH edge data that were included in the fitting for this study.

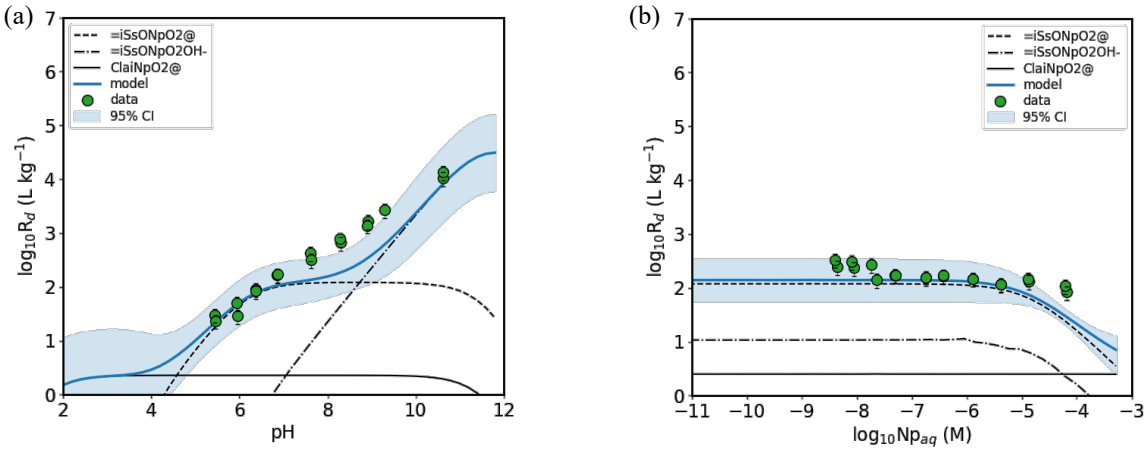

Fig. 4-16: Np(V) sorption on Na-illite in 0.1 M NaCl

(a) pH edge and (b) sorption isotherm at pH 7.7, in-house experimental data, this work (the experimental conditions of sorption measurements are described in App. C and App. D, Tab. D-1)

4.1.15 Protactinium

Pa(V) sorption data used for modelling sorption on illite were taken from Bradbury & Baeyens (2009b). The summary of published experimental datasets used for the modelling is given in App. E, Tab. E-1.

The aqueous hydrolysis speciation data for Pa(V) in the TDB 2020 differs significantly from that of Trubert et al. (2003), which was applied in the earlier Pa(V) sorption model development (Bradbury & Baeyens 2017). The current sorption model stays in compliance with the Pa(V) aqueous speciation in the TDB 2020, but, to this end, the surface complex $\equiv SsOPaO_2^0$ was removed from the model, and the surface complex $\equiv SsOPaO_2(OH)_2^{2-}$ was inserted instead.

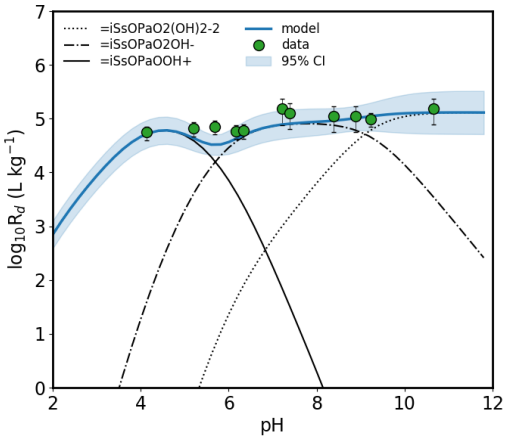

Fig. 4-17: Pa(V) sorption edge on Na-illite in 0.1 M $NaClO_4$

Experimental data (Bradbury & Baeyens 2009b)

4.1.16 Uranium

U(VI) sorption data used for modelling sorption on illite were taken from Bradbury & Baeyens (2005a) and Bradbury & Baeyens (2009b). Additionally, unpublished in-house datasets of pH edges and isotherms were included into the fitting (Fig. 4-18 and App. C, Section C.8). The experimental conditions and the results of the batch sorption experiments used for the modelling are given in App. C and App. D, Tab. D-1. The summary of published experimental datasets used in this work are given in App. E, Tab. E-1.

The aqueous hydrolysis speciation of U(VI) in the TDB 2020 is similar to that used previously in Bradbury & Baeyens (2017). According to the observations in Bradbury & Baeyens (2017), the model predicts that the surface complexes on weak sites make a similar contribution to the total sorption as the ones on the strong sites at trace U(VI) concentrations (e.g., the curve of $\equiv$iSsOUO$_2$OH@ almost overlaps with $\equiv$iSvOUO$_2$OH@, and similar overlapping of $\equiv$iSsOUO$_2$(OH)$_2^-$ and $\equiv$iSvOUO$_2$(OH)$_2^-$ is observed). During the model parameterisation, it became apparent that the value of the selectivity coefficient ${}^{UO_2}_{Na}K_c$ cannot be unequivocally retrieved as it only affects the U(VI) speciation at pH <3, where difficulties due to clay dissolution affect the measurements. Thus, it was decided to retain the previously estimated value for the selectivity coefficient without calculated uncertainty. This does not have any effect on the model in the near-neutral pH range (Fig. 4-18), but it helps to parameterise the model by reducing the number of simultaneously fitted parameters. It should be noted that spectroscopic investigations of uranyl sorption on montmorillonite at low pH and low ionic strength, show that cation exchange plays an important role (Dent et al. 1992). This should also be the case for illite, since both clays have a similar 2:1 structure.

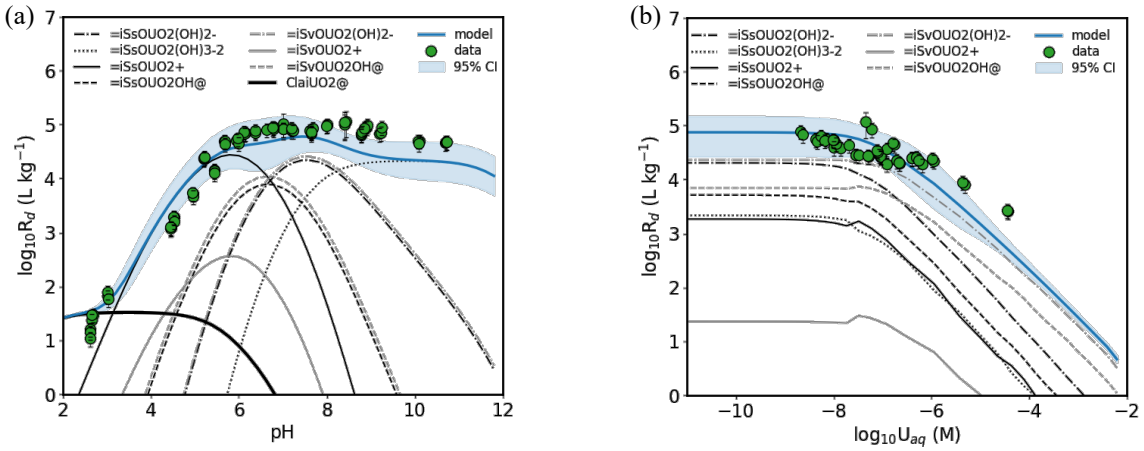

Fig. 4-18: U(VI) sorption on Na-illite in 0.1 M $NaClO_4$

(a) pH edge, experimental data (Bradbury & Baeyens 2009b) and (b) sorption isotherm at pH 7.2, in-house experimental data, this work (the experimental conditions of sorption measurements are described in App. C and App. D, Tab. D-1)

4.2 Modelling sorption edges and isotherms on montmorillonite

4.2.1 Caesium

The source Cs(I) sorption isotherm (Fig. 4-20b) used for modelling sorption on montmorillonite was taken from Bradbury & Baeyens (2002a). The pH edges represented in this work (Fig. 4-19a and App. C, Section C.1) are in-house unpublished datasets. The experimental conditions and the results of the batch sorption experiments used for the modelling are given in App. C and App. D, Tab. D-1.

The Cs(I) sorption model on montmorillonite is based on the assumption that the uptake of Cs(I) by smectites predominantly occurs via cation exchange and is analogous to a simple cation exchange model applied in Bradbury & Baeyens (2002a). It contains only one $Na^+ - Cs^+$ cation exchange reaction on the planar sites (Fig. 4-19, Tab. A-6).

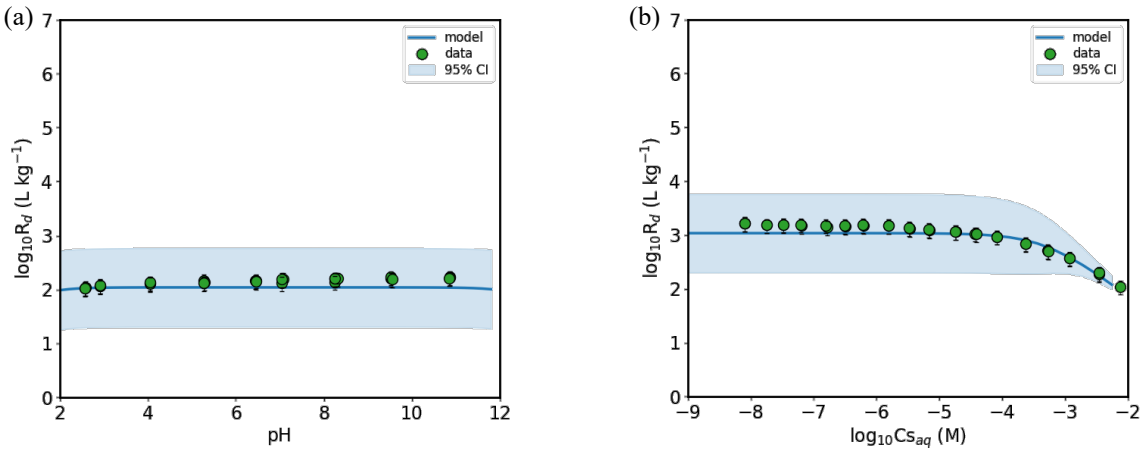

Fig. 4-19: Cs(I) sorption on Na-montmorillonite

(a) pH edge in 0.1 M $NaClO_4$, experimental in-house data, this work (the experimental conditions of sorption measurements are described in App. C and App. D, Tab. D-1), and (b) sorption isotherm at pH 6 in 0.01 M $NaClO_4$ (Bradbury & Baeyens 2002a)

4.2.2 Cadmium

Cd(II) sorption data used for modelling sorption on montmorillonite were taken from Zachara et al. (1993), Itami & Yanai (2006), and Missana et al. (2023). The summary of published experimental datasets used for the modelling is given in App. E, Tab. E-1.

Compared to a previous parameterisation (Bradbury & Baeyens 2017), which included a cation exchange on planar sites and a surface complexation reaction on strong edge sites, the current model additionally includes a surface complexation reaction on weak edge sites (Fig. 4-20) due to the involvement of isotherm data in the modelling.

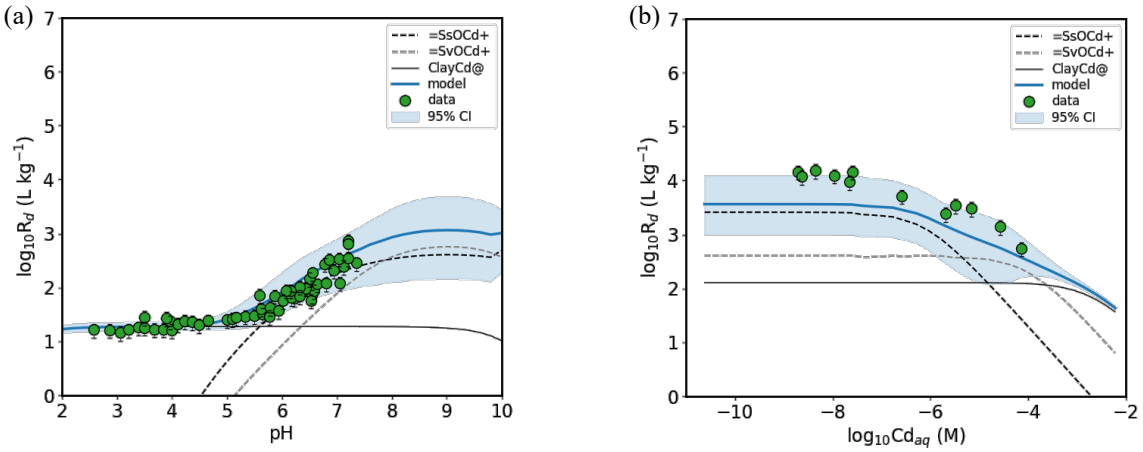

Fig. 4-20: Cd(II) sorption on Na-montmorillonite

(a) pH edge in 0.25 M $NaNO_3$, experimental data (Itami & Yanai 2006) and (b) sorption isotherm at pH 7.8 in 0.1 M $NaClO_4$, experimental data (Missana et al. 2023)

4.2.3 Cobalt

Co(II) sorption data used for modelling sorption on montmorillonite were taken from Baeyens & Bradbury 2017. Additionally, an unpublished in-house dataset of an isotherm was included into the fitting (Fig. 4-21b). The conditions of this experiment are outlined in App. C and App. D, Tab. D-1. The summary of published experimental datasets used in this work are given in App. E, Tab. E-1.

The aqueous thermodynamic data used for the Co(II) modelling on montmorillonite were taken from the ThermoChimie database, version 11a (Giffaut et al. 2014).

The value of the cation exchange selectivity coefficient for Co^{2+} −Na^{+} exchange was taken as equal to that for Ni^{2+} −Na^{+} exchange. This assumption was made as it was not possible to estimate it independently of surface complexation constants on weak sites based on available datasets. Simultaneous fitting of available Co(II) sorption edge and isotherm datasets led to the complete suppression of the surface complex on weak sites =SvOCo^{+} in favour of the cation exchange complex. This erroneous underestimation can be clearly detected during the fitting by taking only isotherm data into account. In this case, the surface complex =SvOCo^{+} becomes significant. In order to avoid the underestimation of =SvOCo^{+} and its removal from the model, it was decided to fix the selectivity coefficient value by assigning it with the corresponding value of the chemical analogue Ni(II). Examples of a pH edge and an isotherm of Co(II) on montmorillonite are shown in Fig. 4-21.

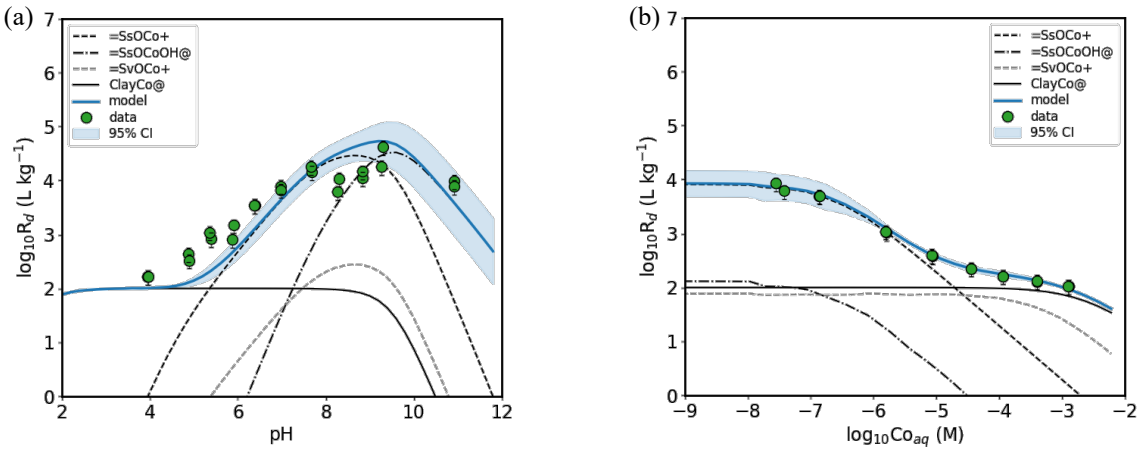

Fig. 4-21: Co(II) sorption on Na-montmorillonite

(a) pH edge, experimental data (Baeyens & Bradbury 2017) and (b) sorption isotherm at pH 7.3 in 0.1 M NaCl, in-house experimental data, this work (the experimental conditions of sorption measurements are described in App. C and App. D, Tab. D-1)

4.2.4 Iron

Fe(II) sorption data used for modelling sorption on montmorillonite were taken from Soltermann et al. (2013) and Soltermann et al. (2014). The summary of published experimental datasets used for the modelling is given in App. E, Tab. E-1.

For Fe(II) sorption modelling on Na-montmorillonite, the same sorption model as proposed in Bradbury & Baeyens (2017) was applied. Unlike the model proposed in Soltermann et al. (2014), the model suggested here does not contain additional surface complexation reactions for Fe(II) that involve surface oxidation of ferrous iron surface complexes ($=S_{s,w}OFe^{+}$) to ferric iron surface complexes ($=S_{s,w}OFe^{2+}$) on both strong and weak sites. The set consisted of cation exchange on the planar sites, and one surface complexation reaction on both strong and weak sites was enough to describe the available experimental data (Fig. 4-22).

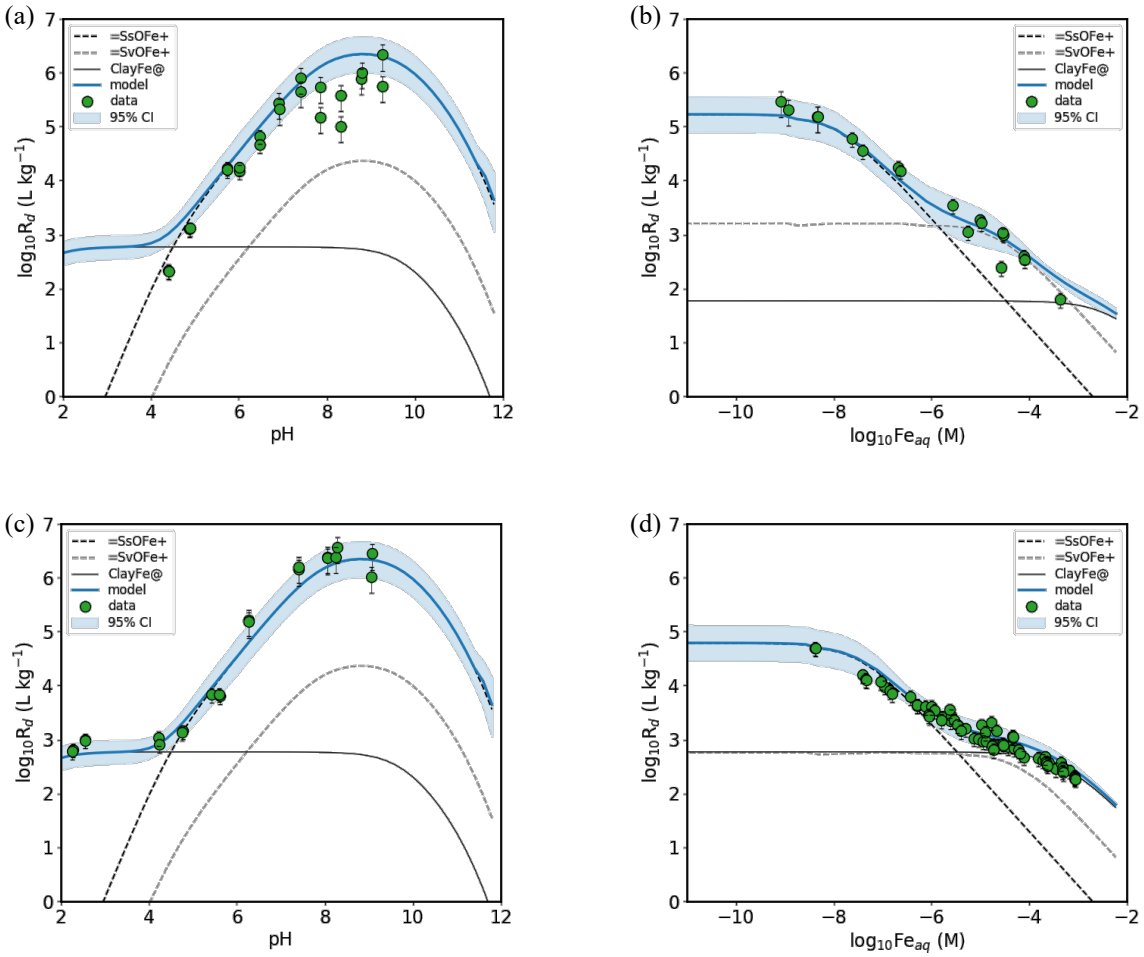

Fig. 4-22: Fe(II) sorption on Na-montmorillonite in 0.1 M $NaClO_4$

(a) pH edge and (b) isotherm at pH 6.7 on synthetic Na-montmorillonite in 0.1 M $NaClO_4$, experimental data (Soltermann et al. 2013), (c) pH edge and (d) isotherm at pH 6.2 on Na-STx, experimental data (Soltermann et al. 2014)

4.2.5 Manganese

Unpublished in-house data were used to model the sorption of Mn(II) on montmorillonite (Fig. 4-23 and App. C, Section C.2). The experimental conditions and the results of the batch sorption experiments used for the modelling are given in App. C and App. D, Tab. D-1.

The sorption model for Mn(II) was constructed with the same type of surface complexes as that for Fe(II). The model shows a good fit to measured data except for a few points with strong sorption at high pH values, probably caused by adsorbed Mn(II) oxidation (Fig. 4-23).

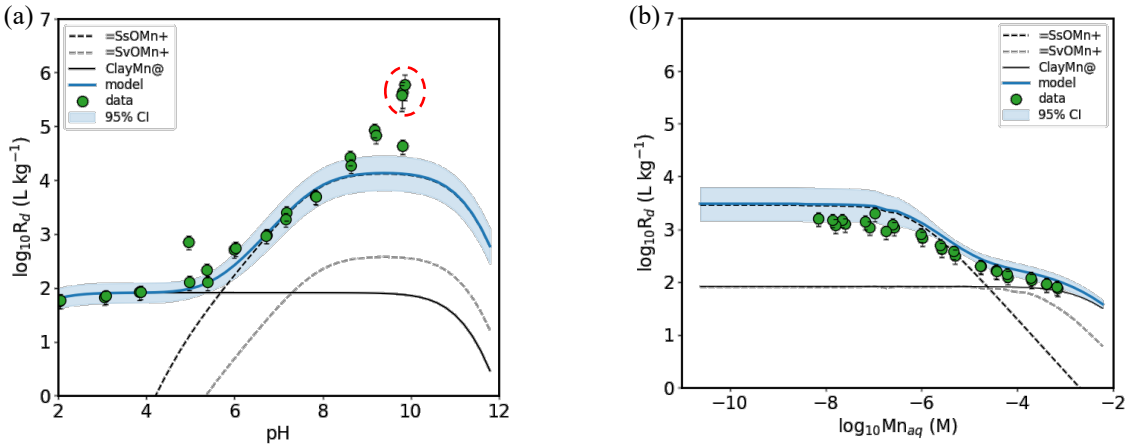

Fig. 4-23: Mn(II) sorption on Na-montmorillonite in 0.1 M NaCl

(a) pH edge and (b) sorption isotherm at pH 7.3, in-house experimental data, this work (the experimental conditions of sorption measurements are described in App. C and App. D, Tab. D-1). The circled points in plot (a) may correspond to surface precipitation of Mn(III) (hydr)oxide

4.2.6 Nickel

Ni(II) sorption data used for modelling sorption on montmorillonite were taken from Baeyens & Bradbury (1997) and Marques Fernandes & Baeyens (2020). Additionally, unpublished in-house sorption isotherm datasets were included into the fitting (App. C, Section C.3). The experimental conditions and the results of the batch sorption experiments used for the modelling are given in App. C and App. D, Tab. D-1. The summary of published experimental datasets used in this work are given in App. E, Tab. E-1.

In contrast to the previous model in Baeyens & Bradbury (2017), only two surface complexation reactions on strong sites were included into the present model of Ni(II) sorption on montmorillonite (Fig. 4-24). This simplification is reasonable when considering the experimental points at pH values below 10 in order to reduce the interference of Ni(II) sorption on aluminium hydroxides, which may form as a result of clay dissolution under alkaline conditions. The proposed model fits experimental points with relatively low uncertainty values and is consistent with the models for other bivalent elements with similar hydrolysis behaviour, and with the Ni(II) sorption model on illite.

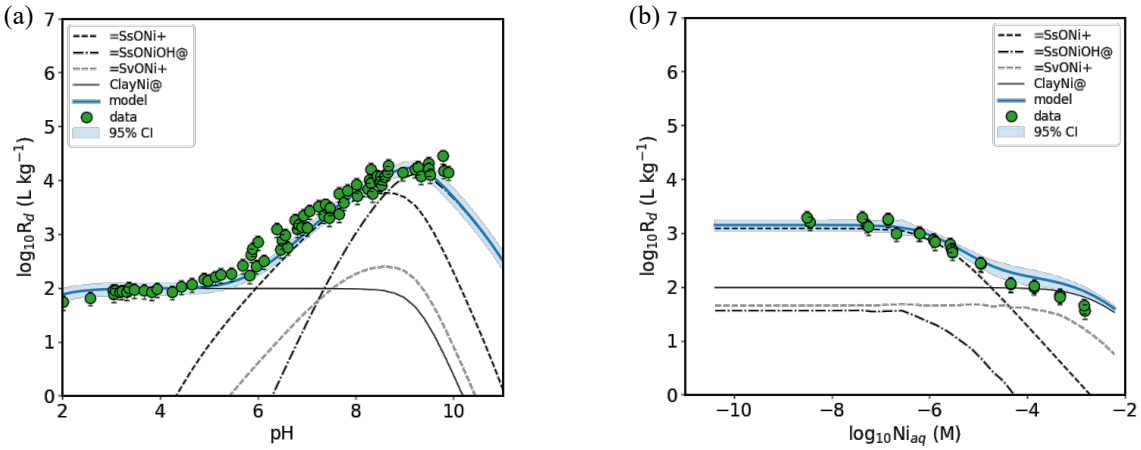

Fig. 4-24: Ni(II) sorption on Na-montmorillonite in 0.1 M $NaClO_4$

(a) pH edge, experimental data (Baeyens & Bradbury 1997) and (b) sorption isotherm at pH 7.1, experimental data (Marques Fernandes & Baeyens 2020)

4.2.7 Lead

Pb(II) sorption data used for modelling sorption on montmorillonite were taken from Marques Fernandes & Baeyens (2019). Additionally, an unpublished in-house dataset of the sorption isotherm was included into the fitting (App. C, Section C.4). The experimental conditions and the results of the batch sorption experiments used for the modelling are given in App. C and App. D, Tab. D-1. The summary of published experimental datasets used in this work are given in App. E, Tab. E-1.

Pb(II) shows relatively high sorption in the acidic region in comparison to other bivalent elements with similar hydrolysis behaviour (Fig. 4-25). This was explained by a specific sorption of Pb(II) on so-called "high-affinity" sites that were included into the model proposed in Marques Fernandes & Baeyens (2019). For the current model, "high-affinity" sites were not considered. Therefore, the value of the Pb(II) selectivity coefficient is higher than for other bivalent metals with similar hydrolysis behaviour due to partial compensation by ion exchange at low pH.

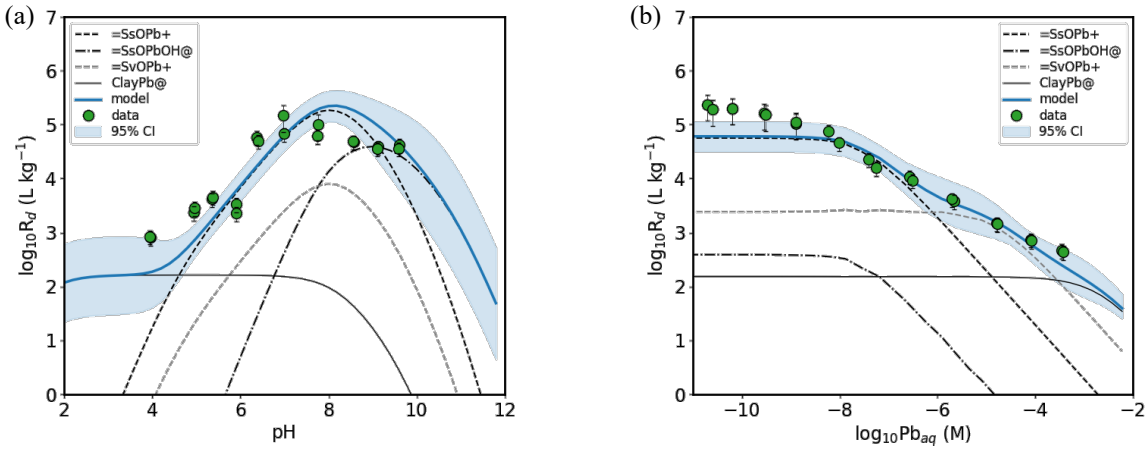

Fig. 4-25: Pb(II) sorption on Na-montmorillonite in 0.1 M $NaClO_4$

(a) pH edge and (b) sorption isotherm at pH 7, experimental data (Marques Fernandes & Baeyens 2019)

4.2.8 Radium

Ra(II) sorption data used for modelling sorption on montmorillonite were taken from Klinkenberg et al. (2021).

The same Ra(II) sorption model on montmorillonite as proposed in Klinkenberg et al. (2021) was applied in this study. Similar to illite, a good agreement of the model could not be obtained against the data measured in solutions of varying ionic strengths. Only one dataset with the highest ionic strengths (0.3 M) closest to those in bentonite porewater was used for the model parameterisation (Fig. 4-26). The proposed model overestimates the experimental data at lower ionic strength (0.02 M and 0.14 M NaCl, not shown). These were not used in the fitting.

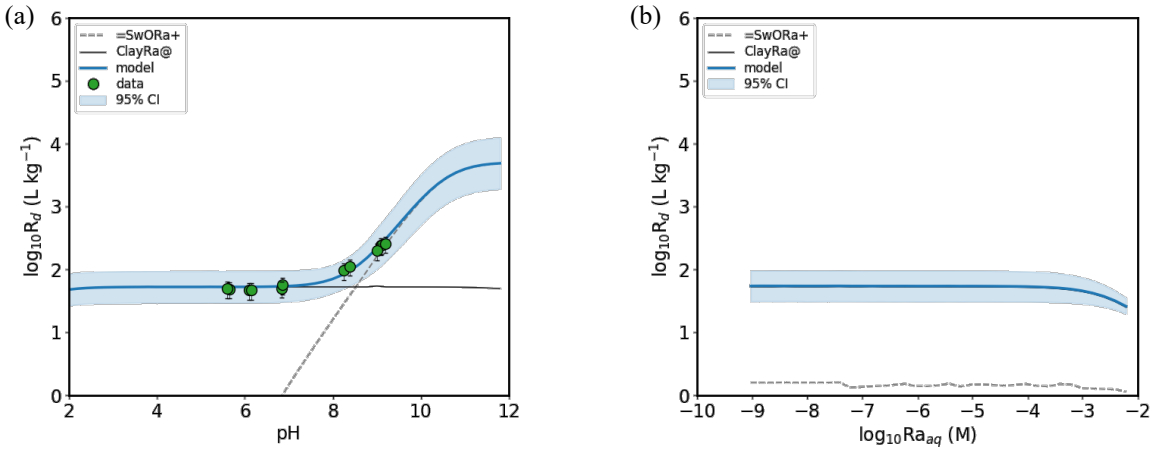

Fig. 4-26: Ra(II) sorption on Na- montmorillonite in 0.3 M NaCl

(a) pH edge, experimental data (Klinkenberg et al. 2021) and (b) predicted sorption isotherm at pH 7 (no Ra sorption isotherm data on montmorillonite available)

4.2.9 Zinc

Zn(II) sorption data used for modelling sorption on montmorillonite were taken from Baeyens & Bradbury (1997), Dähn et al. (2011) and Marques Fernandes & Baeyens (2020). Additionally, unpublished in-house datasets of the pH edge and sorption isotherm were included into the fitting (App. C, Section C.5). The experimental conditions and the results of the batch sorption experiments used for the modelling are given in App. C and App. D, Tab. D-1. The summary of published experimental datasets used in this work are given in App. E, Tab. E-1.

The surface complexation component of the model of Zn(II) sorption on montmorillonite was reduced to one reaction on strong- and one reaction on weak sites, compared to the earlier model in Baeyens & Bradbury (2017), which included three surface complexation reactions on strong sites and one on weak sites. By contrast, the model of Zn(II) sorption on illite contains two surface complexation reactions due to the availability of sorption isotherm data at pH 8.4, while the highest pH for which the montmorillonite isotherm was obtained is 7.7. Nevertheless, the simplified Zn(II) sorption model is sufficient to fit the available experimental data (Fig. 4-27).

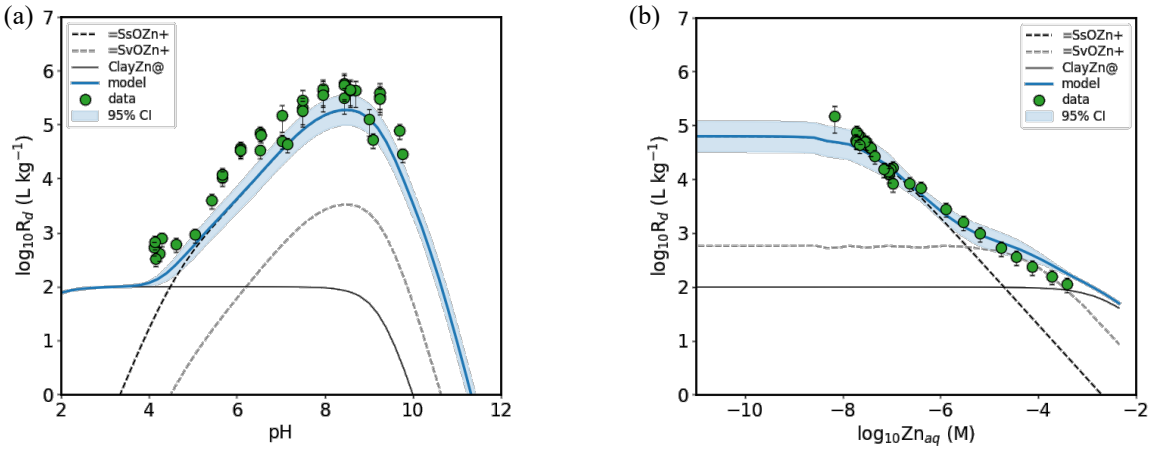

Fig. 4-27: Zn(II) sorption on Na-montmorillonite

(a) pH edge in 0.1 M $NaClO_4$ and (b) sorption isotherm at pH 7 in 0.1 M $NaClO_4$, experimental data (Baeyens & Bradbury 1997)

4.2.10 Americium

Data concerning Am(III) sorption on montmorillonite were taken from Bradbury & Baeyens (2005b) and Bradbury & Baeyens (2006). The summary of published experimental datasets used for the modelling is given in App. E, Tab. E-1.

The model of Am(III) sorption on montmorillonite includes a cation exchange reaction and two surface complexation reactions. This is different from the model in Baeyens & Bradbury (2017) that additionally contains the $=SsOAmOH^+$ surface complex. The reason for its removal from the current model was its low sensitivity and strong correlation with the other surface complexes. The same issue was observed for illite. However, in that case, a value for the surface complexation constant could be fitted, and a wide 95% confidence interval could be estimated. The exclusion of this surface complex does not significantly affect the modelled R_d values but helps to better constrain the model fit and to reduce the uncertainty (Fig. 4-28).

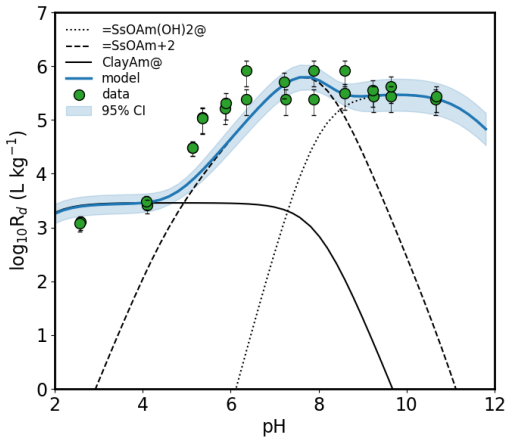

Fig. 4-28: Sorption edge of Am(III) on Na-montmorillonite in 0.1 M $NaClO_4$
Experimental data (Bradbury & Baeyens 2006)

4.2.11 Europium

Data concerning Eu(III) sorption data on montmorillonite were taken from Bradbury & Baeyens (2002c), Bradbury & Baeyens (2006) and Marques Fernandes & Baeyens (2020). Additionally, unpublished in-house datasets of the pH edge and sorption isotherm were included into the fitting (App. C, Section C.6). The experimental conditions and the results of the batch sorption experiments used for the modelling are given in App. C and App. D, Tab. D-1. The summary of published experimental datasets used in this work are given in App. E, Tab. E-1.

The current Eu(III) sorption model on montmorillonite was changed compared to that in Bradbury & Baeyens (2017) by adding the surface complex $=SsOEu(OH)_3^-$ instead of $=SsOEu(OH)_2^0$. This was done in consistency with the Eu(III) sorption model on illite. The model with four surface complexes led to high uncertainties for the calculated R_d values caused by the correlation of surface complexes that partially overlap in a narrow pH range. Retaining the $=SsOEu(OH)_2^0$ complex in the model instead of $=SsOEu(OH)_3^-$ led to an incomplete description of the data at pH values around 9. The model with the currently selected complexes can fit the available measured data with a narrow 95% confidence interval of the calculated R_d (Fig. 4-29).

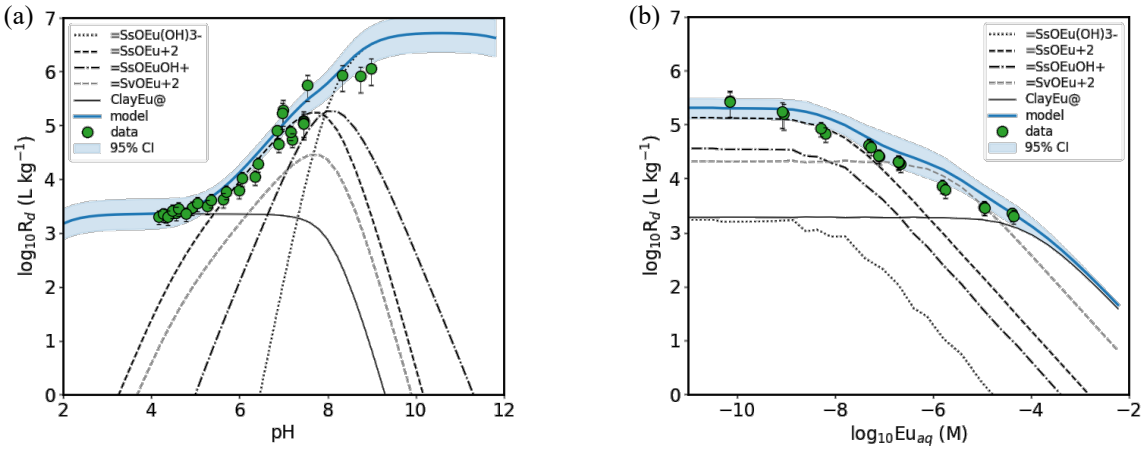

Fig. 4-29: Eu(III) sorption on Na-montmorillonite in 0.1 M $NaClO_4$

(a) pH edge, experimental data (Bradbury & Baeyens 2006) and (b) sorption isotherm at pH 7.2, experimental data (Marques Fernandes & Baeyens 2020)

4.2.12 Tin

Data concerning Sn(IV) sorption on montmorillonite were taken from Bradbury & Baeyens (2005b) and Ishidera et al. (2023). The summary of published experimental datasets used for the modelling is given in App. E, Tab. E-1.

Due to the significantly different Sn(IV) aqueous speciation used in Baeyens & Bradbury (2017) compared to that used in the TDB 2020, the sorption model had to be modified accordingly. The surface complex $=SsOSn(OH)_2^+$ was excluded due to the low sensitivity of the model to representing the available measured data. The main improvement to the model of Sn(IV) sorption on montmorillonite was the addition of two surface complexation reactions on weak sites to the model. This resulted from the availability of pH edge datasets with relatively high Sn(IV) loadings, which were assumed to saturate the strong sites. Since similar data are unavailable for illite, the corresponding model improvement was not possible. Another difference from the illite sorption model is the removal of the surface complex $=SsOSn(OH)_4^-$, which showed high uncertainty and was correlated with other surface complexes. The remaining set of surface complexation reactions was sufficient to fit the measured pH edge data (Fig. 4-30).

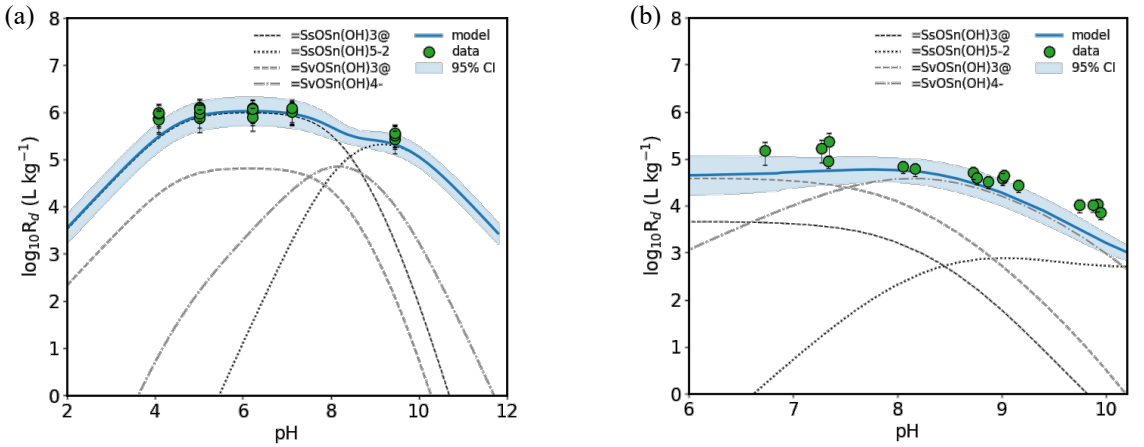

Fig. 4-30: Sn(IV) sorption on Na-montmorillonite in 0.1 M $NaClO_4$

(a) pH edge, experimental data (Bradbury & Baeyens 2005b) and (b) pH edge, experimental data (Ishidera et al. 2023)

4.2.13 Thorium

Data concerning Th(IV) sorption on montmorillonite were taken from Bradbury & Baeyens (2005b). Additionally, an unpublished in-house dataset of the pH edge was included into the fitting (Fig. 4-31). The experimental conditions and the results of the batch sorption experiments used for the modelling are given in App. C and App. D, Tab. D-1.

Similar to that for illite (Section 4.1.12), the Th(IV) sorption model for montmorillonite was adjusted to account for the removal of aqueous $Th(OH)_3^+$ species from the TDB 2020 by removing the surface complex $=SsOTh(OH)_2^+$. The measured data were fitted successfully with the proposed model with four surface complexes, and show lower uncertainty than the Th(IV) sorption model on illite due to the larger number of measurements available for montmorillonite, thereby better constraining the model (Fig. 4-31).

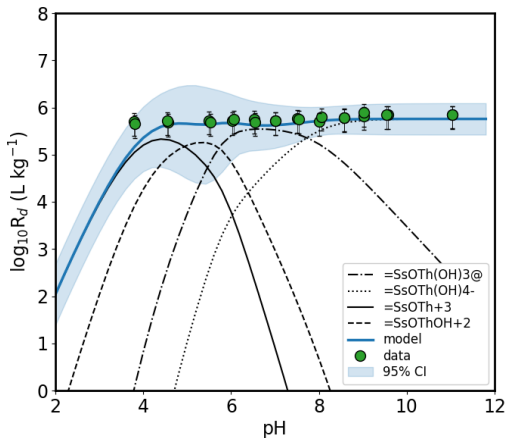

Fig. 4-31: pH edge of Th(IV) sorption on Na-montmorillonite in 0.1 M $NaClO_4$

In-house experimental data (the experimental conditions of sorption measurements are described in App. C and App. D, Tab. D-1)

4.2.14 Niobium

Data concerning Nb(V) sorption on montmorillonite were taken from Ishidera et al. (2023). Additionally, the dataset of the pH edge for illite taken from Ervanne et al. (2014) was included into the fitting (see justification below). The summary of published experimental datasets used for modelling is given in App. E, Tab. E-1.

The experimental data for Nb(V) sorption on montmorillonite (Ishidera et al. 2023) were represented as two pH edges with relatively high Nb(V) loadings implying the (near-)saturation of the strong sites. With only these measured data, it was not possible to estimate the constants of surface complexation reactions on strong sites. In order to fill this data gap, it was decided to use the Nb(V) pH edge dataset on illite, assuming the same R_d values of Nb(V) on illite and montmorillonite. Simultaneous fitting of a proxy model, similar to that applied to illite, to the three experimental datasets made it possible to estimate the constants of surface complexation reactions on strong sites. However, the surface complex $=SsONb(OH)_6^{2-}$ demonstrated the uncertainty of more than one $\log_{10}K$ unit. By removing this complex, it was possible to fit the measured data and to reduce the uncertainties of model parameters (Fig. 4-32). Consequently, the resulting Nb(V) sorption model on montmorillonite is somewhat different from the model for illite.

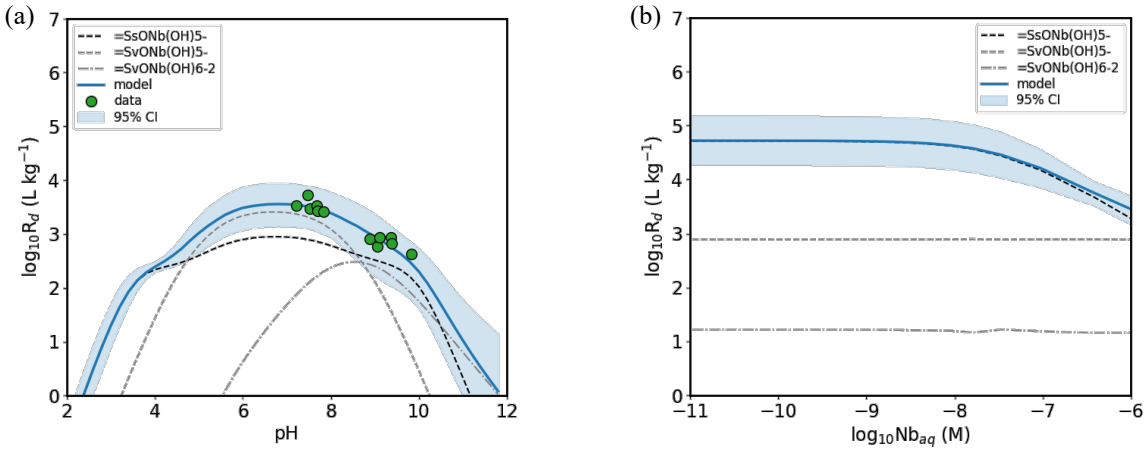

Fig. 4-32: Nb(V) sorption on Na-montmorillonite

(a) pH edge, experimental data (Ishidera et al. 2023) and (b) predicted sorption isotherm at pH 7 in 0.1 M NaCl (no isotherm data were available for Nb on montmorillonite)

4.2.15 Neptunium

Data concerning Np(V) sorption on montmorillonite were taken from Gorgeon (1994) and Bradbury & Baeyens (2005b). Additionally, unpublished in-house datasets of pH edges and isotherms were included into the fitting (App. C, Section C.7). The experimental conditions and the results of the batch sorption experiments used for the modelling are given in App. C and App. D, Tab. D-1. The summary of published experimental datasets used in this work are given in App. E, Tab. E-1.

This study follows the model defined in the previous investigation (Baeyens & Bradbury 2017). However, since a few more datasets were included into the fitting procedure, the values of surface complexation constants obtained here are slightly different compared to the previous study. Examples of a pH edge and an isotherm are shown in Fig. 4-33.

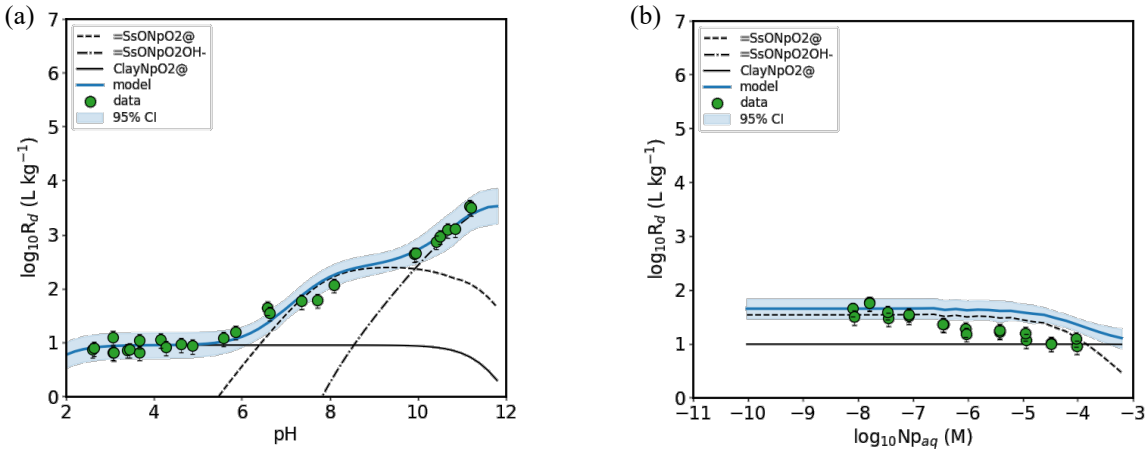

Fig. 4-33: Np(V) sorption on Na-montmorillonite

(a) pH edge, experimental data (Bradbury & Baeyens 2005b) and (b) sorption isotherm at pH 7 in 0.1 M NaClO4, in-house experimental data (the experimental conditions of sorption measurements are described in App. C and App. D, Tab. D-1)

4.2.16 Protactinium

Data concerning Pa(V) sorption on montmorillonite were taken from Bradbury & Baeyens (2006) and Baeyens & Marques Fernandes (2018). The summary of published experimental datasets used for the modelling is given in App. E, Tab. E-1.

The current Pa(V) sorption model contains one more surface complex than the previous model in Baeyens & Bradbury (2017). The surface complex $=SsOPaO_2(OH)_2^{2-}$ was added into the model in compliance with the changed Pa(V) aqueous speciation according to the TDB 2020. In contrast to the Pa(V) sorption model on illite, the surface complex $=SsOPaO_2^0$ was kept in the model (Fig. 4-34). This discrepancy can be explained by the differences in the protolysis constants of the two clay minerals, due to which the positions of surface complexation curves along the pH scale are shifted, resulting in varying levels of sensitivity to the measured data.

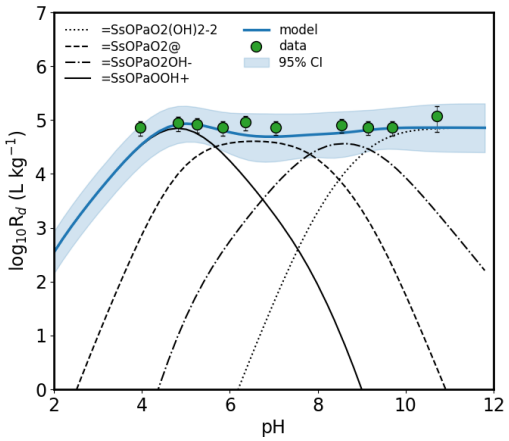

Fig. 4-34: pH edge of Pa(V) sorption on Na-montmorillonite in 0.1 M $NaClO_4$
Experimental data (Bradbury & Baeyens 2006)

4.2.17 Uranium

Data concerning U(VI) sorption on montmorillonite were taken from Bradbury & Baeyens (2005b) and Marques Fernandes et al. (2012). Additionally, unpublished in-house datasets of adsorption isotherms were included into the fitting (App. C, Section C.8). The experimental conditions and the results of the batch sorption experiments used for the modelling are given in App. C and App. D, Tab. D-1. The summary of published experimental datasets used in this work are given in App. E, Tab. E-1.

In contrast to the earlier model (Baeyens & Bradbury 2017), the current model does not involve the surface complex $=SsOUO_2(OH)_2^-$ due to its high uncertainty and low sensitivity to the measured data available (Fig. 4-35). Removing the $=SsOUO_2(OH)_3^{-2}$ complex instead of $=SsOUO_2(OH)_2^-$ resulted in a worse fit with the data at trace uranium concentration at pH 7 – 9. Although keeping $=SsOUO_2(OH)_3^{-2}$ in the model yielded a wide 95% confidence interval for the calculated R_d values at pH 8.5 and above, the most accurate match in the near-neutral region is of higher importance when taking natural porewater conditions into account.

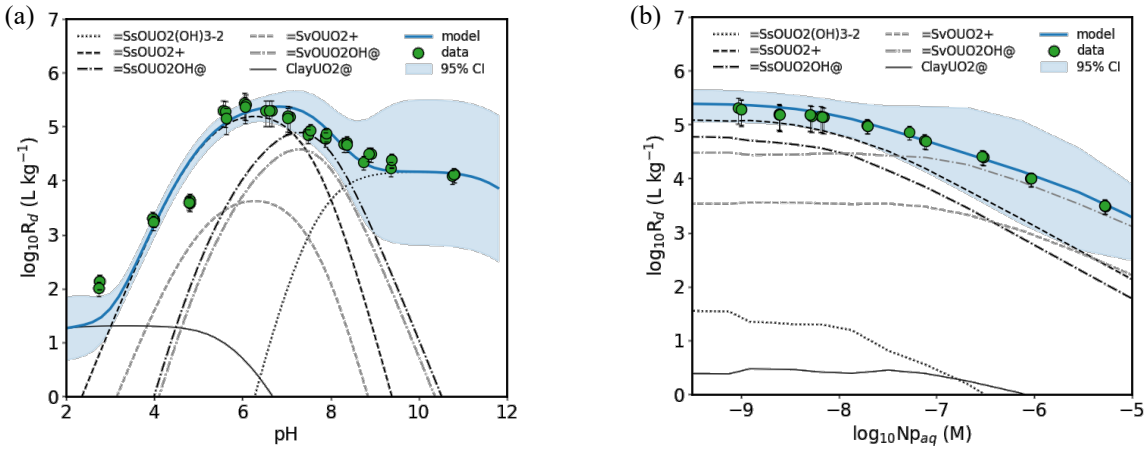

Fig. 4-35: U(VI) sorption on Na-montmorillonite (Na-SWy-1) in 0.1 M $NaClO_4$

(a) pH edge, experimental data (Marques Fernandes et al. 2012) and (b) sorption isotherm at pH 6.8, experimental data (Bradbury & Baeyens 2005b)

4.3 Predictions of Cd(II), Fe(II), Pu(III, IV), Np(IV), and U(IV) sorption on illite and montmorillonite based on linear free energy relationships

Well-established correlations between the free energies of formation of metal complexes and the standard thermodynamic properties of the metal ions or ligands form the basis of the approach to linear free energy relationships (LFER). To derive the surface complexation constants for both strong and weak site types when lacking experimental data for certain elements, it is possible to use the relationship between the stability constants of aqueous and surface complexes, i.e., the so-called LFER (Bradbury & Baeyens 2005b). This approach has been successfully validated by comparison with the experimental sorption data for many elements on illite (Bradbury & Baeyens 2017) and montmorillonite (Baeyens & Bradbury 2017). The R_d values calculated for a particular radionuclide based on its surface complexation equilibrium constants extracted from LFER might not necessarily reproduce the measured sorption data with a high degree of accuracy. However, given the averaging of many datasets, this approach has in most cases demonstrated its reliability to produce qualitatively correct predictions.

The general formula for the hydrolysed species of a metal Me with valency (Z_{Me}) can be written as:

$$\mathrm{Me(OH)_x^{Z_{Me}-x}}$$

and the general formula of the surface complex on the "strong" amphoteric surface hydroxyl group as:

$$\equiv \mathrm{S^SOMe(OH)_y^{Z_{Me}-(y+1)}}$$

Since the surface hydroxyl group is considered analogous to one hydroxyl ion in solution, x and y in those equations are related as:

$$x = y + 1$$

In this work, surface complexation constants for Cd(II) and Fe(II) on strong and weak sites on illite were obtained using the LFER approach based on the aqueous hydrolysis equilibrium constants from the TDB 2020 (Hummel & Thoenen 2023) and updated surface complexation constants of bivalent elements obtained in the present work. The choice of using LFER to obtain the Cd(II) constant is driven by the unavailability of relevant in-house experimental data and by the lack of consistent published data. The existing data on Fe(II) sorption on illite (Chen et al. 2022) cannot be used confidently for the determination of surface complexation constants due to possible oxidation of surface complexes and precipitation of iron-bearing phases.

Since reduced Np, Pu, and U species are expected under the conditions of in-situ Opalinus Clay porewaters, but corresponding experimental sorption data are lacking, the LFER approach was also applied to derive surface complexation constants for Pu(III, IV), Np(IV) and U(IV) on strong sites of illite and montmorillonite.

Although the attempt to find a common LFER equation for determining surface complexation constants for all valence elements was made in Bradbury & Baeyens (2005b), subsequent studies showed that the more appropriate approach is to limit the correlation to constants of the same valence metals (Bradbury & Baeyens 2017).

4.3.1 Cd(II) and Fe(II) on illite

In the previous work (Bradbury & Baeyens 2017), the surface complexation constants for bivalent transition metals Mn(II), Fe(II), Cu(II) were derived using an LFER based on first hydrolysis constants of Co(II), Ni(II), and Zn(II). The limitation of first hydrolysis constants usage was explained by the more significant errors of the hydrolysis constants of higher orders in comparison to the highest reliability of the first hydrolysis constant values because they can be determined at high metal concentrations using potentiometric methods. As new sorption data for Mn(II) and Pb(II) on illite have since been obtained and used for modelling in the current work, it was possible to include the corresponding constants in the LFER plot in addition to the metals listed above (Fig. 4-36). However, the plot containing only the first hydrolysis constants exhibited scatter with a low correlation coefficient of 0.7, and the subsequent inclusion of the second hydrolysis constants in the LFER plot increased the correlation coefficient to 0.98.

Regarding the application of the LFER approach to the derivation of surface complexation constants on weak sites, inclusion of different valence metals on the same LFER plot was suggested in Bradbury & Baeyens (2017). The reason for this was the assumption that there is no competitive sorption on weak sites due to their large sorption capacity. In the present work, Cd(II) and Fe(II) surface complexation constants on weak sites were obtained from the LFER approach based on the data of same-valence metals (App. A, Tab. A-2). This approach was applied because apart from bivalent metals, only four constants for weak sites were available – one for Eu^{3+} and three for UO_2^{2+} – and they seemed to be inconsistent with the plot formed by bivalent metal data.

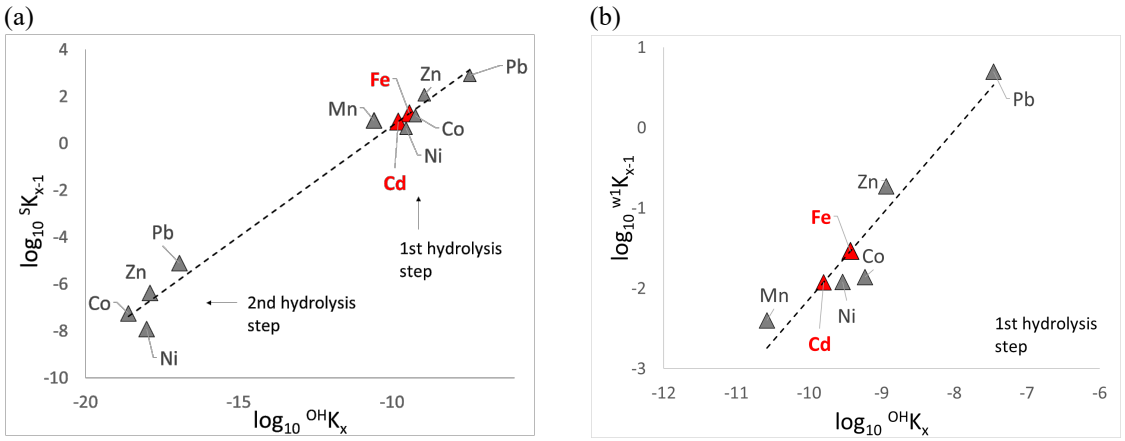

Fig. 4-36: Derivation of Cd(II) and Fe(II) surface complexation from the LFER approach on illite using the surface complexation constants updated in this work (App. A, Tab. A-2) and the hydrolysis constants from the TDB 2020 (App. B)

(a) Sorption on strong sites and (b) on weak sites. Dashed lines represent the linear regression corresponding to equations:

$$\log {}^{S}K_{x-1} = (10.15 \pm 0.68) + (0.94 \pm 0.05) \cdot \log {}^{OH}K_{x} \quad (R^2 = 0.98)$$

$$\log {}^{W1}K_{x-1} = (8.36 \pm 1.8) + (1.05 \pm 0.2) \cdot \log {}^{OH}K_{x} \quad (R^2 = 0.91)$$

The surface complexation constants for strong and weak sites obtained using the above LFER were applied for computing hypothetical Cd(II) and Fe(II) sorption edge and isotherm (Fig. 4-37). The cation exchange selectivity coefficient for both metals was taken as for Zn(II) due to their similar aqueous speciation.

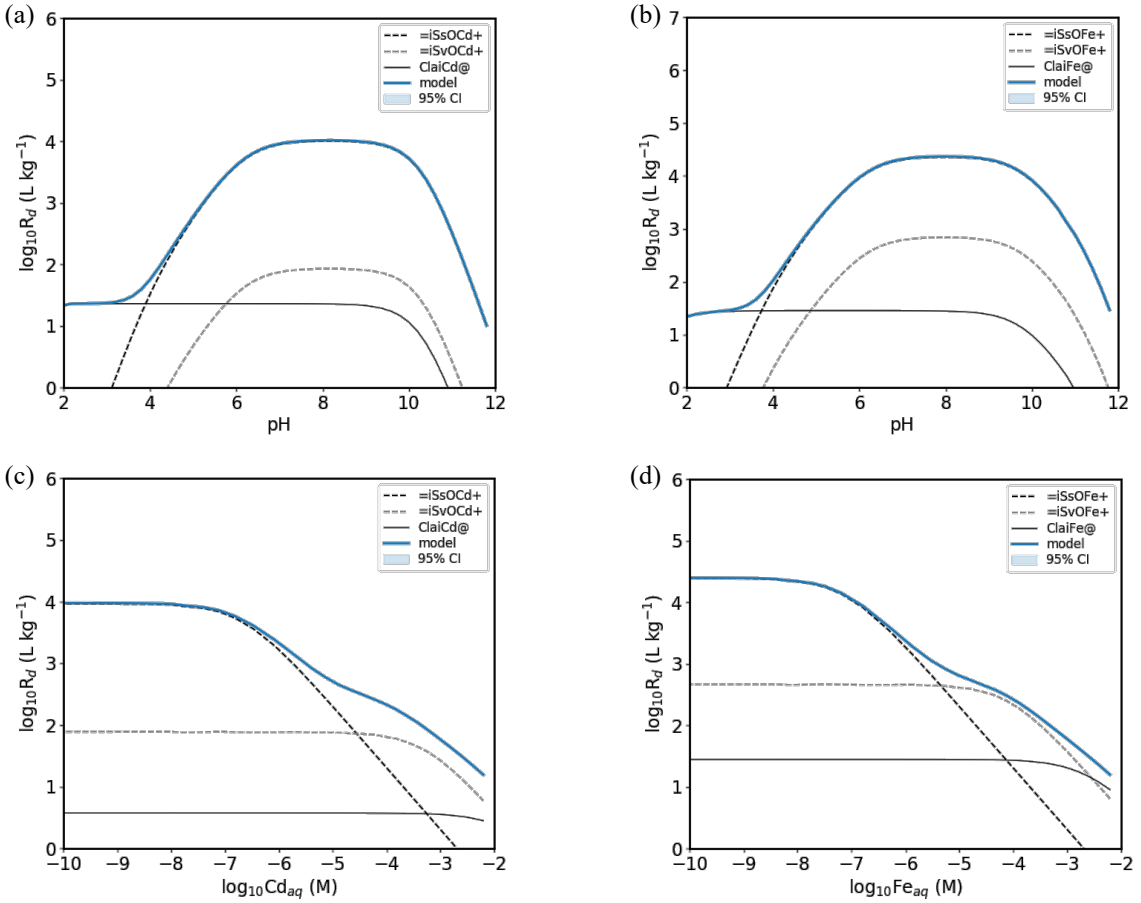

Fig. 4-37: Predicted sorption edges and isotherms for Cd(II) and Fe(II) in 0.1 M $NaClO_4$ on Na-illite

(a) pH edge for Cd(II) and (b) for Fe(II) and sorption isotherm at pH 7 for (c) Cd(II) and (d) Fe(II)

The R_d values of the resulting Cd(II) and Fe(II) pH edges and isotherms are comparable to those for montmorillonite (Fig. 4-20 and Fig. 4-22), which can be an indirect indication that the LFER-based surface complexation constants lie within values boundaries specific to 2:1 clay minerals.

The predicted Cd(II) and Fe(II) sorption edges and isotherms were also compared to the experimental data of the chemical analogues Co(II), Ni(II), and Zn(II) (Fig. 4-38).

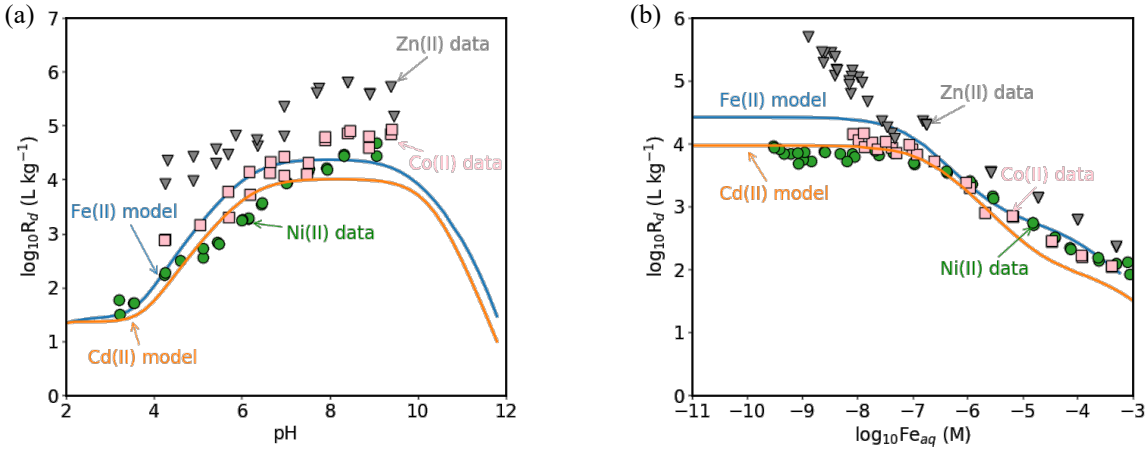

Fig. 4-38: Comparison of predicted sorption edges and isotherms for Cd(II) and Fe(II) with chemical analogue data in 0.1 M $NaClO_4$ on Na-illite

(a) pH edge and (b) isotherm at pH 7. Data taken from Marques Fernandes et al. (2015), Montoya et al. (2018), Poinssot et al. (1999)

The results of the comparison show a good match with Co(II) and Ni(II) measured data, whereas Zn(II) measured data are characterised by higher R_d values. This is probably due to the contribution of high-affinity sites of illite to Zn(II) sorption. In general, the good match of the predicted Fe(II) sorption model with measured data of chemical analogues suggests that the surface complexation constants estimated using the LFER approach are at least reasonably close to the expected real values. Only when the corresponding experimental data are available, will it be possible to determine the accuracy of these predictions.

4.3.2 Pu(III) on illite and montmorillonite

The surface complexation constants for Pu(III) on strong sites of illite and montmorillonite were derived from the surface complexation constants for Am(III) and Eu(III) updated in this work (App. A, Tab. A-2) and on the hydrolysis constants from the TDB 2020 (App. B) (Fig. 4-39).

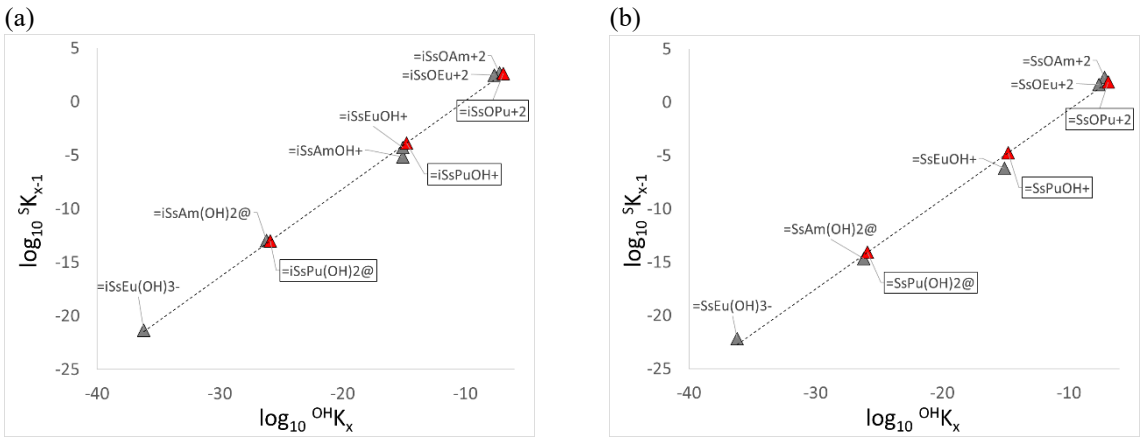

Fig. 4-39: Pu(III) surface complexation constants derived by applying the LFER approach to strong sites for (a) illite and (b) montmorillonite using the surface complexation constants of Am(III) and Eu(III) updated in this work (App. A, Tab. A-2, A-3) and the hydrolysis constants from the TDB 2020 (App. B)

Dashed lines represent the linear regression corresponding to equations:

Illite: $\log^{S}K_{x-1} = (8.29 \pm 0.51) + (0.82 \pm 0.02) \cdot \log^{OH}K_{x}$ ($R^2 = 0.99$)

Montmorillonite: $\log^{S}K_{x-1} = (7.72 \pm 0.8) + (0.84 \pm 0.04) \cdot \log^{OH}K_{x}$ ($R^2 = 0.99$)

4.3.3 Np(IV), Pu(IV), and U(IV) on illite and montmorillonite

The surface complexation constants for Np(IV), Pu(IV), and U(IV) on strong sites of illite and montmorillonite were derived based on the surface complexation constants for Th(IV) updated in this work (App. A, Tab. A-2) and the hydrolysis constants from the TDB 2020 (App. B) (Fig. 4-40).

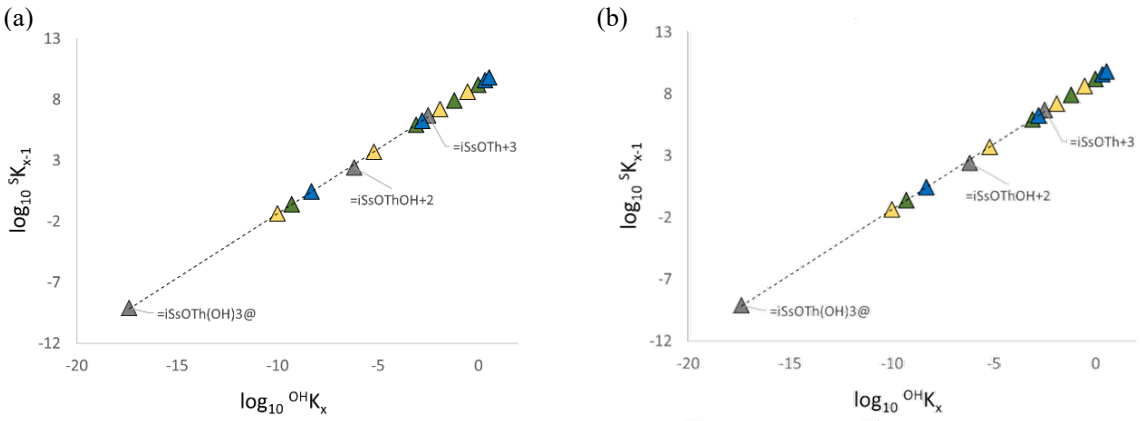

Fig. 4-40: Np(IV), Pu(IV), and U(IV) surface complexation constants derived by applying the LFER approach to strong sites for (a) illite and (b) montmorillonite using the surface complexation constants of Th(IV) updated in this work (App. A, Tab. A-2, A-3) and the hydrolysis constants from the TDB 2020 (App. B)

The triangles show sets of derived constants of Np(IV) (blue), Pu(IV) (green), and U(IV) (yellow) (App. A, Tab. A-2, A-3) corresponding to their 1st, 2nd, 3rd, and 4th hydrolysis constants (App. B). Dashed lines represent the linear regression corresponding to equations:

Illite: $\log^{S}K_{x-1} = (9.19 \pm 0.3) + (1.06 \pm 0.03) \cdot \log^{OH}K_{x}$ ($R^2 = 0.99$)

Montmorillonite: $\log^{S}K_{x-1} = (9.59 \pm 0.69) + (1.09 \pm 0.06) \cdot \log^{OH}K_{x}$ ($R^2 = 0.99$)

5 Summary

The ClaySor model, i.e., the GEMS implementation of the 2SPNE SC/CE sorption model (see Chapter 2), was made consistent with the chemical thermodynamic database TDB 2020 resulting in the updated Sorption Thermodynamic Database (STDB) for illite and montmorillonite. The brief model description and the specifics of its implementation in GEMS, as well as the non-adjustable basis model parameters (site capacities, protolysis constants) are given in Chapter 2. The uncertainties of the surface complexation constants and selectivity coefficients were determined via Monte Carlo simulations carried out using the GEMSFITS package and are given at a 95% confidence level. The procedure of the model parameter optimization and the uncertainty estimation are outlined in Chapter 3.

The results of Cs(I), Cd(II), Co(II), Fe(II), Mn(II), Ni(II), Pb(II), Ra(II), Zn(II), Am(III), Cm(III) (illite only), Eu(III), Sn(IV), Th(IV), Nb(V), Np(V), Pa(V), and U(VI) sorption modelling using the ClaySor model have been summarised in Chapter 4. The model parametrisation is based primarily on the "in-house" published investigations, complemented by "in-house" unpublished datasets and the data found in the open literature.

To derive the surface complexation constants for Cd(II) and Fe(II) on illite, as well as the surface complexation constants for Pu(III, IV), Np(IV), and U(IV) on illite and montmorillonite, the linear relationship between the stability constants of aqueous and surface complexes, commonly known as linear free energy relationships (LFERs), was used. This approach demonstrated a good performance in predicting surface complexation constants for bivalent transition metals, lanthanides and trivalent and tetravalent actinides shown in previous studies. In this study, the estimated values were applied to predict pH edges and adsorption isotherms for Cd(II) and Fe(II) on illite, which were compared to the experimental data of chemical analogues (Ni, Co, Zn), reinforcing the reliability of the surface complexation constants estimated using LFERs (Section 4.3). To determine the quality of these predictions, more experimental data are necessary.

The directly adjusted model parameters such as provisional standard Gibbs energies of surface species, along with the derived equilibrium constants of surface complexation reactions for both strong and weak sites of illite and montmorillonite, as well as cation exchange selectivity coefficients, are tabulated in App. A. The metal aqueous hydrolysis constants from the chemical thermodynamic database TDB 2020 are listed in App. B. Additionally, the experimental conditions of sorption measurements and summaries of batch sorption experiments on illite and montmorillonite used for the sorption model development are given in App. C.

The provided model can be used to calculate equilibrium sorption values such as R_d for clay minerals in host rocks and buffer materials used as engineered barriers in a deep geological repository.

6 Acknowledgements

This work was part of Nagra's scientific investigations for Stage 3 of the Sectoral Plan under the guidance and coordination of Drs. S. Serno and R. Wüst. We would like to convey our appreciation to Dr. B. Baeyens for his valuable input to this work and his improvements to the document. Numerous staff members at Nagra (incl. A. Paulsen, A. Brown, R. Wüst) edited the manuscript and Nagra's Graphics Office supported the final formatting. We would also like to express our sincere thanks to Professor V. Brendler (Helmholtz-Zentrum Dresden-Rossendorf, Germany) for the thorough scientific review of the manuscript. The project was financed through Nagra.

7 References

Baes, C.F. & Mesmer, R.E. (1976): The hydrolysis of cations. Wiley, New York.

Baeyens, B. & Bradbury, M.H. (1997): A mechanistic description of Ni and Zn sorption on Na-montmorillonite. Part I: Titration and sorption measurements. J. Contam. Hydrol. 27, 199-222.

Baeyens, B. & Bradbury, M.H. (2004): Cation exchange capacity measurements on illite using the sodium and cesium isotope dilution technique: Effects of the index cation, electrolyte concentration and competition: Modeling. Clays Clay Miner. 52, 421-431.

Baeyens, B. & Bradbury, M.H. (2017): The development of a thermodynamic sorption data base for montmorillonite and the application to bentonite. Nagra Technical Report NTB 17-13.

Baeyens, B. & Marques Fernandes, M. (2018): Adsorption of heavy metals including radionuclides. In Developments in Clay Science pp. 125-172.

Bradbury, M.H. & Baeyens, B. (1995): A quantitative mechanistic description of Ni, Zn and Ca sorption on Na-montorillonite. Part III: Modelling. Nagra Technical Report NTB 95-06.

Bradbury, M.H. & Baeyens, B. (1997): A mechanistic description of Ni and Zn sorption on Na-montmorillonite. Part II: Modelling. J. Contam. Hydrol. 27, 223-248.

Bradbury, M.H. & Baeyens, B. (2000): A generalised sorption model for the concentration dependent uptake of caesium by argillaceous rocks. J. Contam. Hydrol. 42, 141-163.

Bradbury, M.H. & Baeyens, B. (2002a): A Comparison of Apparent Diffusion Coefficients Measured in Compacted Kunigel V1 Bentonite with those Calculated from Batch Sorption Measurements and De (HTO) Data: A Case Study for Cs(I), Ni(II), Sm(III), Am(III), Zr(IV) and Np(V). Nagra Technical Report NTB 02-17.

Bradbury, M.H. & Baeyens, B. (2002b): Porewater chemistry in compacted re-saturated MX-80 bentonite: Physico-chemical characterisation and geochemical modelling. Nagra Technical Report NTB 01-08.

Bradbury, M.H. & Baeyens, B. (2002c): Sorption of Eu on Na- and Ca-montmorillonites: Experimental investigations and modelling with cation exchange and surface complexation. Geochim. Cosmochim. Acta 66, 2325-2334.

Bradbury, M.H. & Baeyens, B. (2005a): Experimental and Modelling Investigations on Na-Illite: Acid-Base Behaviour and the Sorption of Strontium, Nickel, Europium and Uranyl. Nagra Technical Report NTB 04-02.

Bradbury, M.H. & Baeyens, B. (2005b): Modelling the sorption of Mn(II), Co(II), Ni(II), Zn(II), Cd(II), Eu(III), Am(III), Sn(IV), Th(IV), Np(V) and U(VI) on montmorillonite: Linear free energy relationships and estimates of surface binding constants for some selected heavy metals and actinides. Geochim. Cosmochim. Acta 69, 875-892.

Bradbury, M.H. & Baeyens, B. (2006): Modelling sorption data for the actinides Am(III), Np(V) and Pa(V) on montmorillonite. In Radiochimica Acta pp. 619-625.

Bradbury, M.H. & Baeyens, B. (2009a): Sorption modelling on illite Part I: Titration measurements and the sorption of Ni, Co, Eu and Sn. Geochim. Cosmochim. Acta 73, 990-1003.

Bradbury, M.H. & Baeyens, B. (2009b): Sorption modelling on illite. Part II: Actinide sorption and linear free energy relationships. Geochim. Cosmochim. Acta 73, 1004-1013.

Bradbury, M.H. & Baeyens, B. (2017): The development of a thermodynamic sorption data base for illite and the application to argillaceous rocks. Nagra Technical Report NTB 17-14.

Brouwer, E., Baeyens, B., Maes, A. & Cremers, A. (1983): Cesium and rubidium ion equilibria in illite clay. J. Phys. Chem. 87, 1213-1219.

Brown, P.L., Ekberg, C., 2016. Hydrolysis of Metal Ions, Hydrolysis of Metal Ions. Wiley-VCH Verlag GmbH, Weinheim, Germany, 910 pp.

Chen, P., Van Loon, L.R., Fernandes, M. do S.M., Churakov, S., 2022. Sorption mechanism of Fe(II) on illite: Sorption and modelling. Appl. Geochemistry 143, 105389.

Comans, R.N.J., Haller, M. & De Preter, P. (1991): Sorption of cesium on illite: Non-equilibrium behaviour and reversibility. Geochim. Cosmochim. Acta 55, 433-440.

Curti, E. (2023): Bentonite pore waters (BPW) for the Sectoral Plan, phase SGT-3: Model development, testing and final calculations. Nagra Working Report NAB 22-43.

Dähn, R., Baeyens, B. & Bradbury, M.H. (2011): Investigation of the different binding edge sites for Zn on montmorillonite using P-EXAFS - The strong/weak site concept in the 2SPNE SC/CE sorption model. Geochim. Cosmochim. Acta 75, 5154-5168.

Davis, J.A. & Kent, D.B. (1990): Surface complexation modelling in aqueous geochemistry eds. M. F. J. Hochell and A. F. White. Miner. Interface Geochemistry 23, 177-260.

Dent, A.J., Ramsay, J.D.F. & Swanton, S.W. (1992): An EXAFS study of uranyl ion in solution and sorbed onto silica and montmorillonite clay colloids. J. Colloid Interface Sci. 150, 45-60.

Ervanne, H., Hakanen, M. & Lehto, J. (2014): Modelling of niobium sorption on clay minerals in sodium and calcium perchlorate solutions. Radiochim. Acta 102, 839-847.

Gabis V. (1958): Etude préliminaire des argiles oligocènes du Puy-en-Velay (Haute-Loire). Bull. Mineral. 81, 183-185.

Gaines, G.L. & Thomas, H.C. (1953): Adsorption studies on clay minerals. Part II. A formulation of the thermodynamics of exchange adsorption. J. Chem. Phys. 21, 714-718.

Gamsjäger, H., Bugajski, J., Gajda, T., Lemire, R.J. & Preis, W. (2005): Chemical Thermodynamics of Nickel. Chemical Thermodynamics, Vol. 6. Elsevier, Amsterdam, 617 pp.

Gamsjäger, H., Gajda, T., Sangster, J., Saxena, S.K. & Voigt, W. (2012): Chemical Thermodynamics of Tin. Chemical Thermodynamic Series, Vol. 12, OECD NEA, Issy-les-Moulineaux, France, 609 pp.

Giffaut, E., Grivé, M., Blanc, P., Vieillard, P., Colàs, E., Gailhanou, H., Gaboreau, S., Marty, N., Madé, B. & Duro, L. (2014): Andra thermodynamic database for performance assessment: ThermoChimie. Appl. Geochemistry 49, 225-236.

Gorgeon, L. (1994): Contribution à la modélisation physico-chimique de la retention de radio-eléments à vie longue par des materiaux argileux. Université Paris 6.

Grenthe, I., Fuger, J., Konings, R.J.M., Lemire, R.J., Muller, A.B., Nguyen-Trung C., & Wanner, H. (1992): Chemical Thermodynamics of Uranium. Chemical Thermodynamics, Vol. 1. North-Holland, Amsterdam, 715 pp.

Guillaumont, R., Fanghänel, T., Fuger, J., Grenthe, I., Neck, V., Palmer, D.A. & Rand, M.H. (2003): Update of the Chemical Thermodynamics of Uranium, Neptunium, Plutonium, Americium and Technetium. Chemical Thermodynamics, Vol. 5. Elsevier, Amsterdam, 919 pp.

Hill M. C. and Tiedeman C. R. (2007): Effective Groundwater Model Calibration: With Analysis of Data, Sensitivities, Predictions, and Uncertainty.

Hummel, W., Berner, U., Curti, E., Pearson, F.J. & Thoenen, T. (2002): Nagra/PSI chemical thermodynamic data base 01/01. In Radiochimica Acta pp. 805-813.

Hummel, W. & Thoenen, T. (2023): The PSI Chemical Thermodynamic Database 2020. Nagra Technical Report NTB 21-03.

Ishidera, T., Okazaki, M., Yamada, Y., Tomura, T. & Shibutani. S. (2023): Sorption of Sn and Nb on montmorillonite at neutral to alkaline pH. J. Nucl. Sci. Technol. 60, 536-546.

Itami, K. & Yanai, J. (2006): Sorption and desorption properties of Cadmium and Copper on soil clays in relation to charge characteristics. Soil Sci. Plant Nutr. 52, 5-12.

Johnson S.G. (2007): The NLopt nonlinear-optimisation package.

Kim, Y., Kirkpatrick, R.J. & Cygan, R.T. (1996): 133Cs NMR study of cesium on the surfaces of kaolinite and illite. Geochim. Cosmochim. Acta 60, 4059-4074.

Klinkenberg, M., Brandt, F., Baeyens, B., Bosbach, D. & Fernandes, M.M. (2021): Adsorption of barium and radium on montmorillonite: A comparative experimental and modelling study. Appl. Geochemistry 135, 105-117.

Kulik, D.A., Marques Fernandes, M. & Baeyens, B. (2018): The 2SPNE SC/CE sorption model in GEM-Selektor v.3.4 code package (ClaySor): Implementation, tests, and user guide. Nagra Arbeitsbericht NAB 18-27.

Kulik, D.A., Glaus, M.A., Gimmi, T., Van Loon, L.R. & Wüst, R. (2023): Claysordif: A New Model For Radionuclide Sorption And Diffusion In Argillaceous Media (Gems Implementation And Verification Against Phreeqc Results And Experimental Data). In Migration 2023. Nantes - France. September 24-29, 2023. Book of abstracts Nantes.

Kulik, D.A. & Miron, G.D. (2024): Solubility Limits for Model Opalinus Clay Porewaters as Input for Sorption (SDB) and Diffusion (DDB) Databases. Nagra Arbeitsbericht NAB 23-07.

Kulik, D.A., Wagner, T., Dmytrieva, S.V., Kosakowski, G., Hingerl, F.F., Chudnenko, K.V. & Berner, U.R. (2013): GEM-Selektor geochemical modeling package: Revised algorithm and GEMS3K numerical kernel for coupled simulation codes. Comput. Geosci. 17, 1-24.

Lemire, R.J., Fuger, J., Nitsche, H., Potter, P., Rand, M.H., Rydberg, J., Spahiu, K., Sullivan, J.C., Ullman, W.J., Vitorge, P. & Wanner, H. (2001): Chemical Thermodynamics of Neptunium and Plutonium. Chemical Thermodynamics, Vol. 4. Elsevier, Amsterdam, 845 pp.

Marques Fernandes, M. & Baeyens, B. (2019): Cation exchange and surface complexation of lead on montmorillonite and illite including competitive adsorption effects. Appl. Geochemistry 100, 190-202.

Marques Fernandes, M. & Baeyens, B. (2020): Competitive adsorption on illite and montmorillonite: Experimental and modelling investigations. Nagra Technical Report NTB 19-05.

Marques Fernandes, M., Baeyens, B., Dähn, R., Scheinost, A.C. & Bradbury, M.H. (2012): U(VI) sorption on montmorillonite in the absence and presence of carbonate: A macroscopic and microscopic study. Geochim. Cosmochim. Acta 93, 262-277.

Marques Fernandes, M., Klinkenberg, M., Baeyens, B., Bosbach, D. & Brandt, F. (2023): Adsorption of Ba and 226Ra on illite: A comparative experimental and modelling study. Appl. Geochemistry 159, 105815.

Marques Fernandes, M., Marinich, O., Miron, G.D. & Baeyens, B. (2024): Sorption of Cs, Ni, Eu, Th and U on Rock Samples of Opalinus Clay and Confining Geological Units from Deep Boreholes in the Jura Ost, Nördlich Lägern and Zürich Nordost Siting Regions: Measurements and Predictive Sorption Modelling. Nagra Technical Report NTB 23-01.

Marques Fernandes, M., Vér, N. & Baeyens, B. (2015): Predicting the uptake of Cs, Co, Ni, Eu, Th and U on argillaceous rocks using sorption models for illite. Appl. Geochemistry 59, 189-199.

Mazurek, M., Wersin, P., Hadi, J., Grenèche, J.M., Prinpreecha, N. & Traber, D. (2023): Geochemistry and palaeo-hydrogeology of the weathered zone in the Opalinus Clay. Appl. Clay Sci. 232.

Miron, G.D., Kulik, D.A., Dmytrieva, S.V. & Wagner, T. (2015): GEMSFITS: Code package for optimisation of geochemical model parameters and inverse modeling. Appl. Geochemistry 55, 28-45.

Missana, T., Alonso, U., Mayordomo, N. & García-Gutiérrez, M. (2023): Analysis of Cadmium Retention Mechanisms by a Smectite Clay in the Presence of Carbonates. Toxics 11.

Montoya, V., Baeyens, B., Glaus, M.A., Kupcik, T., Marques Fernandes, M., Van Laer, L., Bruggeman, C., Maes, N. & Schäfer, T. (2018): Sorption of Sr, Co and Zn on illite: Batch experiments and modelling including Co in-diffusion measurements on compacted samples. Geochim. Cosmochim. Acta 223, 1-20.

Neck, V. & Kim, J.I. (2001): Solubility and hydrolysis of tetravalent actinides. Radiochim. Acta 89, 1-16.

Poinssot, C., Baeyens, B. & Bradbury, M.H. (1999): Experimental studies of Cs, Sr, Ni and Eu sorption on Na-illite and the modelling of Cs sorption. Nagra Technical Report NTB 99-04.

Powell, M.J.D. (2009): The BOBYQA algorithm for bound constrained optimisation without derivatives. Report DAMTP 2009/NA06, University of Cambridge.

Powell, K.J., Brown, P.L., Byrne, R.H., Gajda, T., Hefter, G., Leuz, A.K., Sjöberg, S., Wanner, H., 2011. Chemical speciation of environmentally significant metals with inorganic ligands. Part 4: The Cd^{2+} + OH^-, Cl^-, CO_3^{2-}, SO_4^{2-}, and PO_4^{3-} systems (IUPAC technical report). Pure Appl. Chem. 83, 1163–1214.

Rabung, T., Pierret, M.C., Bauer, A., Geckeis, H., Bradbury, M.H. & Baeyens, B. (2005): Sorption of Eu(III)/Cm(III) on Ca-montmorillonite and Na-illite. Part 1: Batch sorption and time-resolved laser fluorescence spectroscopy experiments. Geochim. Cosmochim. Acta 69, 5393-5402.

Rand, M., Fuger, J., Grenthe, I., Neck, V. & Rai, D. (2008): Chemical Thermodynamics of Thorium. Chemical Thermodynamics, Vol. 11. OECD Publishing, Paris, 900 pp.

Reinholdt, M.X., Miehé-Brendlé, J., Delmotte, L., Tuilier, M.-H., Le Dred, R., Cortès, R., Flank, A.-M. (2001): Fluorine route synthesis of montmorillonites containing Mg or Zn and characterization by XRD, thermal analysis, MAS NMR, and EXAFS spectroscopy. Eur. J. Inor. Chem. 11, 2831–2841.

Reinholdt, M.X., Brendlé, J., Tuilier, M.-H., Kaliaguine, S., Ambroise, E. (2013): Hydrothermal Synthesis and Characterization of Ni-Al Montmorillonite-Like Phyllosilicates. Nanomaterials. 3, 48-69.

Soltermann, D., Baeyens, B., Bradbury, M.H. & Fernandes M.M. (2014): Fe(II) uptake on natural montmorillonites. II. Surface complexation modeling. Environ. Sci. Technol. 48, 8698-8705.

Soltermann, D., Fernandes, M.M., Baeyens, B., Dähn, R., Miehé-Brendlé, J., Wehrli, B. & Bradbury, M.H. (2013): Fe(II) sorption on a synthetic montmorillonite. A combined macroscopic and spectroscopic study. Environ. Sci. Technol. 47, 6978-6986.

Sposito, O. (1984): The Surface Chemistry of Soils., Oxford University Press, New York, NY.

Staunton, S. & Roubaud, M. (1997): Adsorption of 137Cs on montmorillonite and illite: Effect of charge compensating cation, ionic strength, concentration of Cs, K and fulvic acid. Clays Clay Minerals. 45, 251-260.

Tennøe, S., Halnes, G. & Einevoll, G.T. (2018): Uncertainpy: A Python Toolbox for Uncertainty Quantification and Sensitivity Analysis in Computational Neuroscience. Front. Neuroinform. 12.

Thoenen, T., Hummel, W., Berner, U. & Curti, E. (2014): The PSI/Nagra Chemical Thermodynamic Database 12/07. PSI Report 14-04.

Tournassat, C., Bourg, I. C., Steefel, C. I., & Bergaya, F. (2015). Surface Properties of Clay Minerals. In C. Tournassat, I. C. Bourg, C. I. Steefel, & F. Bergaya (Eds.), Developments in Clay Science: Vol. 6 Natural and Engineered Clay Barriers 5-31. Elsevier.

Trubert, D., Le Naour, C., Jaussaud, C. & Mrad, O. (2003): Hydrolysis of Protactinium(V). III. Determination of Standard Thermodynamic Data. J. Solution Chem. 32, 505-517.

Vanselow A.P. (1932): The utilization of the base-exchange reaction for the determination of activity coefficients in mixed electrolytes. J. Am. Chem. Soc. 54, 1307-1311.

Wagner T., Kulik D.A., Hingerl F.F., Dmytrieva S.V. (2012): GEM-Selektor geochemical modeling package: TSolMod library and data interface for multicomponent phase models. Canadian Mineralogist 50, 1173-1195.

Westall, J.C., Zachary J.L. & Morel, F.M.M. (1976): MINEQL: A computer program for the calculation of chemical eqilibrium composition of aqueous systems., Dept. of Civil Eng., Massachusetts Institute of Technology, Cambridge, Massachusetts.

Wick, S., Baeyens, B., Marques Fernandes, M. & Voegelin, A. (2018): Thallium Adsorption onto Illite. Environ. Sci. Technol. 52, 571-580.

Zachara, J.M., Smith, S.C., McKinley, J.P. & Resch, C.T. (1993): Cadmium Sorption on Specimen and Soil Smectites in Sodium and Calcium Electrolytes. Soil Sci. Soc. Am. J. 57, 1491-1501.

App. A Optimised surface complexation constants and ion exchange selectivity coefficients for illite and montmorillonite (ClaySor 2023 sorption thermodynamic database)

The following tables comprise the parameters of the updated ClaySor 2023 model. The non-adjustable (site capacities) and adjustable (ion exchange selectivity coefficients) parameters of the Generalised Caesium Sorption model (GCS) are given in Tab. A-1. The surface complexation reactions of the elements, the optimised $G°_{298}$ of surface complexes, and the equilibrium constants for strong and weak 1st type sites as well as their uncertainties estimated in the present work for illite and montmorillonite are listed in Tab. A-2 and Tab. A-3 respectively. Surface complexation constants as well as optimised $G°_{298}$ of surface complexes for Ra(II) on weak 2nd type sites are given in Tab. A-4.

The optimised $G°_{298}$ of cation exchange species and selectivity coefficients for illite and montmorillonite are listed in Tab. A-5 and Tab. A-6, respectively. The values of selectivity coefficients are represented as logarithms of selectivity coefficients in both Gaines and Thomas ($\log_{10}K_c$) and Vanselow ($\log_{10}K_V$) conventions in order to be consistent with previous works, which mostly rely on the former convention, and to allow calculations in GEMS, which uses the later convention. All selectivity coefficients except that for Ra(II) are obtained by simultaneously fitting the data-sets with different electrolyte concentrations, mainly 0.01 and 0.1 M $NaClO_4$. Since the specific ion-interaction theory (SIT) is chosen in TDB 2020 as the method for estimating activity coefficients, the proposed selectivity coefficients could be applied to the systems with ionic strength values typical for most natural waters. The Ra(II) selectivity coefficients shown in Tab. A-5 and Tab. A-6 were obtained based on the dataset with the background ionic strength of 0.3 M. The details on the thermodynamic sorption model and parameters for each element can be found in Chapter 4.

Tab. A-1: Summary of GCS model parameters (site types and capacities) and selectivity coefficients (K_c) for the cation exchange equilibria on the three site types of illite for Cs^+, K^+, NH_4^+, Ca^{2+}, Mg^{2+}, and Sr^{2+} w.r.t. Na on illite with a CEC = 225 meq kg^{-1}

Site type	**Frayed edge sites (FES)**		
% of CEC	0.25%		
Site capacity (meq kg^{-1})	0.5625		
Exchange equilibrium	**$^{CE}G°_{298}$, kJ·mol^{-1}**	**$\log_{10}[K_c]$**	**$\log_{10}[K_V]$**
$Cs^+ + Na^+$-illite ⇔ **Cs^+-illite** + Na^+	-319.33 ± 0.27	6.64 ± 0.05[1]	6.64 ± 0.05
$K^+ + Na^+$-illite ⇔ **K^+-illite** + Na^+	-286.18 ± 1.14	2.4 ± 0.2[2]	2.4 ± 0.2
$NH_4^+ + Na^+$-illite ⇔ **NH_4^+-illite** + Na^+	-88.77 ± 1.71	3.4 ± 0.3[3]	3.4 ± 0.3
$Ca^{2+} + 2Na^+$-illite ⇔ **Ca^{2+}-illite** + $2Na^+$	-532.17	0.2 ± 0.1[3]	-0.1 ± 0.1
$Mg^{2+} + 2Na^+$-illite ⇔ **Mg^{2+}-illite** + $2Na^+$	-434.74	0.2 ± 0.1[4]	-0.1 ± 0.1
$Sr^{2+} + 2Na^+$-illite ⇔ **Sr^{2+}-illite** + $2Na^+$	-543.23	0.2 ± 0.1[4]	-0.1 ± 0.1
Site type	**Type II sites (T2S)**		
% of CEC	20%		
Site capacity (meq kg^{-1})	45		
Exchange equilibrium	**$^{CE}G°_{298}$, kJ·mol^{-1}**	**$\log_{10}[K_c]$**	**$\log_{10}[K_V]$**
$Cs^+ + Na^+$-illite ⇔ **Cs^+-illite** + Na^+	-298.71 ± 4.86	3.03 ± 0.85[1]	3.03 ± 0.85
$K^+ + Na^+$-illite ⇔ **K^+-illite** + Na^+	-284.46 ± 1.14	2.1 ± 0.2[2]	2.1 ± 0.2
$NH_4^+ + Na^+$-illite ⇔ **NH_4^+-illite** + Na^+	-81.35 ± 0.57	2.1 ± 0.1[3]	2.1 ± 0.1
$Ca^{2+} + 2Na^+$-illite ⇔ **Ca^{2+}-illite** + $2Na^+$	-531.03	0.0 ± 0.1[3]	-0.3 ± 0.1
$Mg^{2+} + 2Na^+$-illite ⇔ **Mg^{2+}-illite** + $2Na^+$	-433.60	0.0 ± 0.1[4]	-0.3 ± 0.1
$Sr^{2+} + 2Na^+$-illite ⇔ **Sr^{2+}-illite** + $2Na^+$	-542.09	0.0 ± 0.1[4]	-0.3 ± 0.1
Site type	**Planar sites (PS)**		
% of CEC	~ 80%		
Site capacity (meq kg^{-1})	180		
Exchange equilibrium	**$^{CE}G°_{298}$, kJ·mol^{-1}**	**$\log_{10}[K_c]$**	**$\log_{10}[K_V]$**
$Cs^+ + Na^+$-illite ⇔ **Cs^+-illite** + Na^+	-289.96 ± 4.23	1.49 ± 0.74[1]	1.49 ± 0.74
$K^+ + Na^+$-illite ⇔ **K^+-illite** + Na^+	-278.76 ± 1.14	1.1 ± 0.2[2]	1.1 ± 0.2
$NH_4^+ + Na^+$-illite ⇔ **NH_4^+-illite** + Na^+	-74.50 ± 0.57	0.9 ± 0.1[3]	0.9 ± 0.1
$Ca^{2+} + 2Na^+$-illite ⇔ **Ca^{2+}-illite** + $2Na^+$	-533.31	0.4 ± 0.2[3]	0.1 ± 0.2
$Mg^{2+} + 2Na^+$-illite ⇔ **Mg^{2+}-illite** + $2Na^+$	-435.88	0.4 ± 0.2[4]	0.1 ± 0.2
$Sr^{2+} + 2Na^+$-illite ⇔ **Sr^{2+}-illite** + $2Na^+$	-544.37	0.4 ± 0.2[4]	0.1 ± 0.2

[1] Results obtained during this study.
[2] The values of selectivity coefficients are taken from Bradbury & Baeyens (2017). The uncertainty is taken as a provisional value.
[3] Taken from Wick et al. (2018).
[4] Assumed to be identical to that for Ca^{2+}.

Tab. A-2: Surface complexation reactions and equilibrium constants for Cd(II), Co(II), Fe(II), Mn(II), Ni(II), Pb(II), Zn(II), Am(III), Cm(III), Eu(III), Pu(III, IV), Np(IV, V), Sn(IV), Th(IV), Nb(V), Pa(V), and U(IV, VI) on illite

Surface complex formation reaction	**$^{S}G°_{298}$, kJ·mol^{-1}**	**$\log_{10}{}^{S}K$**	**$^{W1}G°_{298}$, kJ·mol^{-1}**	**$\log_{10}{}^{W1}K$**
≡SOH + Cd^{2+} ⇔ **≡SOCd^{+}** + H^{+}	-320.22	0.93*	-303.96	-1.92*
≡SOH + Co^{2+} ⇔ **≡SOCo^{+}** + H^{+} ≡SOH + Co^{2+} + H_2O ⇔ **≡SOCoOH^{0}** + $2H^{+}$	-299.51 ± 0.65 -488.55 ± 3.21	1.18 ± 0.11 -7.25 ± 0.56	-282.15 ± 3.75	-1.86 ± 0.66
≡SOH + Fe^{2+} ⇔ **≡SOFe^{+}** + H^{+}	-335.21	1.28*	-319.11	-1.54*
≡SOH + Mn^{2+} ⇔ **≡SOMn^{+}** + H^{+}	-471.02 ± 0.53	0.98 ± 0.09	-451.76 ± 1.34	-2.4 ± 0.24
≡SOH + Ni^{2+} ⇔ **≡SONi^{+}** + H^{+} ≡SOH + Ni^{2+} + H_2O ⇔ **≡SONiOH^{0}** + $2H^{+}$	-286.65 ± 0.24 -474.90 ± 0.86	0.65 ± 0.04 -7.92 ± 0.15	-272.00 ± 0.71	-1.92 ± 0.12
≡SOH + Pb^{2+} ⇔ **≡SOPb^{+}** + H^{+} ≡SOH + Pb^{2+} + H_2O ⇔ **≡SOPbOH^{0}** + $2H^{+}$	-277.95 ± 1.26 -469.42 ± 1.37	2.90 ± 0.22 -5.11 ± 0.24	-265.41 ± 1.66	0.70 ± 0.29
≡SOH + Zn^{2+} ⇔ **≡SOZn^{+}** + H^{+} ≡SOH + Zn^{2+} + H_2O ⇔ **≡SOZnOH^{0}** + $2H^{+}$	-396.19 ± 0.80 -585.14 ± 1.17	2.07 ± 0.14 -6.37 ± 0.21	-380.22 ± 1.07	-0.73 ± 0.19
≡SOH + Am^{3+} ⇔ **≡SOAm^{2+}** + H^{+} ≡SOH + Am^{3+} + H_2O ⇔ **≡SOAmOH^{+}** + $2H^{+}$ ≡SOH + Am^{3+} + $2H_2O$ ⇔ **≡SOAm(OH)$_2^{0}$** + $3H^{+}$	-851.27 ± 1.51 -1,043.51 ± 8.87 -1,236.18 ± 0.38	2.69 ± 0.26 -5.17 ± 1.55 -12.96 ± 0.07		
≡SOH + Am^{3+} ⇔ **≡SOAm^{2+}** + H^{+} ≡SOH + Am^{3+} + $2H_2O$ ⇔ **≡SOAm(OH)$_2^{0}$** + $3H^{+}$	-851.48 ± 1.52 -1,236.46 ± 0.43	2.73 ± 0.27 -12.91 ± 0.07		
≡SOH + Cm^{3+} ⇔ **≡SOCm^{2+}** + H^{+} ≡SOH + Cm^{3+} + H_2O ⇔ **≡SOCmOH^{+}** + $2H^{+}$	-847.20 ± 1.16 -1,051.57 ± 2.15	2.56 ± 0.2 -3.18 ± 0.38		
≡SOH + Eu^{3+} ⇔ **≡SOEu^{2+}** + H^{+} ≡SOH + Eu^{3+} + H_2O ⇔ **≡SOEuOH^{+}** + $2H^{+}$ ≡SOH + Eu^{3+} + $3H_2O$ ⇔ **≡SOEu(OH)$_3^{-}$** + $4H^{+}$	-827.16 ± 2.30 -1,025.82 ± 0.94 -1,402.72 ± 0.99	2.47 ± 0.4 -4.28 ± 0.17 -21.34 ± 0.17	-818.79 ± 1.11	1.00 ± 0.19
≡SOH + Pu^{3+} ⇔ **≡SOPu^{2+}** + H^{+} ≡SOH + Pu^{3+} + H_2O ⇔ **≡SOPuOH^{+}** + $2H^{+}$ ≡SOH + Pu^{3+} + $2H_2O$ ⇔ **≡SOPu(OH)$_2^{0}$** + $3H^{+}$	-831.14 -1,031.18 -1,216.26	2.62* -3.88* -13*		
≡SOH + Np^{4+} ⇔ **≡SONp^{3+}** + H^{+} ≡SOH + Np^{4+} + H_2O ⇔ **≡SONpOH^{2+}** + $2H^{+}$ ≡SOH + Np^{4+} + $2H_2O$ ⇔ **≡SONp(OH)$_2^{+}$** + $3H^{+}$ ≡SOH + Np^{4+} + $3H_2O$ ⇔ **≡SONp(OH)$_3^{0}$** + $4H^{+}$	-784.75 -1,020.69 -1,238.82 -1,442.86	9.77* 9.56* 6.23* 0.43*		
≡SOH + Pu^{4+} ⇔ **≡SOPu^{3+}** + H^{+} ≡SOH + Pu^{4+} + H_2O ⇔ **≡SOPuOH^{2+}** + $2H^{+}$ ≡SOH + Pu^{4+} + $2H_2O$ ⇔ **≡SOPu(OH)$_2^{+}$** + $3H^{+}$ ≡SOH + Pu^{4+} + $3H_2O$ ⇔ **≡SOPu(OH)$_3^{0}$** + $4H^{+}$	-767.64 -997.53 -1,223.26 -1,423.01	9.19* 7.92* 5.92* -0.63*		
≡SOH + Sn^{4+} + $3H_2O$ ⇔ **≡SOSn(OH)$_3^{0}$** + $4H^{+}$ ≡SOH + Sn^{4+} + $4H_2O$ ⇔ **≡SOSn(OH)$_4^{-}$** + $5H^{+}$ ≡SOH + Sn^{4+} + $5H_2O$ ⇔ **≡SOSn(OH)$_5^{2-}$** + $6H^{+}$	-992.44 ± 1.16 -1,193.45 ± 1.63 -1,382.02 ± 0.73	15.86 ± 0.20 9.53 ± 0.29 1.02 ± 0.13		
≡SOH + Th^{4+} ⇔ **≡SOTh^{3+}** + H^{+} ≡SOH + Th^{4+} + H_2O ⇔ **≡SOThOH^{2+}** + $2H^{+}$ ≡SOH + Th^{4+} + $3H_2O$ ⇔ **≡SOTh(OH)$_3^{0}$** + $4H^{+}$ ≡SOH + Th^{4+} + $4H_2O$ ⇔ **≡SOTh(OH)$_4^{-}$** + $5H^{+}$	-980.39 ± 9.21 -1,192.86 ± 5.17 -1,601.34 ± 8.92 -1,803.74 ± 0.74	6.73 ± 1.61 2.41 ± 0.91 -9.12 ± 1.56 -15.20 ± 0.13		
≡SOH + U^{4+} ⇔ **≡SOU^{3+}** + H^{+} ≡SOH + U^{4+} + H_2O ⇔ **≡SOUOH^{2+}** + $2H^{+}$ ≡SOH + U^{4+} + $2H_2O$ ⇔ **≡SOU(OH)$_2^{+}$** + $3H^{+}$ ≡SOH + U^{4+} + $3H_2O$ ⇔ **≡SOU(OH)$_3^{0}$** + $4H^{+}$	-816.29 -1,045.21 -1,262.48 -1,470.74	8.62* 7.18* 3.7* -1.36*		

Tab. A-2: Cont.

Surface complex formation reaction	**$^{S}G°_{298}$, kJ·mol^{-1}**	**$\log_{10}{}^{S}K$**	**$^{W1}G°_{298}$, kJ·mol^{-1}**	**$\log_{10}{}^{W1}K$**
≡SOH + $Nb(OH)_4^+$ + H_2O ⇔ **≡SONb(OH)$_5^-$** + $2H^+$	-1,674.53 ± 1.23	0.74 ± 0.22		
≡SOH + $Nb(OH)_4^+$ + $2H_2O$ ⇔ **≡SONb(OH)$_6^{2-}$** + $3H^+$	-1,874.71 ± 3.06	-5.74 ± 0.54		
≡SOH + NpO_2^+ ⇔ **≡SONpO$_2^0$** + H^+	-1,137.43 ± 1.28	-1.32 ± 0.22		
≡SOH + NpO_2^+ + H_2O ⇔ **≡SONpO$_2$OH$^-$** + $2H^+$	-1,324.69 ± 2.06	-10.06 ± 0.36		
≡SOH + $PaOOH^{+2}$ ⇔ **≡SOPaOOH$^+$** + H^+	-1,326.03 ± 0.75	6.51 ± 0.13		
≡SOH + $PaOOH^{+2}$ + H_2O ⇔ **≡SOPaO$_2$OH$^-$** + $3H^+$	-1,498.11 ± 0.78	-4.89 ± 0.14		
≡SOH + $PaOOH^{+2}$ + $2H_2O$ ⇔ **≡SOPaO$_2$(OH)$_2^{2-}$** + $4H^+$	-1,683.26 ± 1.18	-14.00 ± 0.21		
≡SOH + UO_2^{2+} ⇔ **≡SOUO$_2^+$** + H^+	-1,203.26 ± 1.00	2.37 ± 0.17	-1,184.99 ± 1.33	-0.83 ± 0.23
≡SOH + UO_2^{2+} + H_2O ⇔ **≡SOUO$_2$OH^0** + $2H^+$	-1,401.60 ± 4.68	-4.43 ± 0.82	-1,394.92 ± 0.73	-5.60 ± 0.13
≡SOH + UO_2^{2+} + $2H_2O$ ⇔ **≡SOUO$_2$(OH)$_2^-$** + $3H^+$	-1,600.80 ± 1.49	-11.07 ± 0.26	-1,593.68 ± 0.88	-12.32 ± 0.15
≡SOH + UO_2^{2+} + $3H_2O$ ⇔ **≡SOUO$_2$(OH)$_3^{2-}$** + $4H^+$	-1,791.05 ± 1.04	-19.29 ± 0.18		

* Derived from LFER.

Tab. A-3: Surface complexation reactions and equilibrium constants for Cd(II), Co(II), Fe(II), Mn(II), Ni(II), Pb(II), Zn(II), Am(III), Eu(III), Pu(III, IV), Np(IV, V), Sn(IV), Th(IV), Nb(V), Pa(V), and U(IV, VI) on montmorillonite

Surface complex formation reaction	$^{S}G°_{298}$, kJ·mol^{-1}	$\log_{10}{}^{S}K$	$^{W1}G°_{298}$, kJ·mol^{-1}	$\log_{10}{}^{W1}K$
≡SOH + Cd^{2+} ⇔ **≡SOCd^{+}** + H^{+}	-309.06 ± 1.72	-1.03 ± 0.3	-297.03 ± 3.53	-3.13 ± 0.62
≡SOH + Co^{2+} ⇔ **≡SOCo^{+}** + H^{+}	-291.75 ± 0.72	-0.18 ± 0.13	-272.75 ± 0.46	-3.51 ± 0.08
≡SOH + Co^{2+} + H_2O ⇔ **≡SOCoOH^{0}** + $2H^{+}$	-476.88 ± 1.78	-9.29 ± 0.31		
≡SOH + Fe^{2+} ⇔ **≡SOFe^{+}** + H^{+}	-337.62 ± 0.96	1.70 ± 0.17	-318.66 ± 1.35	-1.62 ± 0.24
≡SOH + Mn^{2+} ⇔ **≡SOMn^{+}** + H^{+}	-461.85 ± 0.96	-0.63 ± 0.17	-445.57 ± 0.70	-3.48 ± 0.12
≡SOH + Ni^{2+} ⇔ **≡SONi^{+}** + H^{+}	-278.34 ± 0.32	-0.81 ± 0.06	-262.72 ± 1.49	-3.54 ± 0.26
≡SOH + Ni^{2+} + H_2O ⇔ **≡SONiOH^{0}** + $2H^{+}$	-466.27 ± 0.47	-9.43 ± 0.08		
≡SOH + Pb^{2+} ⇔ **≡SOPb^{+}** + H^{+}	-269.25 ± 0.84	1.37 ± 0.15	-254.02 ± 1.44	-1.30 ± 0.25
≡SOH + Pb^{2+} + H_2O ⇔ **≡SOPbOH^{0}** + $2H^{+}$	-454.17 ± 3.01	-7.78 ± 0.53		
≡SOH + Zn^{2+} ⇔ **≡SOZn^{+}** + H^{+}	-389.99 ± 0.83	0.98 ± 0.15	-370.94 ± 0.87	-2.36 ± 0.15
≡SOH + Am^{3+} ⇔ **≡SOAm^{2+}** + H^{+}	-849.14 ± 0.70	2.32 ± 0.12		
≡SOH + Am^{3+} + $2H_2O$ ⇔ **≡SOAm(OH)$_2^{0}$** + $3H^{+}$	-1,226.36 ± 0.87	-14.68 ± 0.15		
≡SOH + Eu^{3+} ⇔ **≡SOEu^{2+}** + H^{+}	-822.53 ± 0.57	1.65 ± 0.10	-810.50 ± 0.90	-0.45 ± 0.16
≡SOH + Eu^{3+} + H_2O ⇔ **≡SOEuOH^{+}** + $2H^{+}$	-1,014.69 ± 1.69	-6.23 ± 0.3		
≡SOH + Eu^{3+} + $3H_2O$ ⇔ **≡SOEu(OH)$_3^{-}$** + $4H^{+}$	-1,397.96 ± 0.99	-22.17 ± 0.17		
≡SOH + Pu^{3+} ⇔ **≡SOPu^{2+}** + H^{+}	-827.09	1.91*		
≡SOH + Pu^{3+} + H_2O ⇔ **≡SOPuOH^{+}** + $2H^{+}$	-1,026.32	-4.73*		
≡SOH + Pu^{3+} + $2H_2O$ ⇔ **≡SOPu(OH)$_2^{0}$** + $3H^{+}$	-1,210.15	-14.07*		
≡SOH + Np^{4+} ⇔ **≡SONp^{3+}** + H^{+}	-787.15	10.19*		
≡SOH + Np^{4+} + H_2O ⇔ **≡SONpOH^{2+}** + $2H^{+}$	-1,023.03	9.97*		
≡SOH + Np^{4+} + $2H_2O$ ⇔ **≡SONp(OH)$_2^{+}$** + $3H^{+}$	-1,240.71	6.56*		
≡SOH + Np^{4+} + $3H_2O$ ⇔ **≡SONp(OH)$_3^{0}$** + $4H^{+}$	-1,443.77	0.59*		
≡SOH + Pu^{4+} ⇔ **≡SOPu^{3+}** + H^{+}	-769.92	9.59*		
≡SOH + Pu^{4+} + H_2O ⇔ **≡SOPuOH^{2+}** + $2H^{+}$	-999.64	8.29*		
≡SOH + Pu^{4+} + $2H_2O$ ⇔ **≡SOPu(OH)$_2^{+}$** + $3H^{+}$	-1,225.02	6.23*		
≡SOH + Pu^{4+} + $3H_2O$ ⇔ **≡SOPu(OH)$_3^{0}$** + $4H^{+}$	-1,423.75	-0.5*		
≡SOH + Sn^{4+} + $3H_2O$ ⇔ **≡SOSn(OH)$_3^{0}$** + $4H^{+}$	-994.54 ± 0.93	16.23 ± 0.16	-980.33 ± 1.36	13.74 ± 0.24
≡SOH + Sn^{4+} + $4H_2O$ ⇔ **≡SOSn(OH)$_4^{-}$** + $5H^{+}$			-1,174.54 ± 0.94	6.22 ± 0.17
≡SOH + Sn^{4+} + $5H_2O$ ⇔ **≡SOSn(OH)$_5^{2-}$** + $6H^{+}$	-1,372.39 ± 0.63	-0.67 ± 0.11		
≡SOH + Th^{4+} ⇔ **≡SOTh^{3+}** + H^{+}	-983.63 ± 1.89	7.30 ± 0.33		
≡SOH + Th^{4+} + H_2O ⇔ **≡SOThOH^{2+}** + $2H^{+}$	-1,192.30 ± 4.92	2.31 ± 0.86		
≡SOH + Th^{4+} + $3H_2O$ ⇔ **≡SOTh(OH)$_3^{0}$** + $4H^{+}$	-1,601.16 ± 1.63	-9.15 ± 0.29		
≡SOH + Th^{4+} + $4H_2O$ ⇔ **≡SOTh(OH)$_4^{-}$** + $5H^{+}$	-1,794.19 ± 0.97	-16.88 ± 0.17		
≡SOH + U^{4+} ⇔ **≡SOU^{3+}** + H^{+}	-818.51	9.01*		
≡SOH + U^{4+} + H_2O ⇔ **≡SOUOH^{2+}** + $2H^{+}$	-1047.21	7.53*		
≡SOH + U^{4+} + $2H_2O$ ⇔ **≡SOU(OH)$_2^{+}$** + $3H^{+}$	-1263.91	3.95*		
≡SOH + U^{4+} + $3H_2O$ ⇔ **≡SOU(OH)$_3^{0}$** + $4H^{+}$	-1471.31	-1.26*		
≡SOH + $Nb(OH)_4^{+}$ + H_2O ⇔ **≡SONb(OH)$_5^{-}$** + $2H^{+}$	-1,674.46 ± 1.33	0.73 ± 0.23	-1,656.63 ± 1.33	-2.40 ± 0.23
≡SOH + $Nb(OH)_4^{+}$ + $2H_2O$ ⇔ **≡SONb(OH)$_6^{2-}$** + $3H^{+}$			-1,844.05 ± 3.70	-11.11 ± 0.65

Tab. A-3: Cont.

Surface complex formation reaction	$^{S}G°_{298}$, kJ·mol^{-1}	$\log_{10}{}^{S}K$	$^{W1}G°_{298}$, kJ·mol^{-1}	$\log_{10}{}^{W1}K$
≡SOH + NpO_2^+ ⇔ **≡SONpO_2^0** + H^+	-1,130.00 ± 0.65	-2.63 ± 0.11		
≡SOH + NpO_2^+ + H_2O ⇔ **≡SONpO_2OH$^-$** + 2H^+	-1,310.42 ± 1.31	-12.56 ± 0.23		
≡SOH + $PaOOH^{+2}$ ⇔ **≡SOPaOOH$^+$** + H^+	-1,327.19 ± 1.14	6.71 ± 0.20		
≡SOH + $PaOOH^{+2}$ ⇔ **≡SOPaO_2^0** + 2H^+	-1,294.81 ± 1.57	1.04 ± 0.28		
≡SOH + $PaOOH^{+2}$ + H_2O ⇔ **≡SOPaO_2OH$^-$** + 3H^+	-1,487.27 ± 1.77	-6.79 ± 0.31		
≡SOH + $PaOOH^{+2}$ + 2H_2O ⇔ **≡SOPaO_2(OH)$_2^{2-}$** + 4H^+	-1,672.14 ± 1.33	-15.95 ± 0.23		
≡SOH + UO_2^{2+} ⇔ **≡SOUO_2^+** + H^+	-1,206.48 ± 0.57	2.93 ± 0.10	-1,190.11 ± 1.77	0.07 ± 0.31
≡SOH + UO_2^{2+} + H_2O ⇔ **≡SOUO_2OH^0** + 2H^+	-1,402.82 ± 2.28	-4.21 ± 0.40	-1,393.62 ± 1.88	-5.83 ± 0.33
≡SOH + UO_2^{2+} + 3H_2O ⇔ **≡SOUO_2(OH)$_3^{2-}$** + 4H^+	-1,780.62 ± 3.92	-21.12 ± 0.69		

Tab. A-4: Surface complexation constants for Ra(II) on weak type 2 sites of illite and montmorillonite

Mineral	Surface complex formation reaction	$^{W2}G°_{298}$, kJ·mol^{-1}	$\log_{10}{}^{W2}K$
Illite	≡SOH + Ra^{2+} ⇔ **≡SORa$^+$** + H^+	-776.71 ± 1.71	-3.85 ± 0.30
Montmorillonite		-771.29 ± 1.19	-4.80 ± 0.21

Tab. A-5: Cation exchange reactions and corresponding selectivity coefficients (K_c and K_V) for Na-illite

Cation exchange reaction	**$^{CE}G°_{298}$, kJ·mol^{-1}**	**$\log_{10}[K_c]$**	**$\log_{10}[K_V]$**
Na^+-clay + $Cs^+ \Leftrightarrow Cs^+$-clay + Na^+	-289.96 ± 4.23	1.49 ± 0.74[1]	1.49 ± 0.74
Na^+-clay + $K^+ \Leftrightarrow K^+$-clay + Na^+	-278.76 ± 1.14	1.1 ± 0.2[2]	1.1 ± 0.2
Na^+-clay + $NH_4^+ \Leftrightarrow NH_4^+$-clay + Na^+	-74.50 ± 0.57	0.9 ± 0.1[3]	0.9 ± 0.1
$2Na^+$-clay + $Ba^{2+} \Leftrightarrow Ba^{2+}$-clay + $2Na^+$	-541.87	1.05[5]	0.75
$2Na^+$-clay + $Ca^{2+} \Leftrightarrow Ca^{2+}$-clay + $2Na^+$	-533.31	0.4 ± 0.2[3]	0.1 ± 0.2
$2Na^+$-clay + $Cd^{2+} \Leftrightarrow Cd^{2+}$-clay + $2Na^+$	-59.38	0.60[2]	0.3
$2Na^+$-clay + $Co^{2+} \Leftrightarrow Co^{2+}$-clay + $2Na^+$	-37.85 ± 3.53	0.71 ± 0.62	0.41 ± 0.62
$2Na^+$-clay + $Fe^{2+} \Leftrightarrow Fe^{2+}$-clay + $2Na^+$	-72.37	0.60[2]	0.3
$2Na^+$-clay + $Mg^{2+} \Leftrightarrow Mg^{2+}$-clay + $2Na^+$	-435.88	0.4 ± 0.2[4]	0.1 ± 0.2
$2Na^+$-clay + $Mn^{2+} \Leftrightarrow Mn^{2+}$-clay + $2Na^+$	-208.84 ± 2.68	0.41 ± 0.47	0.11 ± 0.47
$2Na^+$-clay + $Ni^{2+} \Leftrightarrow Ni^{2+}$-clay + $2Na^+$	-28.13 ± 0.41	0.73 ± 0.07	0.43 ± 0.07
$2Na^+$-clay + $Pb^{2+} \Leftrightarrow Pb^{2+}$-clay + $2Na^+$	-15.45 ± 3.69	2.28 ± 0.65	1.98 ± 0.65
$2Na^+$-clay + $Ra^{2+} \Leftrightarrow Ra^{2+}$-clay + $2Na^+$	-558.10 ± 0.67	3.22 ± 0.12[7]	2.92 ± 0.12
$2Na^+$-clay + $Sr^{2+} \Leftrightarrow Sr^{2+}$-clay + $2Na^+$	-544.37	0.4 ± 0.2[4]	0.1 ± 0.2
$2Na^+$-clay + $Zn^{2+} \Leftrightarrow Zn^{2+}$-clay + $2Na^+$	-128.85	0.60[8]	0.3
$3Na^+$-clay + $Am^{3+} \Leftrightarrow Am^{3+}$-clay + $3Na^+$	-575.62 ± 0.52	1.71 ± 0.09	1.23 ± 0.09
$3Na^+$-clay + $Eu^{3+} \Leftrightarrow Eu^{3+}$-clay + $3Na^+$	-553.23 ± 0.87	1.78 ± 0.15	1.3 ± 0.15
Na^+-clay + $NpO_2^+ \Leftrightarrow NpO_2^+$-clay + Na^+	-897.98 ± 2.55	0.04 ± 0.45	0.04 ± 0.45
$2Na^+$-clay + $UO_2^{2+} \Leftrightarrow UO_2^{2+}$-clay + $2Na^+$	-934.50	0.65[9]	0.35

[1] Results obtained during this study.

[2] The values of selectivity coefficients are taken from Bradbury & Baeyens (2017). The uncertainty is taken as a provisional value.

[3] Taken from Wick et al. (2018).

[4] Assumed to be identical to that for Ca^{2+}.

[5] Taken from Marques Fernandes et al. (2023).

[6] Assumed to be to be identical to that for Zn.

[7] For 0.3 M NaCl (see Section 4.1.6).

[8] Taken from Montoya et al (2018).

[9] In this study, it was not possible to obtain the optimum selectivity coefficient for the cation exchange of UO_2^{2+} on Na-illite due to the low sensitivity of this parameter. As a result, it was removed from the optimised function. The previously estimated value by Bradbury & Baeyens (2017) is specified instead.

Tab. A-6: Cation exchange reactions and corresponding selectivity coefficients (log K_c) for Na-montmorillonite

Cation exchange reaction	**$^{CE}G°_{298}$, kJ·mol^{-1}**	**log** [K_c]	**log** [K_V]
Na^+-clay + Cs^+ ⇔ Cs^+-clay + Na^+	-287.68 ± 2.13	1.10 ± 0.37	1.10 ± 0.37
Na^+-clay + K^+ ⇔ K^+-clay + Na^+	-275.91	0.602 ± 0.22[1]	0.602 ± 0.22[2]
2Na^+-clay + Ba^{2+} ⇔ Ba^{2+}-clay + 2Na^+	-538.24	0.9[3]	0.6
2Na^+-clay + Ca^{2+} ⇔ Ca^{2+}-clay + 2Na^+	-533.28	0.415 ± 0.27[1]	0.095 ± 0.27[2]
2Na^+-clay + Cd^{2+} ⇔ Cd^{2+}-clay + 2Na^+	-59.80 ± 0.20	0.67 ± 0.03	0.37 ± 0.03
2Na^+-clay + Co^{2+} ⇔ Co^{2+}-clay + 2Na^+	-37.06	0.57	0.27[4]
2Na^+-clay + Fe^{2+} ⇔ Fe^{2+}-clay + 2Na^+	-76.54 ± 0.63	1.33 ± 0.11	1.03 ± 0.11
2Na^+-clay + Mg^{2+} ⇔ Mg^{2+}-clay + 2Na^+	-435.48	0.342 ± 0.3[1]	0.03 ± 0.3[2]
2Na^+-clay + Mn^{2+} ⇔ Mn^{2+}-clay + 2Na^+	-209.21 ± 0.53	0.48 ± 0.09	0.18 ± 0.09
2Na^+-clay + Ni^{2+} ⇔ Ni^{2+}-clay + 2Na^+	-27.27 ± 0.32	0.57 ± 0.06	0.27 ± 0.06
2Na^+-clay + Pb^{2+} ⇔ Pb^{2+}-clay + 2Na^+	-9.20 ± 2.09	1.18 ± 0.37	0.88 ± 0.37
2Na^+-clay + Ra^{2+} ⇔ Ra^{2+}-clay + 2Na^+	-547.34 ± 0.73	1.34 ± 0.13	1.03 ± 0.13
2Na^+-clay + Sr^{2+} ⇔ Sr^{2+}-clay + 2Na^+	-544.45	0.415 ± 0.27[1]	0.113 ± 0.27[2]
2Na^+-clay + Zn^{2+} ⇔ Zn^{2+}-clay + 2Na^+	-128.87	0.59[5]	0.29
3Na^+-clay + Am^{3+} ⇔ Am^{3+}-clay + 3Na^+	-575.23 ± 0.52	1.64 ± 0.09	1.16 ± 0.09
3Na^+-clay + Eu^{3+} ⇔ Eu^{3+}-clay + 3Na^+	-551.83 ± 0.81	1.53 ± 0.14	1.06 ± 0.14
Na^+-clay + NpO_2^+ ⇔ NpO_2^+-clay + Na^+	-898.02 ± 0.68	0.04 ± 0.12	0.04 ± 0.12
2Na^+-clay + UO_2^{2+} ⇔ UO_2^{2+}-clay + 2Na^+	-933.42 ± 1.72	0.46 ± 0.3	0.16 ± 0.3

[1] Taken from Bradbury & Baeyens (2002b).
[2] Taken from Curti (2023). The uncertainty value is provisionally assumed to be the same as for the log [K_c] value.
[3] Taken from Klinkenberg et al. (2021).
[4] Assumed to be the same as for Ni.
[5] Taken from previous investigations (Baeyens & Bradbury 1995).

App. B Metal hydrolysis equilibrium constants used in the development of sorption thermodynamic databases for illite and montmorillonite (in accordance with the TDB 2020)

The table contains the hydrolysis reactions and the values for the constants from the TDB 2020 (Hummel & Thoenen, 2023) with the original references except for the Co(II) data, which were taken from the ThermoChimie thermodynamic database, version 11a (Giffaut et al. 2014).

Tab. B-1: Hydrolysis reactions and constant values from the TDB 2020 (Hummel & Thoenen, 2023) with the original references except for the Co(II) data, which were taken from the ThermoChimie thermodynamic database (Giffaut et al. 2014).

Metal	Hydrolysis reactions	log ^{OH}K	Reference
Cd(II)	$Cd^{2+} + H_2O \Leftrightarrow CdOH^+ + H^+$	-9.8	Powell et al. (2011)
	$Cd^{2+} + 2H_2O \Leftrightarrow Cd(OH)_2^0 + 2H^+$	-20.19	
	$Cd^{2+} + 3H_2O \Leftrightarrow Cd(OH)_3^- + 3H^+$	-33.5	
	$Cd^{2+} + 4H_2O \Leftrightarrow Cd(OH)_4^{2-} + 4H^+$	-47.28	
Co(II)	$Co^{2+} + H_2O \Leftrightarrow CoOH^+ + H^+$	-9.23	Giffaut et al. (2014)
	$Co^{2+} + 2H_2O \Leftrightarrow Co(OH)_2^0 + 2H^+$	-18.6	
	$Co^{2+} + 3H_2O \Leftrightarrow Co(OH)_3^- + 3H^+$	-31.7	
	$Co^{2+} + 4H_2O \Leftrightarrow Co(OH)_4^{2-} + 4H^+$	-46.42	
Fe(II)	$Fe^{2+} + H_2O \Leftrightarrow FeOH^+ + H^+$	-9.43	Brown & Ekberg (2016)
	$Fe^{2+} + 2H_2O \Leftrightarrow Fe(OH)_2^0 + 2H^+$	-20.52	
	$Fe^{2+} + 3H_2O \Leftrightarrow Fe(OH)_3^- + 3H^+$	-32.68	
Mn(II)	$Mn^{2+} + H_2O \Leftrightarrow MnOH^+ + H^+$	-10.58	Brown & Ekberg (2016)
	$Mn^{2+} + 2H_2O \Leftrightarrow Mn(OH)_2^0 + 2H^+$	-22.18	
	$Mn^{2+} + 3H_2O \Leftrightarrow Mn(OH)_3^- + 3H^+$	-34.34	
	$Mn^{2+} + 4H_2O \Leftrightarrow Mn(OH)_4^{2-} + 4H^+$	-48.28	
Ni(II)	$Ni^{2+} + H_2O \Leftrightarrow NiOH^+ + H^+$	-9.54	Gamsjäger et al. (2005)
	$Ni^{2+} + 2H_2O \Leftrightarrow Ni(OH)_2^0 + 2H^+$	-18	
	$Ni^{2+} + 3H_2O \Leftrightarrow Ni(OH)_3^- + 3H^+$	-29.2	
Pb(II)	$Pb^{2+} + H_2O \Leftrightarrow PbOH^+ + H^+$	-7.46	Powell et al. (2009)
	$Pb^{2+} + 2H_2O \Leftrightarrow Pb(OH)_2^0 + 2H^+$	-16.94	
	$Pb^{2+} + 3H_2O \Leftrightarrow Pb(OH)_3^- + 3H^+$	-28.03	
Ra(II)	$Ra^{2+} + H_2O \Leftrightarrow RaOH^+ + H^+$	-13.7	Hummel & Thoenen (2023) (linear regression)
Zn(II)	$Zn^{2+} + H_2O \Leftrightarrow ZnOH^+ + H^+$	-8.94	Brown & Ekberg (2016)
	$Zn^{2+} + 2H_2O \Leftrightarrow Zn(OH)_2^0 + 2H^+$	-17.89	
	$Zn^{2+} + 3H_2O \Leftrightarrow Zn(OH)_3^- + 3H^+$	-27.98	
	$Zn^{2+} + 4H_2O \Leftrightarrow Zn(OH)_4^{2-} + 4H^+$	-40.35	

Tab. B-1: Cont.

Metal	Hydrolysis reactions	log ^{OH}K	Reference
Am(III)	$Am^{3+} + H_2O \Leftrightarrow AmOH^{2+} + H^+$	-7.2	Guillaumont et al. (2003)
	$Am^{3+} + 2H_2O \Leftrightarrow Am(OH)_2^+ + 2H^+$	-15.1	
	$Am^{3+} + 3H_2O \Leftrightarrow Am(OH)_3^0 + 3H^+$	-26.2	
Eu(III)	$Eu^{3+} + H_2O \Leftrightarrow EuOH^{2+} + H^+$	-7.64	Hummel et al. (2002)
	$Eu^{3+} + 2H_2O \Leftrightarrow Eu(OH)_2^+ + 2H^+$	-15.1	
	$Eu^{3+} + 3H_2O \Leftrightarrow Eu(OH)_3^0 + 3H^+$	-23.7	
	$Eu^{3+} + 4H_2O \Leftrightarrow Eu(OH)_4^- + 4H^+$	-36.2	
Sn(IV)	$Sn^{4+} + 4H_2O \Leftrightarrow Sn(OH)_4^0 + 4H^+$	7.54	Gamsjäger et al. (2012)
	$Sn^{4+} + 5H_2O \Leftrightarrow Sn(OH)_5^- + 5H^+$	-8.6	
	$Sn^{4+} + 6H_2O \Leftrightarrow Sn(OH)_6^{2-} + 6H^+$	-18.67	
Th(IV)	$Th^{4+} + H_2O \Leftrightarrow ThOH^{3+} + H^+$	-2.5	Rand et al. (2008)
	$Th^{4+} + 2H_2O \Leftrightarrow Th(OH)_2^{2+} + 2H^+$	-6.2	
	$Th^{4+} + 4H_2O \Leftrightarrow Th(OH)_4^0 + 4H^+$	-17.4	
Nb(V)	$Nb(OH)_4^+ + H_2O \Leftrightarrow Nb(OH)_5^0 + H^+$	-1.89	Hummel & Thoenen (2023)
	$Nb(OH)^{4+} + 2H_2O \Leftrightarrow Nb(OH)_6^- + 2H^+$	-6.69	
	$Nb(OH)^{4+} + 3H_2O \Leftrightarrow Nb(OH)_7^{2-} + 3H^+$	-16.09	
Np(V)	$NpO_2^+ + H_2O \Leftrightarrow NpO_2(OH)^0 + H^+$	-11.3	Lemire et al. (2001)
	$NpO_2^+ + 2H_2O \Leftrightarrow NpO_2(OH)_2^- + 2H^+$	-23.6	
Pa(V)	$PaO(OH)^{2+} + H_2O \Leftrightarrow PaO(OH)_2^+ + H^+$	-1.26	Hummel & Thoenen (2023)
	$PaO(OH)_2^+ + H_2O \Leftrightarrow PaO(OH)_3^0 + H^+$	-5.04	
	$PaO(OH)_3^0 + H_2O \Leftrightarrow PaO(OH)_4^- + H^+$	-9.4	
U(VI)	$UO_2^{2+} + H_2O \Leftrightarrow UO_2OH^+ + H^+$	-5.25	Guillaumont et al. (2003)
	$UO_2^{2+} + 2H_2O \Leftrightarrow UO_2(OH)_2^0 + 2H^+$	-12.15	"
	$UO_2^{2+} + 3H_2O \Leftrightarrow UO_2(OH)_3^- + 3H^+$	-20.25	"
	$UO_2^{2+} + 4H_2O \Leftrightarrow UO_2(OH)_4^{2-} + 4H^+$	-32.4	"
	$2UO_2^{2+} + H_2O \Leftrightarrow (UO_2)_2OH^{3+} + H^+$	-2.7	Grenthe et al. (1992)
	$2UO_2^{2+} + 2H_2O \Leftrightarrow (UO_2)_2(OH)_2^{2+} + 2H^+$	-5.62	"
	$3UO_2^{2+}\ 4H_2O \Leftrightarrow (UO_2)_3(OH)_4^{2+} + 4H^+$	-11.9	"
	$3UO_2^{2+}\ 5H_2O \Leftrightarrow (UO_2)_3(OH)_5^+ + 5H^+$	-15.55	"
	$3UO_2^{2+}\ 7H_2O \Leftrightarrow (UO_2)_3(OH)_7^- + 7H^+$	-32.2	Guillaumont et al. (2003)
	$4UO_2^{2+}\ 7H_2O \Leftrightarrow (UO_2)_4(OH)_7^+ + 7H^+$	-21.9	Grenthe et al. (1992)

App. C Sorption edge and isotherm measurements on illite and montmorillonite

In this study, we have incorporated all available in-house data, including previously unpublished sorption results (edges and/or isotherms). The unpublished experiments encompass Cs(I), Co(II), Mn(II), Ni(II), Pb(II), Zn(II), Eu(III), Th(IV), NpO_2^+, and UO_2^{2+} sorption on montmorillonite (SWy, STx, and IFM) and illite. Detailed information about these experiments, including experimental conditions, is summarised in Tab. D-1, and the outcomes of these experiments are illustrated in the figures provided in Chapter 4 and below (Fig. C-1 – C-19).

Materials

The SWy-2 montmorillonite (Crook County, Wyoming) in powdered form was obtained from the Source Clay Minerals Repository at the University of Missouri, Columbia. The synthetic iron-free montmorillonite (Na-IFM) utilised in this study is identical to the material employed in the research conducted by Soltermann et al. (2013) and was supplied by Jocelyne Brendlé from Université de Haute-Alsace, Institut de Science des Matériaux de Mulhouse. Comprehensive information on the synthesis and treatment of IFM can be found in previous studies (Reinholdt et al. 2001; Reinholdt et al. 2013). The source illite (Illite du Puy) originated from an Oligocene geological formation in the Le Puy-en-Velay region (Haute-Loire), France (Gabis, 1958). The illite samples underwent crushing, powdering in a mortar, and subsequent separation of the < 63 µm fraction through sieving.

IFM was suspended in 0.1 M NaCl and did not undergo any further treatment. SWy and IdP underwent multiple washes with 1 M NaCl to eliminate soluble salts and sparingly soluble minerals, such as calcite, converting the clay into the homoionic Na-form. The < 0.5 µm clay fraction was obtained through successive steps: peptisation via washing with deionised water pre-equilibrated with the respective clay, centrifugation (approximately 7 minutes at around 600 g maximum), collection of the supernatant suspension, and flocculation with 1 M NaCl. To remove soluble hydroxy-aluminium compounds and other acid-soluble impurities, the clay suspension underwent washing with a 0.1 M NaCl solution at pH 3.5 for 1 hour (Baeyens & Bradbury 1997). For IdP, a repeated acid washing was performed (Bradbury & Baeyens, 2009a). The conversion to the 0.1 M NaCl background concentration was achieved using the dialysis technique. Finally, the conditioned Na-clay suspensions were diluted to a sorbent concentration (S) of approximately 10 $g \cdot L^{-1}$ with the equilibrium solution and stored in the dark at 4 °C. The clay content of each batch was precisely determined by drying to a constant weight at 105 °C and correcting for the salt content. The end products comprised suspensions of the respective purified clays in the Na-form, serving as sources for the adsorption experiments.

The cation exchange capacity (CEC) of the used clays was measured by the ^{134}Cs isotopic dilution method (Baeyens & Bradbury, 2004). A significant number of CEC determinations were conducted on various SWy and IdP clay batches at neutral pH, resulting in average values of 225 ± 10 $meq \cdot kg^{-1}$ and 870 ± 35 $meq \cdot kg^{-1}$ for IdP and SWy, respectively. The CEC of the IFM was determined to be 811.0 ± 10.2 $meq \cdot kg^{-1}$ (Soltermann et al., 2013), demonstrating good agreement with the CEC of natural SWy clay.

Sorption experiments

The sorption of Cs(I), Co(II), Mn(II), Ni(II), Pb(II), Zn(II), Eu(III), Th(IV), NpO_2^+, and UO_2^{2+} on the clay samples (see Tab. D-1) was quantified through radiochemical assays using the corresponding radioisotopes. Specifically, ^{134}Cs ($t_{1/2}$ = 2.06 y), ^{63}Ni ($t_{1/2}$ = 100 y), ^{57}Co ($t_{1/2}$ = 271,79 y), ^{152}Eu ($t_{1/2}$ = 13.3 y), and ^{228}Th ($t_{1/2}$ = 1.913 y) were procured from Eckert and Ziegler, Isotope Products Laboratories (California, USA). Additionally, ^{54}Mn ($t_{1/2}$ = 312.5 d) and ^{65}Zn

($t_{1/2}$ = 343.9 d) were sourced from PerkinElmer, Inc. (Waltham, MA, USA), while ^{210}Pb ($t_{1/2}$ = 22.3 y) was obtained from the former Laboratoire de Mesure des Rayonnements Ionisants (LMRI), (CEA, France). For ^{237}Np ($t_{1/2} = 2.144 \cdot 10^6$ y) and ^{233}U ($t_{1/2} = 160 \cdot 10^3$ y), source solutions in 1 M HCl with concentrations of 0.03 M and $5 \cdot 10^{-3}$ M, respectively, were utilised. The isotopic composition and stable carrier concentration of the used tracers were either provided by the manufacturer or determined in-house by ICP-MS. The radiotracers contained no other metal impurities. Each source radioisotope solution was diluted in 25 or 50 mL of deionised water to produce an acidic stock solution. Standard solutions for use in the adsorption experiments were prepared by labelling aliquots of the given stock radiotracer solution in the background electrolyte. Each standard solution was allowed to stand at least overnight before use to ensure equilibrium (wall sorption).

All the sorption experiments, excluding Cs, were conducted in controlled N_2 atmosphere glove boxes with $CO_2 \leq 1$ ppm and $O_2 \leq 1$ ppm to prevent changes in geochemical conditions (e.g., carbonate complexation, precipitation, oxidation). Two types of batch adsorption measurements were performed: (i) sorption edges: pH-dependent sorption of fixed nuclide concentration and fixed ionic strength and (ii) adsorption isotherms: nuclide concentration-dependent sorption at fixed pH and background electrolyte concentration. A comprehensive experimental overview is provided in Tab. D-1. To prevent pH drift in the adsorption experiments, various buffers, including i.e., $CH_3COONa \cdot 3H_2O$ (sodium acetate), $C_6H_{13}NO_4S$ (MES), $C_7H_{15}NO_4S$ (MOPS), $H_2NC(CH_2OH)_3$ (TRIS) or $C_8H_{17}NO_3S$ (CHES) (BioChemika MicroSelect, Fluka), were used at concentrations of $2 \cdot 10^{-3}$ M.

For the isotherms, stable or weakly radioactive isotopes of the respective investigated nuclides were utilised, except for Np, for which ^{237}Np was also employed in the isotherm experiments. The concentrations and stability of the solutions underwent verification through ICP-OES measurement. Solutions spanning various concentration ranges were prepared at a specific pH in NaCl background electrolyte (see Tab. D-1). The batch-type experimental approach typically involves reacting aliquots of the clay suspensions over a defined period through end-over-end shaking: (i) with the radioisotope-labelled standard solutions (pH edge) or (ii) with the radioisotope-labelled stable nuclide solution of defined concentration at a constant pH and NaCl concentration (isotherm). The detailed experimental conditions (i.e., clay, S/L ratio, pH, nuclide concentration range, electrolyte) are summarised in Tab. D-1.

After a given equilibration period, phase separation was achieved using a Beckman Coulter AvantiTM J30i High-Performance Centrifuge (1 hour at 108,000g max.), and aliquots of the supernatants were assayed radiometrically. The pH of the supernatant of each sample was measured using a Metrohm combined electrode, calibrated against commercially available MerckTM buffers at pH 4, 7, and 10.

Radiochemical assays of the supernatants and the labelled standard solutions (prepared simultaneously at the start of the adsorption experiments) were performed using either a Canberra Packard TRI-CARB 2750 TR/LL liquid scintillation counter (^{63}Ni, ^{233}U, ^{210}Pb, ^{237}Np), or a Canberra Packard Cobra Quantum γ-counter (^{134}Cs, ^{60}Co, ^{152}Eu, ^{228}Th, ^{65}Zn, ^{54}Mn).

Data presentation

The results of the sorption measurements (figures in Chapter 4 and Fig. C-1 to C-19) are expressed in terms of solid-liquid distribution ratios (R_d) plotted against pH (edges) or nuclide equilibrium concentration (isotherm), with R_d (L·kg^{-1}) calculated as follows:

$$R_d = \frac{A_{init} - A_{eql}}{A_{eql}} \times \frac{V}{m}$$

where A_{init} is total initial aqueous nuclide activity (cpm), A_{eql} is the total equilibrium aqueous nuclide activity (cpm), V is the volume of liquid phase (L), and m is mass of solid phase (kg) in the given experiment.

C.1 Caesium

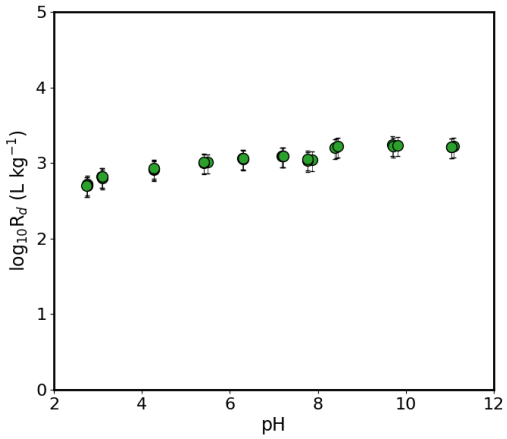

Fig. C-1: Cs(I) sorption edge measurements on Na-montmorillonite in 0.01 M $NaClO_4$

C.2 Manganese

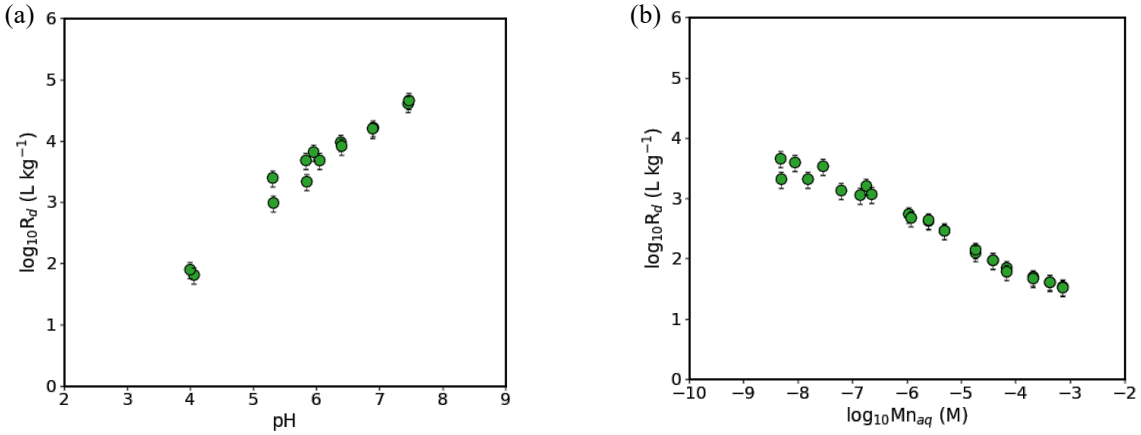

Fig. C-2: Mn(II) sorption on Na-illite in 0.1 M NaCl
(a) pH edge and (b) sorption isotherm at pH 5.95

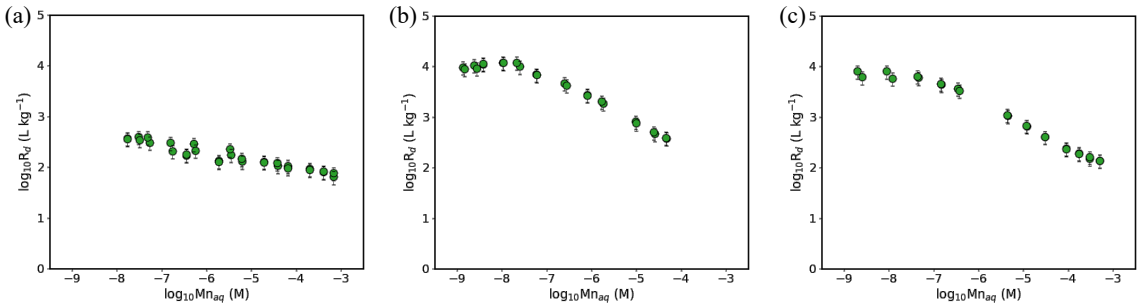

Fig. C-3: Mn(II) sorption isotherm on Na-montmorillonite in 0.1 M NaCl
(a) at pH 6, (b) at pH 8.5, (c) at pH 8.7

C.3 Nickel

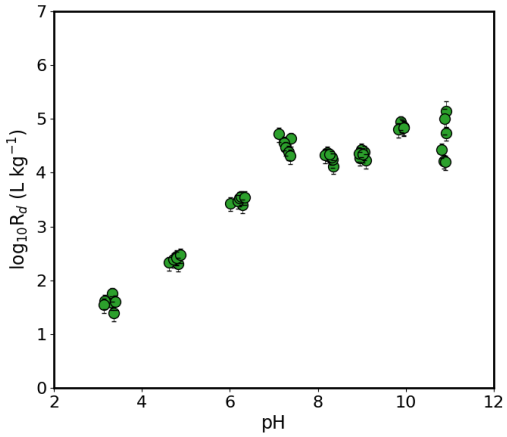

Fig. C-4: Ni(II) sorption edge measurements on Na-illite in 0.1 M $NaClO_4$

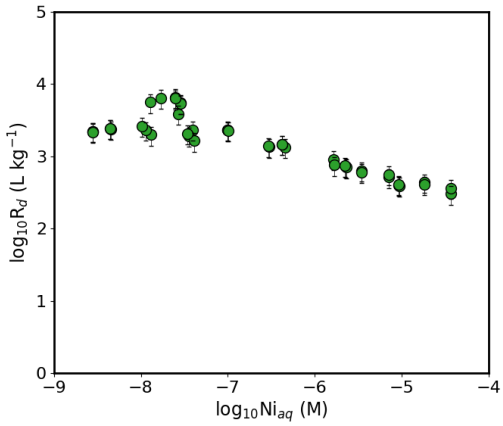

Fig. C-5: Ni(II) sorption isotherm on Na-montmorillonite at pH 7.7 in 0.1 M $NaClO_4$

C.4 Lead

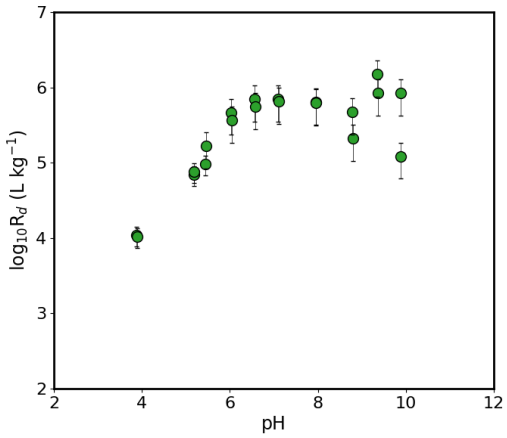

Fig. C-6: Pb(II) pH edge on Na-illite in 0.1 M NaCl

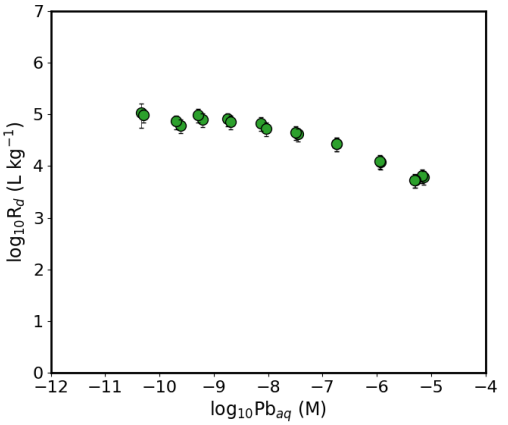

Fig. C-7: Pb(II) sorption isotherm on Na-montmorillonite at pH 8 in 0.1 M NaClO4

C.5 Zinc

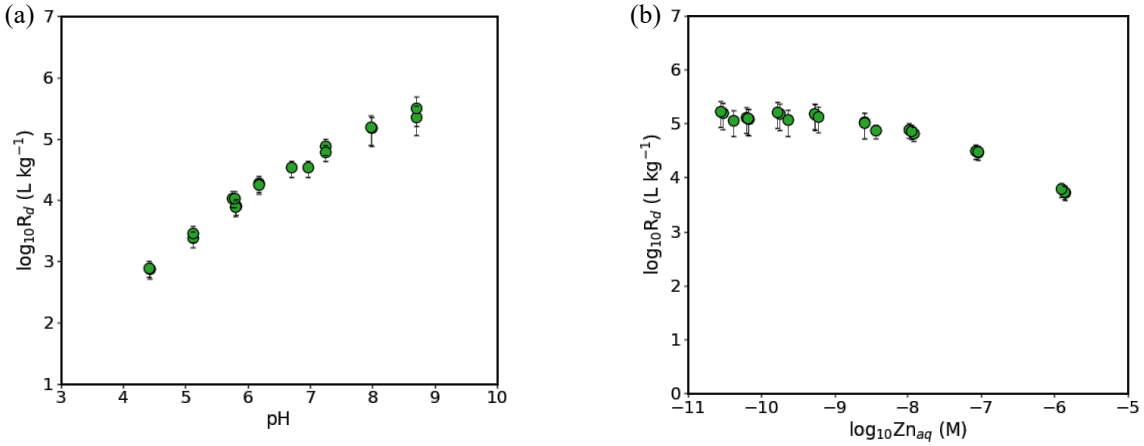

Fig. C-8: Zn(II) sorption on Na-montmorillonite in 0.1 M $NaClO_4$
(a) pH edge and (b) sorption isotherm at pH 7.7

C.6 Europium

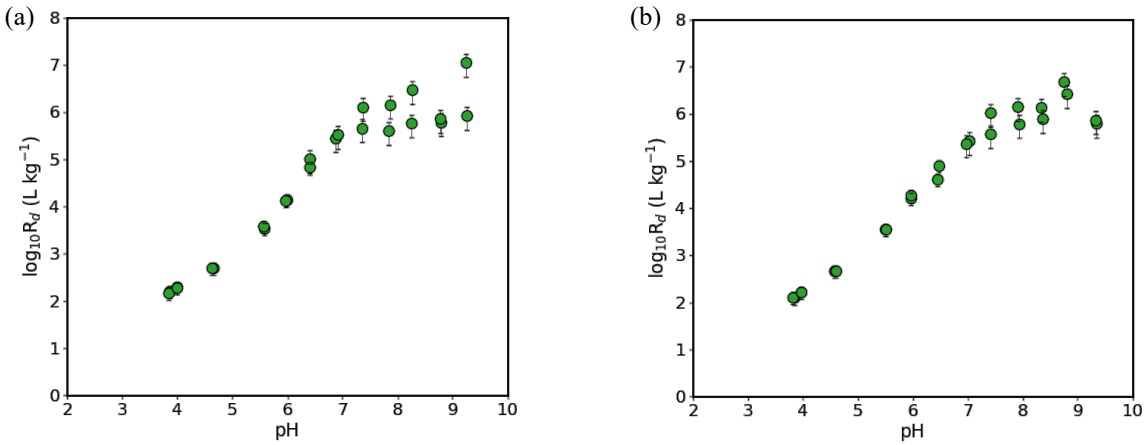

Fig. C-9: pH edges of Eu(III) on Na-illite
(a) in 0.6 M $NaClO_4$ and (b) in 1 M $NaClO_4$

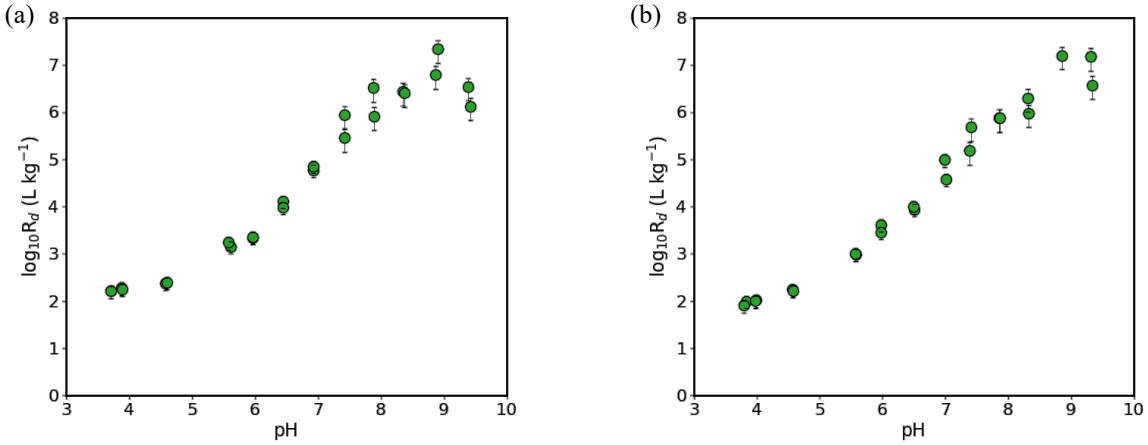

Fig. C-10: pH edges of Eu(III) on Na-montmorillonite
(a) in 0.3 M NaCl and (b) in 0.6 M NaCl

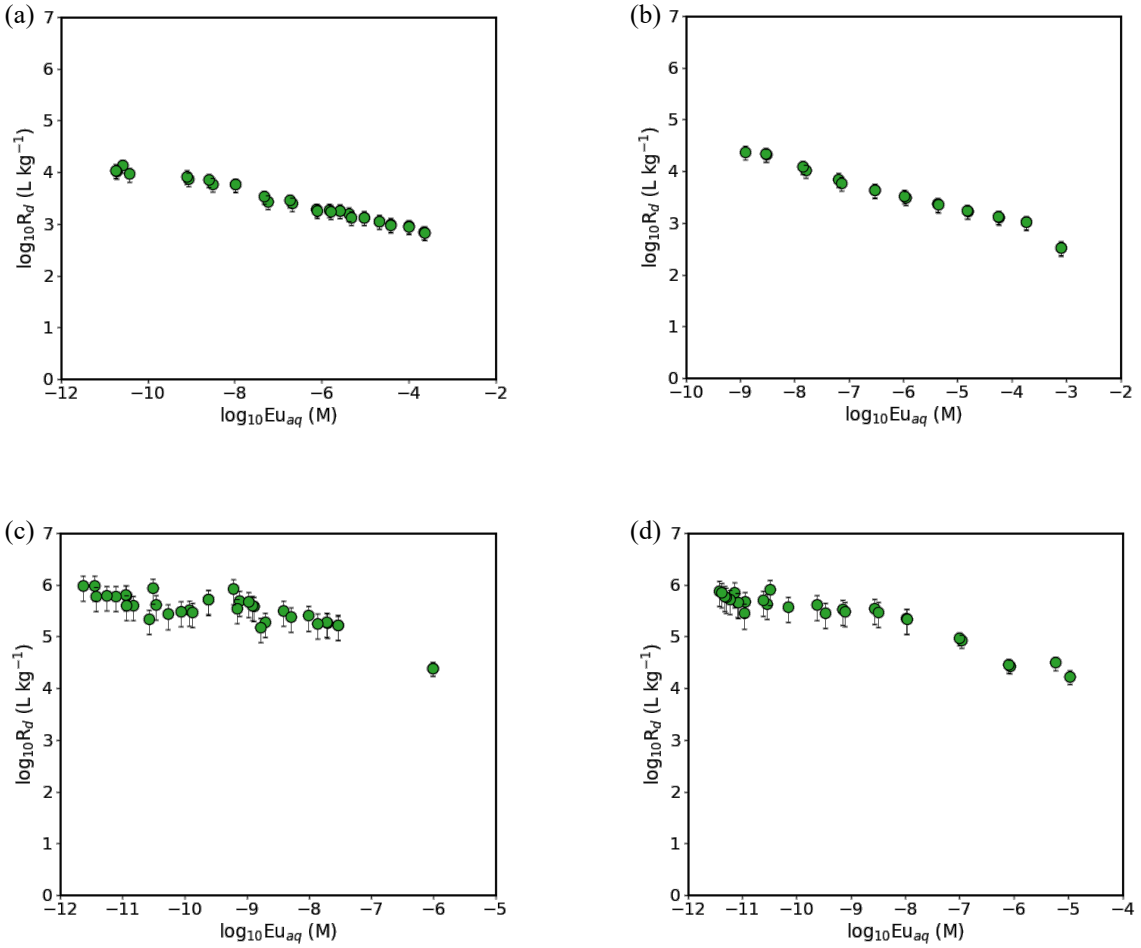

Fig. C-11: Eu(III) sorption isotherm on Na-montmorillonite in 0.1 M $NaClO_4$
(a) at pH 5.9, (b) at pH 6, (c) at pH 7.9, (d) at pH 8

C.7 Neptunium

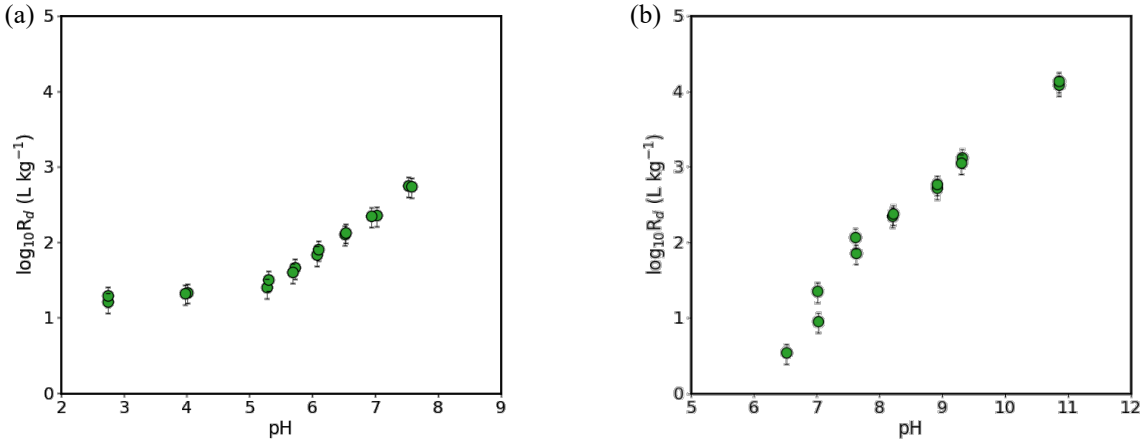

Fig. C-12: pH edges of Np(V) on Na-illite in 0.1 M $NaClO_4$

(a) $C_{in}(Np) = 5 \times 10^{-7}$ M, S:L = 4 g·L^{-1} and (b) $C_{in}(Np) = 2 \times 10^{-6}$ M, S:L = 1.8 g·L^{-1}

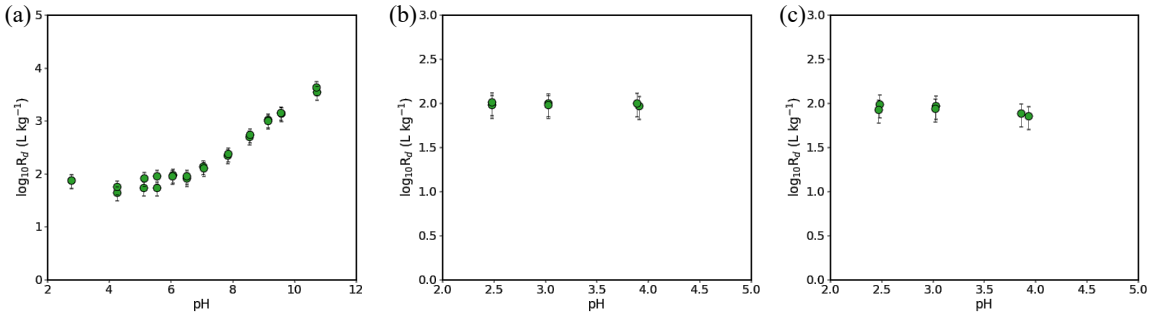

Fig. C-13: pH edges of Np(V) on Na-montmorillonite in 0.01 M $NaClO_4$

(a) $C_{in}(Np) = 2 \times 10^{-8}$ M, S:L = 2.2 g·L^{-1}, (b) $C_{in}(Np) = 1 \times 10^{-5}$ M (SWy-1), S:L = 0.9 g·L^{-1}, and (c) $C_{in}(Np) = 1 \times 10^{-5}$ M (STx-1), S:L = 0.9 g·L^{-1}

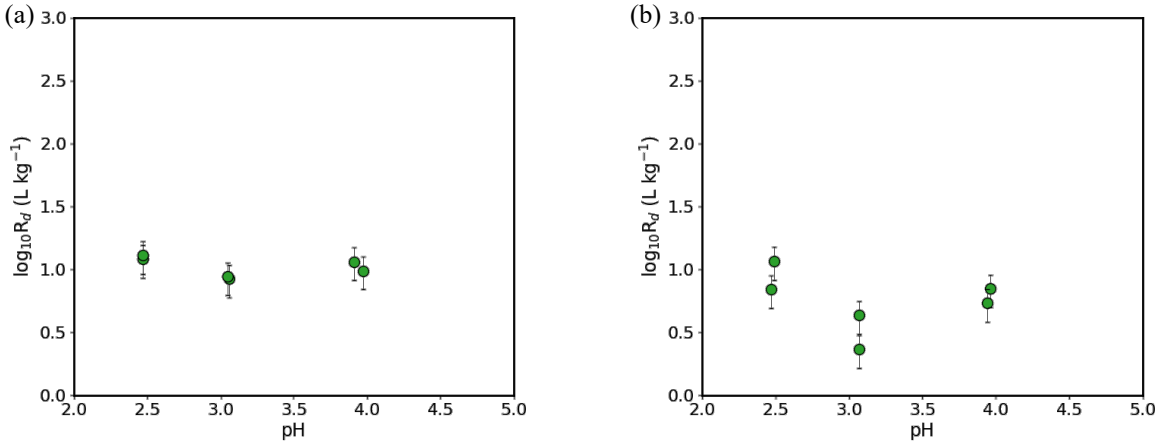

Fig. C-14: pH edges of Np(V) on Na-montmorillonite in 0.1 M $NaClO_4$

(a) $C_{in}(Np) = 1 \times 10^{-5}$ M (SWy-1) and (b) $C_{in}(Np) = 1 \times 10^{-5}$ M (STx-1), S:L = 2.3 g·L^{-1}

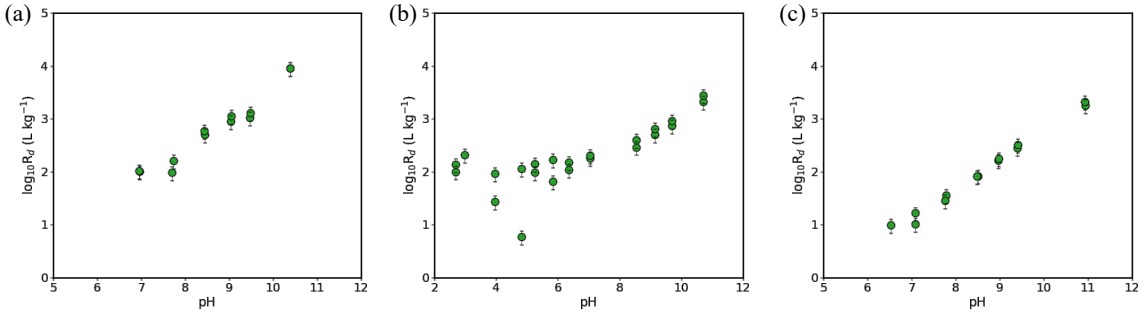

Fig. C-15: pH edges of Np(V) on Na-montmorillonite in 0.1 M $NaClO_4$

(a) $C_{in}(Np) = 2.4 \times 10^{-8}$ M (SWy-2), S:L = 0.5-1 g·L^{-1}, (b) $C_{in}(Np) = 4.16 \times 10^{-7}$ M (SWy-1), S:L = 0.7 g·L^{-1}, and (c) $C_{in}(Np) = 2 \times 10^{-6}$ M, S:L = 0.7-1.7 g·L^{-1}

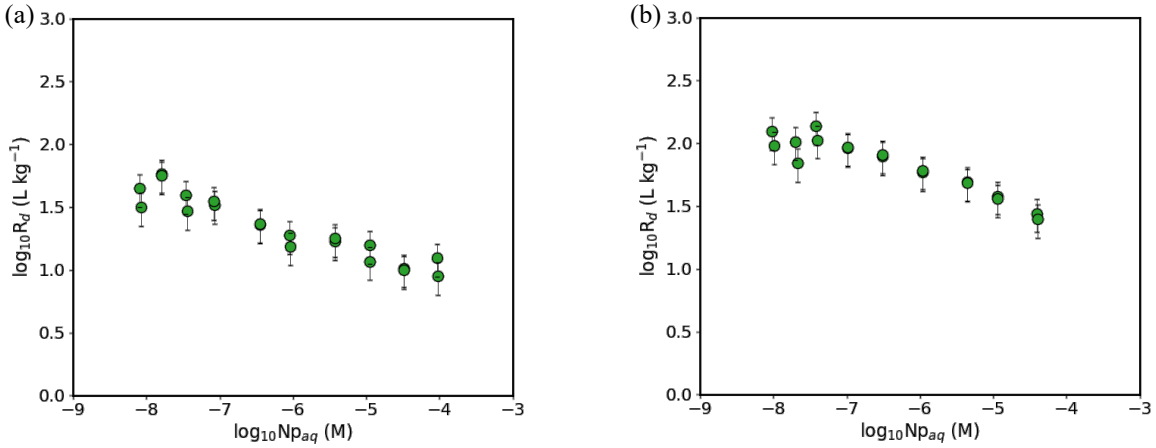

Fig. C-16: Sorption isotherms of Np(V) on Na-montmorillonite in 0.1 M $NaClO_4$
(a) pH 7 (SWy-1) and (b) pH 8 (SWy-2)

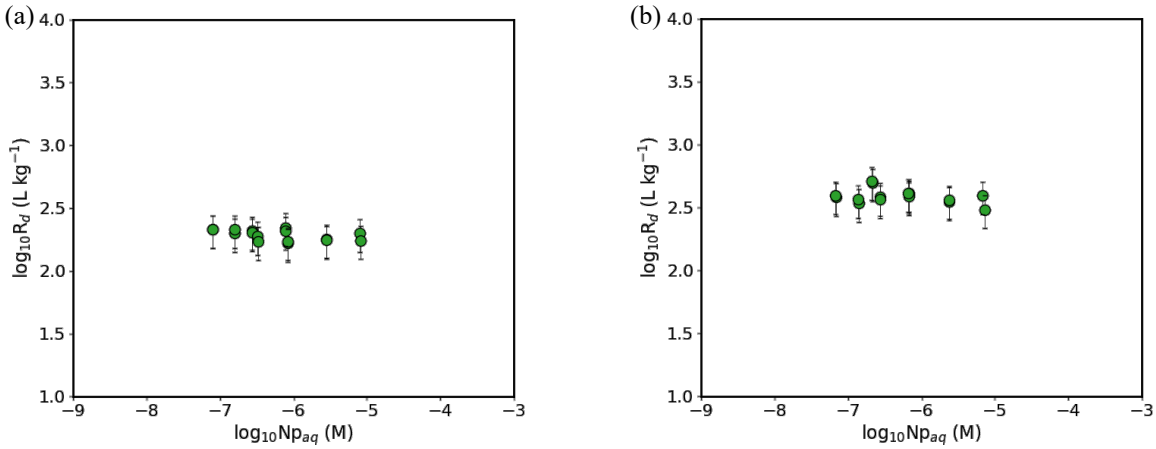

Fig. C-17: Sorption isotherms of Np(V) on Na-montmorillonite (STx-1) in 0.1 M $NaClO_4$
(a) pH 7.9 and (b) pH 8.8

C.8 Uranium

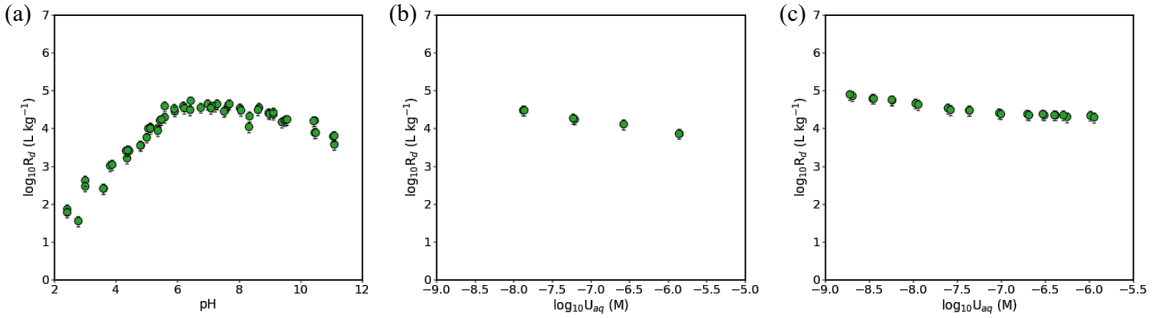

Fig. C-18: U(VI) sorption on Na-illite

(a) pH edge in 0.01 M $NaClO_4$, (b) sorption isotherm at pH 5.9 in 0.1 M $NaClO_4$, and (c) sorption isotherm at pH 7.4 in 0.1 M $NaClO_4$

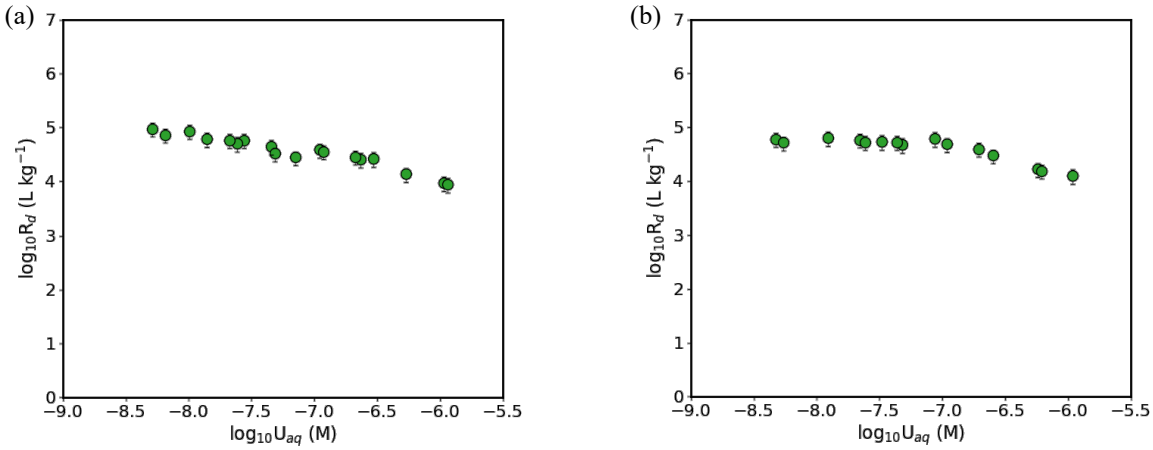

Fig. C-19: U(VI) sorption isotherms on Na-montmorillonite (SWy-2) in 0.1 M $NaClO_4$

(a) at pH 7 and (b) at pH 8

App. D LES/PSI batch sorption experiments on illite and montmorillonite

The table below describes the experimental conditions for the sorption measurements carried out at the Laboratory for Waste Management of the Paul Scherrer Institute for this study. The data were implemented in the sorption modelling together with published experimental data (see Tab. E-1).

Tab. D-1: Experimental conditions and data for new sorption measurements carried out at LES/PSI for this report

Metal	Clay	Clay source	Experiment	Background electrolyte	Solid to liquid ratio, $g \cdot L^{-1}$	Initial concentration of sorbed element	pH
Cs(I)	Montmorillonite	SWy-1	Edge	0.01 M $NaClO_4$	1.2	1×10^{-6}	2.8 – 11.1
		SWy-1	Edge	0.1 M $NaClO_4$	1.4	1×10^{-6}	2.6 – 10.9
Co(II)	Illite	IdP	Isotherm	0.1 M NaCl	2.2	$5.9 \times 10^{-7} – 1.5 \times 10^{-3}$	7.2
	Montmorillonite	Swy-2	Isotherm	0.1 M NaCl	2.1	$5.2 \times 10^{-7} – 1.5 \times 10^{-3}$	7.3
Mn(II)	Illite	IdP	Edge	0.1 M NaCl	2.1	4.7×10^{-8}	4 – 7.5
		IdP	Edge	0.1 M NaCl	2.1	4.7×10^{-8}	4 – 7.5
		IdP	Isotherm	0.1 M NaCl	2	$2.6 \times 10^{-8} – 7.7 \times 10^{-4}$	5.95
		IdP	Isotherm	0.1 M NaCl	2	$2.6 \times 10^{-8} – 7.7 \times 10^{-4}$	7.3
	Montmorillonite	SWy-2	Edge	0.1 M NaCl	1.7 – 1.8	4.5×10^{-8}	2 – 9.9
		SWy-2	Isotherm	0.1 M NaCl	1.7	$2.8 \times 10^{-8} – 7.7 \times 10^{-4}$	6
		SWy-2	Isotherm	0.1 M NaCl	1.7	$2.7 \times 10^{-8} – 7.7 \times 10^{-4}$	7.3
		SWy-2	Isotherm	0.1 M NaCl	1.7	$2.4 \times 10^{-8} – 7.7 \times 10^{-5}$	8.5
		SWy-2	Isotherm	0.1 M NaCl	1.7	$3 \times 10^{-8} – 6.4 \times 10^{-4}$	8.7
Ni(II)	Illite	IdP	Edge	0.1 M $NaClO_4$	1.5	2×10^{-9}	3.1 – 9.1
		IdP	Isotherm	0.1 M $NaClO_4$	1.5	$8.6 \times 10^{-9} – 7.1 \times 10^{-4}$	7
	Montmorillonite	SWy	Isotherm	0.1 M $NaClO_4$	2.1	$1.6 \times 10^{-8} – 1.7 \times 10^{-5}$	7.7
		SWy	Isotherm	0.1 M $NaClO_4$	0.24	$3 \times 10^{-8} – 4 \times 10^{-5}$	7.7
Pb(II)	Illite	IdP	Edge	0.1 M NaCl	0.3 / 0.6	5×10^{-8}	2.5 – 9.9
	Montmorillonite	SWy-2	Isotherm	0.1 M NaCl	1.6	$7.9 \times 10^{-9} – 7.9 \times 10^{-5}$	8
Zn(II)	Montmorillonite	IFSM	Edge	0.1 M $NaClO_4$	0.6 – 3.6	2.2×10^{-7}	4.4 – 8.7
		SWy-1	Isotherm	0.1 M $NaClO_4$	2.1	$1 \times 10^{-8} – 1.7 \times 10^{-5}$	7.7
Eu(III)	Illite	IdP	Edge	0.3 M $NaClO_4$	0.6 – 1.9	2.1×10^{-9}	3.9 – 9.3
		IdP	Edge	0.6 M $NaClO_4$	0.6 – 1.9	2.1×10^{-9}	3.8 – 9.3
		IdP	Edge	1 M $NaClO_4$	0.6 – 1.9	2.1×10^{-9}	3.8 – 9.3
	Montmorillonite	STx	Edge	0.3 M NaCl	0.3 – 1.2	6.5×10^{-9}	3.7 – 9.4
		STx	Edge	0.6 M NaCl	0.3 – 1.2	6.5×10^{-9}	3.8 – 9.3
		SWy-1	Isotherm	0.1 M $NaClO_4$	1.3	$2.8 \times 10^{-10} – 4.4 \times 10^{-4}$	5.9
		SWy-1	Isotherm	0.1 M $NaClO_4$	1.8	$1.5 \times 10^{-9} – 4.6 \times 10^{-4}$	6.8
		STx	Isotherm	0.1 M $NaClO_4$	1	$2.3 \times 10^{-9} – 2.5 \times 10^{-5}$	7.9
		STx-1	Isotherm	0.1 M $NaClO_4$	1	$3.1 \times 10^{-9} – 2 \times 10^{-4}$	8

Tab. D-1: Cont.

Metal	Clay	Clay source	Experiment	Background electrolyte	Solid to liquid ratio, $g \cdot L^{-1}$	Initial concentration of sorbed element	pH
Th(IV)	Montmorillonite	SWy-2	Edge	0.1 M $NaClO_4$	0.28	3.3×10^{-11}	3.8 – 11
Np(V)	Illite	IdP	Edge	0.1 M NaCl	2 / 4	3.8×10^{-8}	5.5 – 10.6
		IdP	Edge	0.1 M $NaClO_4$	4	5×10^{-7}	2.8 – 7.6
		IdP	Edge	0.1 M $NaClO_4$	1.8	2×10^{-6}	6.5 – 10.9
		IdP	Isotherm	0.1 M NaCl	2.3 / 2.5	7.1×10^{-9} – 7.9×10^{-5}	7.7
	Montmorillonite	SWy-1	Edge	0.01 M $NaClO_4$	2.2	2×10^{-8}	2.8 – 10.7
		SWy	Edge	0.1 M $NaClO_4$	0.7 – 1.7	2×10^{-6}	6.5 – 10.9
		SWy-2	Edge	0.1 M $NaClO_4$	0.5 – 1	2.4×10^{-8}	7 – 10.4
		SWy-1	Edge	0.1 M $NaClO_4$	0.7	4.16×10^{-7}	2.7 – 10.7
		SWy-1	Edge	0.1 M $NaClO_4$	2.3	1×10^{-5}	2.5 – 4
		STx-1	Edge	0.1 M $NaClO_4$	2.3	1×10^{-5}	2.5 – 4
		SWy-1	Edge	0.01 M $NaClO_4$	0.9	1×10^{-5}	2.5 – 3.9
		STx-1	Edge	0.01 M $NaClO_4$	0.9	1×10^{-5}	2.5 – 3.9
		STx-1	Isotherm	0.1 M $NaClO_4$	1.2	9.9×10^{-8} – 9.9×10^{-6}	7.9
		STx-1	Isotherm	0.1 M $NaClO_4$	1.2	9.9×10^{-8} – 9.9×10^{-6}	8.8
		SWy-1	Isotherm	0.1 M $NaClO_4$	5.3 – 5.4	1×10^{-8} – 1×10^{-4}	7
		SWy-2	Isotherm	0.1 M $NaClO_4$	2.7	1.3×10^{-8} – 4.3×10^{-5}	8
U(VI)	Illite	IdP	Edge	0.01 M $NaClO_4$	0.9 – 2.1	2.2×10^{-7}	2.4 – 11.1
		IdP	Edge	0.01 M $NaClO_4$	1.1 – 2.9	2.2×10^{-7}	2.8 – 11.1
		IdP	Isotherm	0.01 M $NaClO_4$	2.5	1.1×10^{-6} – 2.7×10^{-5}	5.9
		IdP	Isotherm	0.1 M $NaClO_4$	1.2 – 1.3	5.3×10^{-7} – 1.6×10^{-4}	7.2
		IdP	Isotherm	0.1 M $NaClO_4$	2 – 2.1	3.5×10^{-7} – 5.2×10^{-5}	7.2
		IdP	Isotherm	0.1 M $NaClO_4$	2.2 – 2.3	3.5×10^{-7} – 5.2×10^{-5}	7.4
	Montmorillonite	SWy-2	Isotherm	0.1 M $NaClO_4$	2	2.4×10^{-7} – 6.1×10^{-6}	7
		SWy-2	Isotherm	0.1 M $NaClO_4$	0.5	2.4×10^{-7} – 1.7×10^{-5}	8

App. E Peer-reviewed data of batch sorption experiments on illite and montmorillonite used for the sorption model development

Tab. E-1: Batch sorption experimental data (including references) on illite and montmorillonite documented in the literature used for the sorption model development in this report

Metal	Clay	Clay source	Experiment	Background electrolyte	pH*	Reference
Cs(I)	Illite	IdP	Edge	0.1 M $NaClO_4$	2.8 – 10.9	Poinssot et al. (1999)
		IdP	Edge	0.1 M $NaClO_4$	2.7 – 10.8	Poinssot et al. (1999)
		IdP	Edge	0.1 M $NaClO_4$	2.7 – 10.8	Poinssot et al. (1999)
		IdP	Edge	0.1 M $NaClO_4$	2.9 – 10.8	Poinssot et al. (1999)
		IdP	Edge	0.01 M $NaClO_4$	2.7 – 11	Poinssot et al. (1999)
		IdP	Edge	0.01 M $NaClO_4$	6.2 – 9.2	Poinssot et al. (1999)
		IdP	Edge	1 M $NaClO_4$	1.8 – 9.2	Poinssot et al. (1999)
		IdP	Edge	0.01 M KCl	2.9 – 11.3	Poinssot et al. (1999)
		Morris illite	Isotherm	0.02 M $NaNO_3$	7	Brouwer et al. (1983)
		IdP	Isotherm	0.1 M $NaClO_4$	7	Poinssot et al. (1999)
		Morris illite	Isotherm	0.02 M KNO_3	7	Brouwer et al. (1983)
		Morris illite	Isotherm	0.002 M KNO_3	7	Brouwer et al. (1983)
		IdP	Isotherm	0.01 M KCl	7	Staunton & Roubaud (1997)
		Fithian illite	Isotherm	0.001 M KCl	7	Comans et al. (1991)
	Montmorillonite	SWy-1	Isotherm	0.01 M $NaClO_4$	6	Bradbury & Baeyens (2002a)
Cd(II)	Montmorillonite	Kunimine CC, Japan	Edge	0.25 M $NaNO_3$	2.6 – 7.2	Itami & Yanai (2006)
		FEBEX bentonite	Edge	0.1 M $NaClO_4$	5 – 9.4	Missana et al. (2023)
		SWy-1	Edge	0.1 M $NaClO_4$	4.6 – 7.3	Zachara et al. (1993)
		FEBEX bentonite	Isotherm	0.1 M $NaClO_4$	7.8	Missana et al. (2023)
Co(II)	Illite	IdP	Edge	0.1 M $NaClO_4$	4.3 – 9.5	Montoya et al. (2018)
		IdP	Edge	0.1 M $NaClO_4$	4.3 – 9.4	Montoya et al. (2018)
		IdP	Edge	0.1 M $NaClO_4$	4.3 – 9.3	Montoya et al. (2018)
		IdP	Isotherm	0.1 M $NaClO_4$	5	Montoya et al. (2018)
		IdP	Isotherm	0.1 M $NaClO_4$	7.1	Marques Fernandes et al. (2015)
	Montmorillonite	Swy-2	Edge	0.1 M $NaClO_4$	4 – 10.9	Baeyens & Bradbury (2017)
		Swy-2	Isotherm	0.1 M $NaClO_4$	7.3	Baeyens & Bradbury (2017)

Tab. E-1: Cont.

Metal	Clay	Clay source	Experiment	Background electrolyte	pH*	Reference
Fe(II)	Montmorillonite	CBD treated iFSM	Edge	0.1 M $NaClO_4$	4.4 – 9.3	Soltermann et al. (2013)
		synth iFM	Edge	0.1 M $NaClO_4$	3.4 – 9.2	Soltermann et al. (2013)
		STx	Edge	0.1 M $NaClO_4$	2.3 – 9.1	Soltermann et al. (2014)
		synth iFM	Isotherm	0.1 M $NaClO_4$	6.2	Soltermann et al. (2013)
		synth iFM	Isotherm	0.3 M $NaClO_4$	6.7	Soltermann et al. (2013)
		STx	Isotherm	0.1 M $NaClO_4$	6.2	Soltermann et al. (2014)
		STx	Isotherm	0.1 M $NaClO_4$	6.2	Soltermann et al. (2014)
Ni(II)	Illite	IdP	Edge	0.01 M $NaClO_4$	6.3 – 9.2	Poinssot et al. (1999)
		IdP	Edge	0.01 M $NaClO_4$	6 – 8.8	Poinssot et al. (1999)
		IdP	Edge	0.1 M $NaClO_4$	3.2 – 9.1	Poinssot et al. (1999)
		IdP	Edge	0.1 M $NaClO_4$	4.3 – 8.8	Poinssot et al. (1999)
		IdP	Edge	0.1 M $NaClO_4$	4.1 – 9.4	Bradbury & Baeyens (2005a)
		IdP	Edge	0.5 M $NaClO_4$	3.3 – 9.1	Bradbury & Baeyens (2005a)
		IdP	Edge	0.01 M $NaClO_4$	6 – 9.3	Bradbury & Baeyens (2005a)
		IdP	Isotherm	0.1 M $NaClO_4$	7.2	Marques Fernandes & Baeyens (2020)
		IdP	Isotherm	0.1 M $NaClO_4$	7	Marques Fernandes & Baeyens (2020)
		IdP	Isotherm	0.1 M $NaClO_4$	7.8	Bradbury & Baeyens (2005a)
		IdP	Isotherm	0.1 M $NaClO_4$	7.8	Bradbury & Baeyens (2005a)
		IdP	Isotherm	0.1 M $NaClO_4$	6	Bradbury & Baeyens (2005a)
		IdP	Isotherm	0.1 M $NaClO_4$	7	Poinssot et al. (1999)
	Montmorillonite	SWy-1	Edge	0.01 M $NaClO_4$	4.7 – 9.9	Baeyens & Bradbury (1997)
		SWy-1	Edge	0.03 M $NaClO_4$	4.7 – 9.8	Baeyens & Bradbury (1997)
		SWy-1	Edge	0.1 M $NaClO_4$	4.3 – 9.9	Baeyens & Bradbury (1997)
		SWy-1	Isotherm	0.1 M $NaClO_4$	5.9	Baeyens & Bradbury (1997)
		SWy-1	Isotherm	0.1 M $NaClO_4$	7	Baeyens & Bradbury (1997)
		SWy-1	Isotherm	0.1 M $NaClO_4$	7.1	Marques Fernandes & Baeyens (2020)
		Swy-1	Isotherm	0.1 M $NaClO_4$	8.2	Baeyens & Bradbury (1997)
Pb(II)	Illite	IdP	Edge	0.1 M NaCl	1.5 – 9.5	Marques Fernandes & Baeyens (2019)
		IdP	Isotherm	0.02 M NaCl	5.95	Marques Fernandes & Baeyens (2019)
		IdP	Isotherm	0.1 M NaCl	6.9	Marques Fernandes & Baeyens (2019)
		IdP	Isotherm	0.1 M NaCl	7.2	Marques Fernandes & Baeyens (2019)
	Montmorillonite	SWy-2	Edge	0.1 M NaCl	4 – 9.1	Marques Fernandes & Baeyens (2019)
		SWy-2	Edge	0.1 M NaCl	4 – 9.6	Marques Fernandes & Baeyens (2019)
		SWy-2	Isotherm	0.1 M NaCl	5.9	Marques Fernandes & Baeyens (2019)
		SWy-2	Isotherm	0.1 M NaCl	7	Marques Fernandes & Baeyens (2019)

Tab. E-1: Cont.

Metal	Clay	Clay source	Experiment	Background electrolyte	pH*	Reference
Ra(II)	Illite	IdP	Edge	0.3 M NaCl	5.6 – 9.4	Marques Fernandes et al. (2023)
	Montmorillonite	SWy-2	Edge	0.3 M NaCl	5.6 – 9.2	Klinkenberg et al. (2021)
Zn(II)	Illite	IdP-2	Edge	0.01 M $NaClO_4$	4.3 – 9.7	Montoya et al. (2018)
		IdP-2	Edge	0.1 M $NaClO_4$	4.3 – 9.5	Montoya et al. (2018)
		IdP	Isotherm	0.0011 M $NaClO_4$	5.91	Montoya et al. (2018)
		IdP	Isotherm	0.1 M $NaClO_4$	5	Montoya et al. (2018)
		IdP	Isotherm	0.1 M $NaClO_4$	5	Montoya et al. (2018)
		IdP	Isotherm	0.1 M $NaClO_4$	7.2	Montoya et al. (2018)
		IdP	Isotherm	0.1 M $NaClO_4$	7.2	Montoya et al. (2018)
		IdP	Isotherm	0.1 M $NaClO_4$	8.4	Montoya et al. (2018)
	Montmorillonite	SWy-1	Edge	0.1 M $NaClO_4$	4.2 – 9.8	Baeyens & Bradbury (1997)
		SWy-1	Isotherm	0.1 M $NaClO_4$	5.6	Baeyens & Bradbury (1997)
		SWy-1	Isotherm	0.1 M $NaClO_4$	7	Baeyens & Bradbury (1997)
		STx-1	Isotherm	0.1 M $NaClO_4$	7.2	Dähn et al. (2011)
		Milos	Isotherm	0.1 M $NaClO_4$	7.2	Dähn et al. (2011)
		SWy-1	Isotherm	0.1 M $NaClO_4$	7.3	Marques Fernandes & Baeyens (2020)
Am(III)	Illite	IdP	Edge	0.1 M $NaClO_4$	2.6 – 10.7	Bradbury & Baeyens (2009b)
		IdP	Edge	0.1 M $NaClO_4$	2.7 – 10	Gorgeon (1994)
	Montmorillonite	SWy-1	Edge	0.1 M $NaClO_4$	2.6 – 10.7	Bradbury & Baeyens (2006)
		SWy	Edge	0.1 M $NaClO_4$	2.6 – 11	Gorgeon (1994)
Eu(III)	Illite	IdP	Edge	0.1 M $NaClO_4$	2.7 – 10.8	Poinssot et al. (1999)
		IdP	Edge	0.1 M $NaClO_4$	2.5 – 10.8	Bradbury & Baeyens (2009a)
		IdP	Edge	0.5 M $NaClO_4$	3 – 10.8	Bradbury & Baeyens (2005a)
		IdP	Edge	0.5 M $NaClO_4$	3.1 – 10.7	Bradbury & Baeyens (2005a)
		IdP	Edge	0.5 M $NaClO_4$	3.1 – 10.8	Bradbury & Baeyens (2005a)
		IdP	Edge	0.5 M $NaClO_4$	3.3 – 10.7	Bradbury & Baeyens (2005a)
		IdP	Isotherm	0.1 M $NaClO_4$	7	Poinssot et al. (1999)
		IdP	Isotherm	0.1 M $NaClO_4$	7	Bradbury & Baeyens (2005a)
		IdP	Isotherm	0.1 M $NaClO_4$	7.2	Marques Fernandes & Baeyens (2020)
		IdP	Isotherm	0.1 M $NaClO_4$	7.2	Marques Fernandes & Baeyens (2020)
		IdP	Isotherm	0.1 M $NaClO_4$	7.1	Marques Fernandes & Baeyens (2020)
	Montmorillonite	SWy-1	Edge	0.1 M $NaClO_4$	4.2 – 9	Bradbury & Baeyens (2002b)
		SWy-1	Edge	0.1 M $NaClO_4$	2.7 – 10.6	Bradbury & Baeyens (2006)
		SWy-1	Isotherm	0.1 M $NaClO_4$	6	Bradbury & Baeyens (2002b)
		SWy-2	Isotherm	0.1 M $NaClO_4$	7.2	Marques Fernandes & Baeyens (2020)
		SWy-1	Isotherm	0.1 M $NaClO_4$	7.4	Marques Fernandes & Baeyens (2020)

Tab. E-1: Cont.

Metal	Clay	Clay source	Experiment	Background electrolyte	pH*	Reference
Sn(IV)	Illite	IdP	Edge	0.1 M $NaClO_4$	4.1 – 12.4	Bradbury & Baeyens (2009a)
	Montmorillonite	SWy-1	Edge	0.1 M $NaClO_4$	4.1 – 9.5	Bradbury & Baeyens (2005b)
		Kunipia F	Edge	0.5 M NaCl	6.7 – 9.9	Ishidera et al. (2023)
		Kunipia F	Edge	0.5 M NaCl	7.5 – 9.9	Ishidera et al. (2023)
Th(IV)	Illite	IdP	Edge	0.1 M $NaClO_4$	4.1 – 10.9	Bradbury & Baeyens (2009b)
		SWy-1	Edge	0.1 M $NaClO_4$	4 – 10.9	Bradbury & Baeyens (2005b)
Nb(V)	Illite	IMt-1	Edge	0.1 M $NaClO_4$	4.7 – 10.6	Ervanne et al. (2014)
	Montmorillonite	**	Edge	0.1 M $NaClO_4$	4.7 – 9.1	Ervanne et al. (2014)
		Kunipia F	Edge	0.5 M NaCl	7.2 – 9.2	Ishidera et al. (2023)
		Kunipia F	Edge	0.5 M NaCl	7.2 – 9.8	Ishidera et al. (2023)
Np(V)	Illite	IdP	Edge	0.1 M $NaClO_4$	2.5 – 10.7	Gorgeon (1994)
		IdP	Edge	0.025 M $NaClO_4$	2.6 – 10.9	Gorgeon (1994)
	Montmorillonite	SWy	Edge	1 M $NaClO_4$	2.7 – 10.6	Gorgeon (1994)
		SWy	Edge	0.1 M $NaClO_4$	2.6 – 11.2	Gorgeon (1994)
		SWy	Edge	0.025 M $NaClO_4$	2.6 – 11.1	Gorgeon (1994)
Pa(V)	Illite	IdP-2	Edge	0.1 M $NaClO_4$	4.1 – 10.7	Bradbury & Baeyens (2009b)
		IdP-2	Edge	0.1 M $NaClO_4$	4.1 – 10.6	Bradbury & Baeyens (2009b)
		IdP-2	Edge	0.1 M $NaClO_4$	4 – 9.1	Bradbury & Baeyens (2009b)
		IdP-2	Edge	0.1 M $NaClO_4$	4 – 10.8	Bradbury & Baeyens (2009b)
	Montmorillonite	SWy-1	Edge	0.1 M $NaClO_4$	4 – 10.7	Bradbury & Baeyens (2006)
		SWy-1	Edge	0.1 M $NaClO_4$	4 – 10.7	Baeyens & Marques Fernandes (2018)
U(VI)	Illite	IdP	Edge	0.01 M $NaClO_4$	2.8 – 10.7	Bradbury & Baeyens (2005a)
		IdP	Edge	0.1 M $NaClO_4$	2.7 – 10.1	Bradbury & Baeyens (2009b)
		IdP	Edge	0.1 M $NaClO_4$	2.6 – 10.7	Bradbury & Baeyens (2009b)
		IdP	Isotherm	0.1 M $NaClO_4$	4.8	Bradbury & Baeyens (2005a)
	Montmorillonite	SWy-1	Edge	0.01 M $NaClO_4$	2.6 – 10.7	Bradbury & Baeyens (2005b)
		SWy-1	Edge	0.1 M $NaClO_4$	2.6 – 10.7	Bradbury & Baeyens (2005b)
		SWy-1	Edge	0.1 M $NaClO_4$	2.8 – 10.8	Marques Fernandes et al. (2012)
		SWy-1	Isotherm	0.1 M $NaClO_4$	5	Bradbury & Baeyens (2005b)
		SWy-1	Isotherm	0.1 M $NaClO_4$	6.8	Bradbury & Baeyens (2005b)
		SWy-2	Isotherm	0.1 M $NaClO_4$	8.1	Marques Fernandes et al. (2012)

* Only the ranges used for fitting in this work are indicated. In the original papers, the ranges can be wider.
** Here, the R_d values of Nb(V) on montmorillonite are assumed to be similar to those on illite in Ervanne et al. (2014) (see Section 4.2.14).